Segmentation of Lung Structures in CT

Lo, Pechin Chien Pau

Publication date:
2010

Document version
Early version, also known as pre-print

Citation for published version (APA):
Lo, P. C. P. (2010). *Segmentation of Lung Structures in CT*. Faculty of Science, University of Copenhagen.

FACULTY OF SCIENCE
UNIVERSITY OF COPENHAGEN

PhD thesis

Pechin Chien Pau Lo

Segmentation of Lung Structures in CT

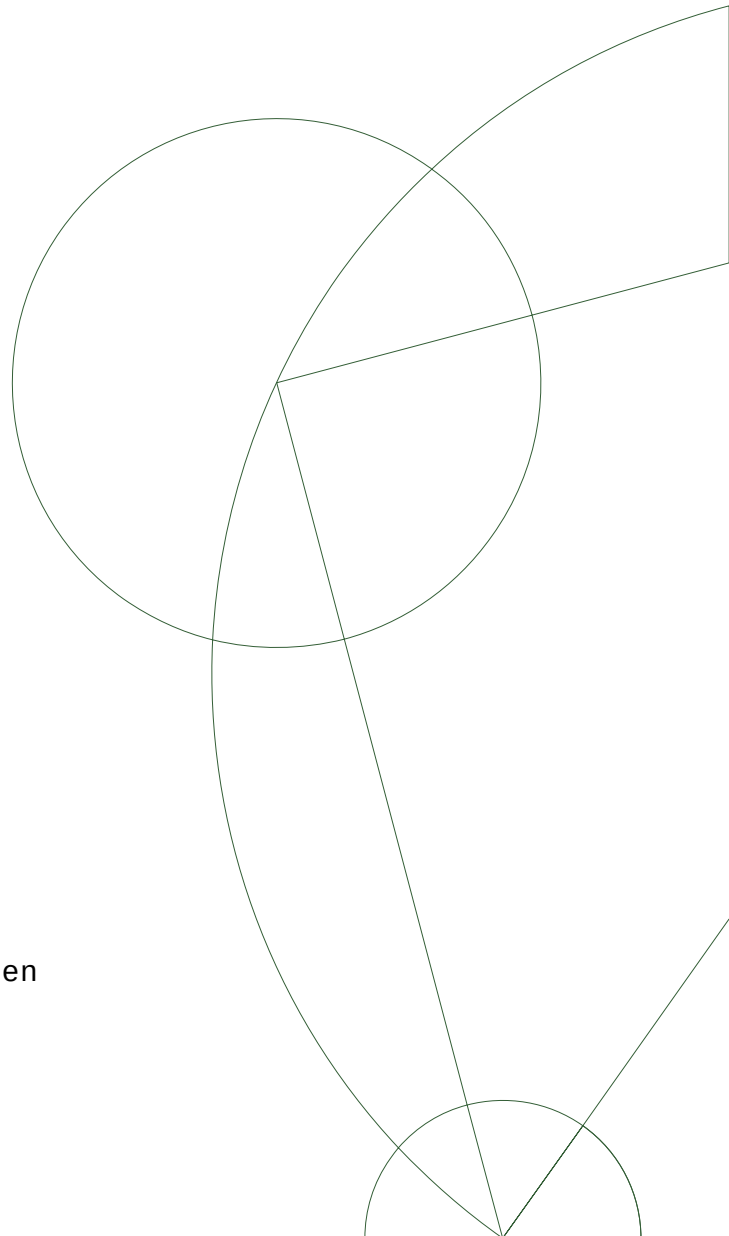

Main academic advisor: Marleen de Bruijne
Co-academic advisors: Jon Sporring, Mads Nielsen
Submitted: 25/03/10

Contents

Abstract

This thesis proposes and evaluates new algorithms for segmenting various lung structures in computed tomography (CT) images, namely the lungs, airway trees and vessel trees. The main objective of these algorithms is to facilitate a better platform for studying Chronic Obstructive Pulmonary Disease (COPD) using CT scans from the Danish Lung Cancer Screening Trial (DLCST) study.

We propose a fully automated lung segmentation algorithm that is based on region growing and the assumption that the lungs are of lower intensities than surrounding structures in CT. Furthermore, we also propose a post processing step that detects and removes esophagus regions, wrongly added by the region growing process, to improve the reliability of the lung segmentation algorithm. The proposed algorithm has been successfully applied to more than 6000 low dose CT scans from the DLCST study. Among the CT scans applied, 200 randomly selected CT scans were manually evaluated by medical experts, and only negligible or minor errors were found in nine scans. The proposed algorithm has been used to study how changes in smoking behavior affect CT based emphysema quantification. The algorithms for segmenting the airway trees and vessel trees proposed in this thesis are also built on top of this lung segmentation algorithm.

We propose a voxel classification based airway appearance model for the segmentation of airway trees, which is trained using easy to obtain manual airway tree segmentations that can be incomplete. Two approaches for extracting the airway tree using the voxel classification appearance model are proposed: a vessel guided approach and a locally optimal paths approach.

The vessel guided approach exploits the fact that all airways are accompanied by arteries of similar orientation. This is accomplished using a vessel orientation similarity measure, which is combined with the proposed appearance model in a region growing framework. Experiments on CT scans from the DLCST study have shown that the proposed approach performs better than simply applying region growing on the response of the appearance model or on the intensity alone. The proposed approach has also been applied to the diverse set of CT scans from the Extraction of Airways from CT (EXACT'09) dataset, where the proposed approach has the advantage of having fairly high sensitivity with very few false positives, when compared to other state of the art airway tree extraction algorithms.

The locally optimal paths approach extracts airway trees by continually extending locally defined optimal paths, generated using a cost function that incorporates the airway appearance model, and shape and orientation measures that are derived using a multiscale Hessian eigen analysis. The decisions in this approach are made on a path basis, which makes it easy to ignore small number of unlikely airway points on a path. Therefore, the proposed approach is capable of overcoming local occlusions, which would otherwise stopped region growing based algorithms that make decisions on a voxel basis. Experiment results have shown that more complete airway trees are extracted with the locally optimal paths approach as compared to the vessel guided approach, though at a price of a slight increase in false positive rate. This approach is also used in combination with a multiscale vessel enhancement filter for the extraction of vessel trees in CT. It was shown that the locally optimal path approach is capable of extracting a better connected vessel tree and extract more of the small peripheral vessels in comparison to applying a threshold on the output of the vessel enhancement filter.

Finally, we also constructed a reference standard for evaluating airway tree extraction algorithms in the EXACT'09 study, which is the first study to perform standardized quantitative evaluation of different airway tree extraction algorithms based on a standard dataset. Segmented airway trees from the algorithms that participate in the study were used to construct the reference standard needed, circumventing the need for labour intensive manual segmentations. Each segmented trees is subdivided into its individual branch segments, where the branch segments are subjected to visual inspection

by human observers. Branch segments that are determined to be correctly segmented during the inspection process are then combined to form the reference standard.

Chapter 1

Introduction

Image segmentation is the process of partitioning regions in an image into meaningful segments belonging to different objects. When analyzing an image, it is usually much more convenient to isolate objects of interest before doing the actual analysis, either in the form of cutouts or highlights using distinguishable borders. Such is the application of image segmentation to the analysis of images, where it usually precedes other analysis related processes. Since most application requires the segmentation of specific objects of interest, it is quite common for image segmentation techniques to include certain form of object recognition as well. Such is the case of medical image analysis, where medical experts are usually only interested in certain organs visible in the image, which is also the main reason why image segmentation is required in almost all medical image related applications.

Accurate quantification of disease regions or size of certain structures have always been difficult for humans. On the other hand, provided that the image is digitized and an accurate segmentation of the object of interest is available, obtaining quantification measures is usually quite straight forward and can be done very accurately using a computer. A typical example of quantification of diseased regions is the quantification of emphysema in lungs, which basically is the measurement of volumes of the regions within a segmented lung that are below a certain density threshold [33, 91]. Another example would be in measuring the dimension of airways, which can be easily computed provided that accurate segmentation of the airway lumen, airway walls, and the whole airway tree is available [9, 75].

Besides quantification, image segmentation is also used in other medical imaging related fields. In computer assisted surgery, image segmentation is needed for extraction of objects from medical images to allow for visualization and manipulation purpose, e.g. virtual colonoscopy. Image segmentation is also used for extraction of landmarks needed for computer aided navigation related tasks, such as computer guided bronchoscopy [30]. Another application of image segmentation is in easing or improving the performance of other processes, such as image registration [34, 55].

This thesis presents automated methods for segmenting several anatomy structures in chest computed tomography (CT) scans: namely the lungs, airway trees and pulmonary vessel trees. The medical context of the segmentation algorithms presented is, though not limited to, the facilitation of a better platform for the study of Chronic Obstructive Pulmonary Disease (COPD). The aim of this introduction chapter is to familiar readers with the background that motivates this thesis. An outline of the chapters in this thesis followed by a list of contributions are also presented in the end of this chapter.

1.1 COPD

COPD is a major cause of chronic morbidity and mortality worldwide [74, 87]. It is the fifth leading cause of death in 2002, projected to be the fourth leading cause of death and rank seventh as a worldwide burden of disease in 2030 [66]. It has been shown that COPD severely reduces quality of life [42, 124] and is a considerable economic burden that will continue to grow as the number of elderly people continues to increase [14].

The term COPD does not refer to a single disease, but is an umbrella term for chronic lung diseases

(a) Relatively healthy (b) Severe emphysema

Figure 1.1: An example of the appearance of lungs in CT of (a) a relatively healthy subject and (b) a subject suffering from severe emphysema.

that irreversibly limits airflow in the lungs. Although it is known that smoking is the major risk factor for COPD, treatment and understanding the progress of COPD remain a challenge due to the fact that COPD consists of a mixture of diseases. Components of COPD can be generalized into two parts: obstruction of airways due to diseases such as chronic bronchitis and obstructive bronchiolitis; and the destruction of lung parenchyma, mainly due to emphysema.

Current standard of defining COPD is via lung function tests (LFT): namely the forced expiratory volume in one second (FEV_1), defined as the volume exhaled during the first second of force expiration from a full inspiration level, and the forced vital capacity (FVC), defined as the total volume exhaled from a full inspiration level. A subject is said to suffer from obstructive pulmonary disease if FEV_1/FVC is less than 70%, and COPD if the obstruction is irreversible and chronic [87]. Severity of the desease is categorized into GOLD stages from one (mild) to four (severe), based on the ratio between the measured FEV_1 and a predicted FEV_1, which is calculated from a formula that takes into account the sex, age and height of the subject. A problem with LFT is that it is very insensitive to small changes in the lungs. For example, it has been reported that changes were only observed after the lungs have been severely damaged [33]. Another problem with LFT is that it is highly dependent on the cooperation and effort of the subject, therefore the measurements are usually noisy and have a low reproducibility rate.

CT imaging is capable of visualizing the effects of COPD. An advantage of CT over LFT is that CT can differentiate between the different types of COPD, making it possible to classify the different subgroups of diseases, be it due to obstruction in airways or destruction of parenchymal tissues. Figure 1.1 shows the difference in CT between lungs of a relatively healthy subject and those from a subject with severe emphysema. CT is also a lot more sensitive than LFT, as changes can now be identified locally within the lungs, instead of treating the lungs as a single entity as in LFT. Studies have shown that various density and morphology measurements derived from CT have high correlation with LFT measurements, showing promise of using CT as a better and more sensitive standard for defining COPD, as compared to LFT [33, 91]. Besides that, due to the morphology details that CT is capable of providing, it also offers the possibilities to better study the nature and progression of COPD.

CT however is not without its problems. Modern multi-detector CT scanner is capable of producing continuous volumetric scans of the whole lung in less than a minute, and up to sub millimeter resolution. Figure 1.2 shows an example of the different views of a CT image obtained from a multi-detector CT scanner. Although this means that CT scanners are capable of providing more detailed information, it also means that more data is being produced. Typical chest CT scan from a multi-detector results in around 400 slices of images for a single subject, making manual analysis of CT scans a laborious and tedious task. For large studies that involve thousands of subjects being scanned on a yearly basis, it becomes impractical to perform manual analysis on such CT scans. There is therefore an immediate need for fully automated solutions in the analysis of scans from CT scanner.

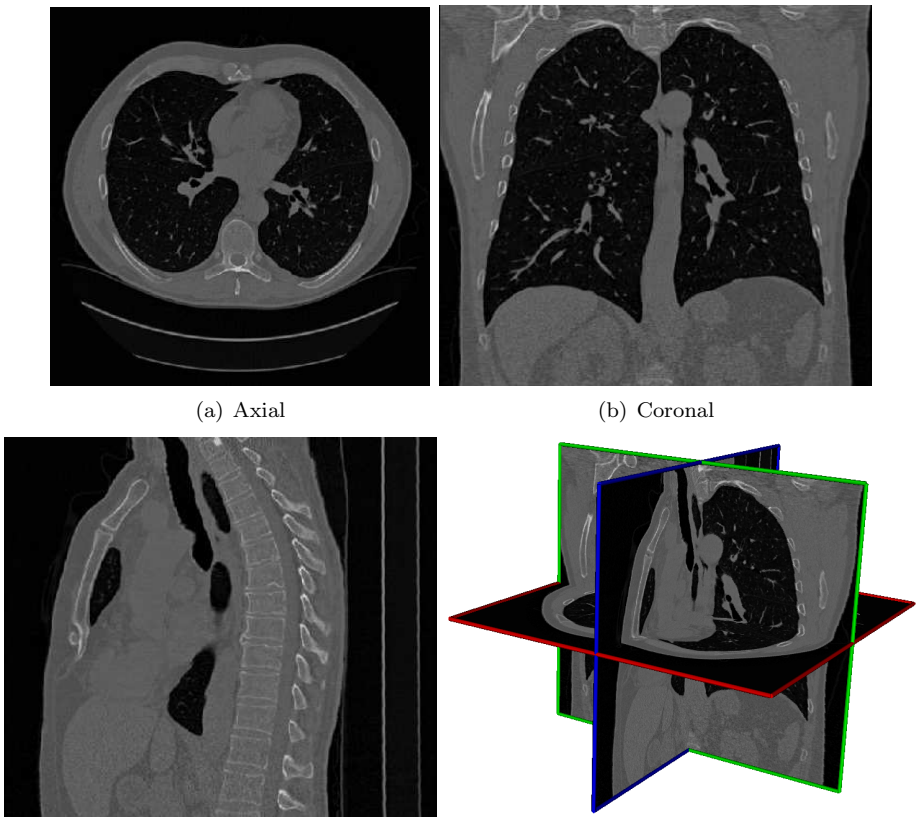

(a) Axial (b) Coronal

(c) Sagittal (d) 3D

Figure 1.2: The three views of a CT image: (a) axial, (b) coronal and (c) sagittal view. (d) A rendering showing the corresponding plan of each view in 3D.

Besides being able to process large amount data in an automated manner, there are also some structures that are just too complex to be segmented manually. A good example is the airway tree, which have been shown to play an important role in the analysis of COPD in recent studies [9, 18, 75], especially those from the small peripheral airways [53]. The first difficulty in manually segmenting the airway tree is the sheer number of individual airway branches involved, which can easily be more than 400 visible branches per airway tree. The second difficulty that complicates the problem even further is that it is very difficult to differentiate airways, especially the smaller ones, from surrounding structures by looking only at a single 2D slice. Experts usually need to take into account their appearance in 3D, relationship with surrounding structures and also connectivity with other more obvious airway branches, making the task extremely labour intensive. Figure 1.3 shows some examples of the appearance of airways in CT.

1.2 COPD quantification in the Danish Lung Cancer Screening Trial

The Danish Lung Cancer Screening Trial (DLCST) [80] is a 5 year trial investigating the effects of screening with low dose CT on the mortality of lung cancer that is conducted in Denmark. The study consists of a total of 4014 participants, where LFT and questionnaires were collected. By randomization, half of the participants (2052) were offered annual CT screening, where CT scans were taken yearly during the period of the study. The participants consist of former and current smokers, of age between 50 to 70 years, with a smoking history of more than 20 pack years, where one pack year is defined as 20 cigarettes (one pack) smoked per day for one year. Former smokers were only

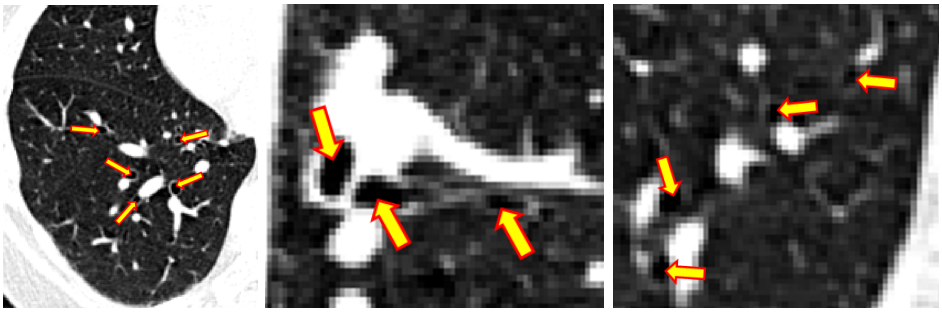

(a) (b) (c)

Figure 1.3: Examples of appearance of airways in CT. The arrows only points to the obvious airways in (a). For (b) and (c), other "airway like" structures in the image that are not pointed by the arrows are most probably not airways.

included if they had quit smoking after the age of 50 and less than 10 years before the inclusion date. The participants were also required to be relatively healthy, with a forced expiratory volume in one second (FEV_1) of at least 30% of predicted normal at baseline. Detailed description of the inclusion and exclusion criteria of the DLCST study is available in [80].

Although originally designed for cancer screening, the inclusion criteria that focused on smokers makes the DLCST study a unique opportunity to study COPD as well. For this reason, a "COPD quantification by CT, biomarkers and quality of life" (CBQ) study is also conducted in parallel with the DLCST study. The CBQ study involves only participants from DLCST that were subjected to CT screening, where an additional Saint George's respiratory questionnaire (SGRQ) [41] and blood samples were collected. The aim of this study is to investigate the roles of SGRQ, FEV_1, quantification measures from CT, genetic information, and inflammation markers from the blood in relation to diagnosis and development of COPD. A main objective of this thesis is to develop segmentation algorithms for CT scans in relation to the CBQ study.

1.3 Outline

The main contents of this thesis are presented in 7 chapters: Chapter 2 and 3 describes work related to lung segmentation, Chapter 4 to 7 are related to airway tree segmentation, Chapter 8 presents an adaptation of the algorithm in Chapter 7 for segmentation of the vessel tree. The following gives a brief description of each chapter, please refer to Chapter 9 for the full summary of the chapters.

Chapter 2 presents a region growing based method for segmenting lung fields in CT, which assumes that lung parenchyma is of lower intensity than surrounding tissues. Although such simple assumption may not be sufficient for segmenting subjects with dense pathologies in the lungs, this is in general not a problem for the targeted CT scans from the DLCST study, which mainly consisted of relatively healthy subjects. The proposed method was manually evaluated on 200 screening CT scans, and applied successfully to more than 6000 screening scans in the DLCST study and various types of CT scans from other studies. This lung segmentation algorithm also forms the basis for the algorithms and analyses presented in the following chapters.

Chapter 3 presents a study of the effects of smoking cessation on the quantification of emphysema in CT. The lung segmentation algorithm presented in the previous chapter was used to obtain the segmentation needed, and a 15th percentile density (PD15), which was adjusted based on the segmented lung volume, was used to quantify the emphysema. The study involves CT scans from 726 subjects, which consist of current and former smokers, taken at baseline and a year after. A clear difference in PD15 was observed between baseline scans of smokers and former smokers. Furthermore, between the baseline and the follow up scans, it was observed that PD15 was strongly influenced by changes in smoking behavior. The study concluded that current smoking status should be taken into account when using CT lung density to assess the severity of diseases such as emphysema.

Chapter 4 presents an algorithm based on region growing for the segmentation of airway trees in CT. The decision function of the region growing algorithm make use of a voxel classification based appearance model and the fact that artery vessels nearby airways are similar in orientation using a vessel orientation similarity measure. An interesting aspect of the presented appearance model is that it was only trained on a set of easily acquired, incomplete airway tree segmentations. The presented algorithm was evaluated on 250 low dose screening CT images from the DLCST study, where we observed that performing region growing on a decision function that combines both appearance model and the vessel orientation similarity measure works best, as compared to using only the appearance model or the intensity alone.

Chapter 5 applies the vessel guided approach in the previous chapter to a diverse set of CT scans from EXACT'09, which is an airway tree extraction challenge that is described in detail in the following chapter. Except for a few minor modifications to take into account the large variation in the quality of the CT scans, the core of the method along with the parameters used remain unchanged, which showed the robustness of the method. Compared to results from other participating teams, results from the evaluation shows that our method is capable of detecting relatively large portion of the tree correctly with very few false positives.

Chapter 6 presents the first study that compares large number of airway extraction algorithms on the same dataset using a reference, which was held in conjunction with MICCAI 2009. The study was named "Extraction of Airways from CT" (EXACT'09). The study involved 15 algorithms from different research groups, consisting of fully and semi automated algorithms. The dataset for the study consists of a total of 40 scans from subjects ranging from healthy volunteers to patients with severe lung disease, scanned at different sites with different CT scanner models, scanning protocols and reconstruction parameters. A unique approach of the study is that the reference is constructed using segmentation results from the participating teams. Airway trees are subdivided into their individual branches, which are subsequently evaluated manually via visual inspection by human observers. The reference is constructed by taking the union of all correct branches from the evaluation process. Interesting findings from the study include the fact that there is a large difference in the branches detected by different algorithms, and that better results can be achieved by combining segmentations from different algorithms.

Chapter 7 presents a method for extracting airway trees from CT images by continually extending the tree with locally optimal paths, generated based on the airway appearance model as well as shape measures and orientations derived using multi-scale Hessian eigen analysis. The main novelty of the presented method is that acceptance and termination criteria are made on a path basis, instead of the voxel basis that is used by most existing methods and Chapter 4. The result is a more robust method for tree extraction that is capable of overcoming local occlusions. Results from the experiments conducted showed that the proposed method is able to extract significantly more complete airway trees than the region growing approach presented in Chapter 4, though at the price of a slight increase in false positive rate.

Chapter 8 applies the concept of locally optimal paths to the extraction of pulmonary vessels in CT. The cost function is modified to make use of the response from a multiscale vessel enhancement filter. Additional improvements such as the use of search spheres of multiple radius for extracting the locally optimal paths and path selection rules that take into account of previously extracted paths are also presented in this chapter. Experiments conducted on 10 low dose chest CT scans showed that locally optimal paths performs better, with more small vessels extracted in comparison to applying a threshold to the response of the filter.

Summary of all the chapters, general discussions and conclusions, and future outlooks are presented in the final chapter.

1.4 Contributions

This thesis consists of six main contributions:

1. **A study on the effects of smoking on CT quantitative measure**: Short term effects that taking up and cessation of smoking has on CT quantitative measure were studied using the developed lung segmentation algorithm. A version of the 15^{th} percentile density of the lungs that

is normalized according to the total lung capacity was used to measure the density of a cohort from the DLCST study. We have observed significant increase or decrease in lung density when subjects start or stop smoking, suggesting the need to take into account of smoking behavior when performing CT density based analysis.

2. **Voxel classification based airway appearance model**: An airway tree appearance model based on voxel classification was introduced. The novelty of the proposed method lies in the usage of easy to obtain low quality airway trees for training purpose. We showed that by using an special set of segmentations designed to reduce false negatives in the training data and by having a sampling scheme that emphasizes on the smaller airways, good results can be achieved even with incomplete airway trees as training data.

3. **Vessel guided approach for airway segmentation**: A way of using segmented vessel trees for improving airway tree segmentation was presented. This is achieved using a vessel orientation similarity measure that compares Hessian derived orientation of an airway candidate voxel with the orientation from the centerline of a nearby vessel. We showed that applying region growing on the vessel orientation similarity measure in combination with the voxel classification based appearance model gives better segmentation results as compared to using the appearance model alone. The method has also been shown to give good results when applied to a diverse set of CT scans.

4. **Construction of airway tree reference using segmentations from different methods**: A method for constructing reference from airway trees segmented by different algorithms is presented, where human observers are given the easier tasks of determining whether a branch segment is segmented correctly or not, instead of segmenting from scratch by hand. Each segmented airway trees is first subdivided into its individual branch segments. Each branch segments is then visually inspected by trained observers to determine whether it is correctly segmented or not. Finally, reference airway trees are constructed by taking the union of all correctly extracted branches.

5. **Comparison of 15 different airway tree extraction algorithms**: It is important to be able to evaluate and compare performance of segmentation algorithms quantitatively. However, because of the difficulty involved in obtaining reference for airway trees, such quantitative evaluation and comparison is almost non-existent for airway tree extraction algorithms. Using a reference constructed from the results of the method to be evaluated, comparison was performed on airway trees segmented by 15 different airway tree extraction algorithms on a standard dataset, which is a task that has never been attempted before.

6. **Extraction of tree structures using locally optimal paths**: A method for extraction of tree structures based on locally optimal paths is proposed. As termination criteria are performed on a path basis, the proposed method is capable of overcoming local occlusions in image data due to e.g. noise. Another advantage of the proposed method is that geometric characteristics of tree structures, e.g. bifurcation angles, number of bifurcations and straightness of a branch, are naturally implemented into the method.

Chapter 2

Automated Lung Segmentation

2.1 Introduction

Segmentation of the lung fields is a critical step for various tasks related to the analysis of the lungs in CT scans. One of the most common usage of lung segmentation algorithms is for the computation of emphysema measures, such as relative area below -950 HU (RA950) and 15^{th} percentile density (PD15) [19]. Lung segmentation algorithms are also commonly used as a preprocessing step for the segmentation of other lung structures and anomalies, such as vessels [1,77], fissures [77,109], lobules [72] and nodules [1]. It has also been shown that using segmented lung fields as a mask in registration related tasks improves registration results as influence from non-lung structures are suppressed [121].

Various work has been done in relation to lung segmentation [94]. The majority of the work is based on region growing and assumes that the lungs in CT scans are objects of lower density in relation to its surroundings [37, 99, 118, 122]. Though this is sufficient for the case of healthy subjects, it is insufficient for cases with dense anomalies within the lungs due to pathologies such as nodules, cystic fibrosis or mesothelioma. In order to be able to correctly segment lungs with dense anomalies, more advanced methods have been proposed at the expense of higher computation cost, such as the use of image registration [93] and shape models [54]. Van Rikxoort et al. [110] proposed a hybrid method, where lungs are segmented using a region growing based method by default and switches to a more computationally expensive registration based method if errors are detected in the segmentation result.

In this chapter, an automated lung segmentation method is proposed, which is based on region growing, similar to [37]. A unique feature of the proposed method is that the separation of the left and right lung fields is performed implicitly by the region growing algorithm. This is in contrast to [37], which relies on a dynamic programming based post processing step that requires prior knowledge of the orientation of the lungs. The reason for the preference of the simpler region growing approach is that the proposed method is meant to be applied to screening CT scans of mainly relatively healthy subjects.

The proposed algorithm also features an esophagus removal scheme, meant for removing possible esophagus regions that are wrongly included by the region growing process. In addition, we also propose an optional hole filling and smoothing scheme to include possible high density regions within the lungs, such as vessels, fissures and small nodules, which uses a coarse airway segmentation to fill up the large vessels in the lungs.

This chapter starts by describing how trachea is detected automatically in a CT scan in Section 2.2, which we use to segment coarse airway tree that contains the major airways with some leakage, a term for false positives in relation to growing based approaches. The coarse airway tree is then used to obtain the left and right main bronchi, which is used for segmenting the left and right lung fields using region growing algorithm as described in Section 2.3. The esophagus removal scheme, and the optional hole filling and smoothing scheme is also presented in the same section. Section 2.4 describes the results of the evaluation conducted. Finally we end this chapter in Section 2.5 with a brief discussion on possible improvements and a conclusion.

2.2 Segmentation of a coarse airway tree

The aim of obtaining the airway tree is two fold: to obtain the left and right main bronchi, which will be used to segment the left and right lungs (described in Section 2.3.2); and for closing up the main vessels that are near the large airways (described in Section 2.3.4). For these purposes, we do not need the airway tree to be segmented accurately, an airway tree that contains the major airways without major leaks will be sufficient, thus the term coarse airway tree. In this section, we first describe how part of the trachea in an image is detected automatically. This is then followed by a description of the algorithm for the segmentation of the coarse airway tree, which is based on fast marching and uses the partly detected trachea as seeds.

2.2.1 Automated trachea detection

The purpose of the automated trachea detection algorithm is to automatically obtain a region within the tracheal lumen, which is used as seed points to obtain the coarse airway tree later. The idea is to detect a cylindrical structure that lies within the top $N_{trachea}$ slices of a chest CT scan. The proposed algorithm involves two stages: detection of round discs in the axial slices and using them to detect a cylindrical structure in 3D.

The first stage uses the fact that trachea generally appears as a dark round disc in axial slices, as shown in Figure 2.1(a). Dark regions in a slice is first extracted by thresholding and retaining voxels with intensities lower than $T_{trachea}$. This is then followed by a connected component analysis, where disconnected components are identified and given different labels. Subsequently, disconnected regions that are touching the border of the scan are considered as background and are removed. The following criteria are then used to filter out non-trachea regions, where a region is retained if it fulfills all the criteria:

1. **Area**: A region must have an area between πR_{min}^2 and πR_{max}^2, where R_{min} and R_{max} are approximately the minimum and maximum radius of the human trachea respectively.

2. **Circularity**: The region must be similar to a circle. This is achieved by enforcing that $1 - (r_{max}/r_{est}) < c_{max}$, where r_{max} is the maximum distance between the points of the region and the centroid of the region, and $r_{est} = \sqrt{A/2\pi}$ with A as the area of the region.

The centroid of the regions the fulfill the criteria are subsequently computed along with the centroid of the foreground. The foreground is defined as a region in the image does not belong to regions previously classified as background. Finally, the region with centroid closest to the centroid of the foreground in the horizontal axis is retained. This uses the observation that trachea, viewed axially, generally lies in the middle of the body in the horizontal axis but not in the vertical axis.

The second stage of cylindrical structure detection is performed once the round discs (possibly belonging to the trachea) in all the top $N_{trachea}$ slices are identified. By scanning in a top to bottom manner, the final trachea region is the first cylindrical region that spans a depth of $d_{trachea}$. Cylindrical regions are formed by grouping overlapping detected discs of neighboring slices together, where a disc in a slice is said to be overlapping with the disc in a neighboring slice if the distance of the centroid of both discs is less than the r_{est} of the former disc.

2.2.2 Coarse airway tree segmentation

An adaptation of the fast marching based algorithm presented in [90] is used to obtain a coarse airway tree segmentation, which we will refer to as the Schlathölter algorithm. The resulting segmented airway tree is in the form of a collection of individual branch segments, where a unique label is assigned to each individual branch segment. This feature of the Schlathölter algorithm makes it possible to easily extract the trachea, left and right main bronchi later.

The key idea of the Schlathölter algorithm is based on the observation that a wave front propagating through a tree structure remains connected until it encounters a bifurcation. The side branches can thus be detected as the individual disconnected components in the propagating front. Another advantage of the algorithm is that possible leakage can also be detected by monitoring changes in the propagating front, which can later be removed from the overall segmentation.

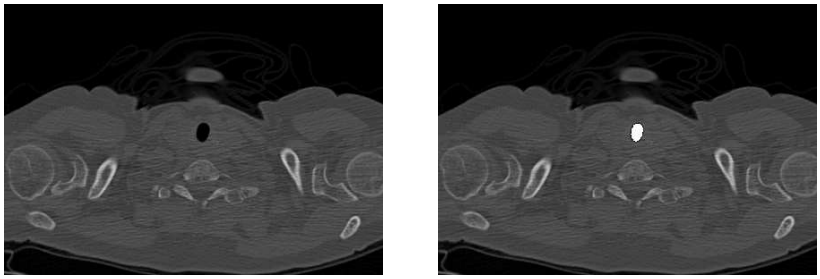

(a) (b)

Figure 2.1: (a) An axial slice of a CT scan with a visible trachea and (b) the same axial slice with the automatically detected trachea highlighted.

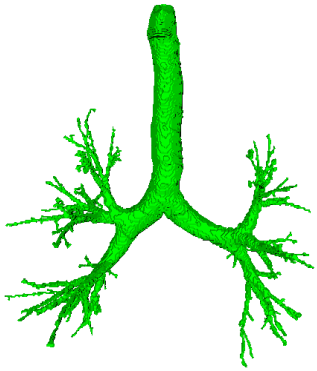

Figure 2.2: Surface rendering of a segmented coarse airway tree.

The detected trachea in Section 2.2.1 is used to initialize the Schlathölter algorithm, where the algorithm was made to propagate to voxels with intensities lower than T_{air}. Bifurcation is detected by monitoring the number of disconnected components in the propagating front. The number of disconnected components in the front is obtained by applying connected component analysis to the set of "trial" points in the fast marching process [63]. Additionally, in order to reduce computation cost, the connected component analysis is only performed when the time stamp from the fast marching algorithm increased by $1/\delta$, where δ is the minimum distance between two voxels.

It is observed that the top part of the trachea is often very noisy, due to reconstruction artifacts from the surrounding dense structures, e.g. the clavicle. Spurious high intensity voxels from such artifacts often cause the propagating fronts to be disconnected, resulting in falsely detected bifurcations. In order to avoid performing bifurcation detection on the top part of the trachea, bifurcation detection is disabled for a length of d_{skip} at the beginning of the trachea. A simple leakage detection rule is implemented, where a branch is discarded if the radius of the propagating front, estimated from the surface area of the front, is α times larger than the radius of the front at the root of the branch. To further prevent the algorithm from leaking and also to save computation time, the algorithm is made to extract at most β branch segments. Figure 2.2 shows the surface rendering of a segmented airway tree obtained using our implementation of the Schlathölter algorithm.

2.3 Segmentation of left and right lung

The trachea, and the left and right main bronchi are extracted from the coarse airway tree obtained in Section 2.2.2, and they are used to initialize a region growing based algorithm for segmenting the left and right lung fields. An esophagus removal process is then applied to the segmented lung fields to remove regions belonging to the esophagus that are wrongly included by the region growing process.

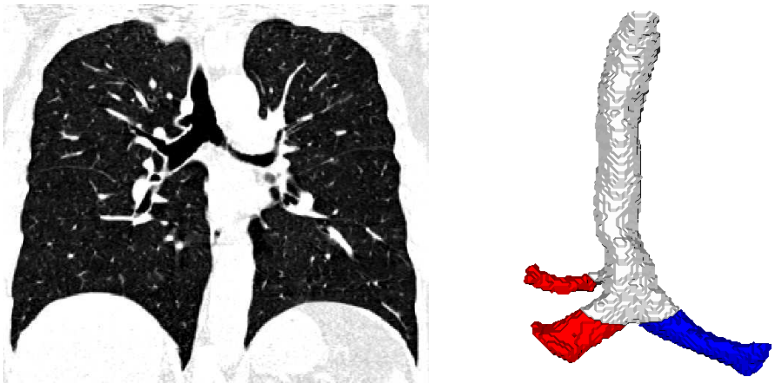

(a) (b)

Figure 2.3: An example of a subject with pig bronchus, showing (a) a coronal view of the CT scan and (b) a surface rendering of the segmented trachea (white), left (red) and right (blue) main bronchi.

As the region growing process assumes that the intensities of the voxels within the lung fields are below a certain threshold, any structures within the lung fields with intensity higher than the threshold will be excluded. As certain applications requires such high intensity structures to be included into the segmented lung fields, an optional smoothing and hole filling process is also introduced. This section starts by describing how the trachea, and the left and right main bronchi are extracted. This is followed by the description of the region growing based algorithm for segmenting the left and right lung. After this, we describe the esophagus removal process, and finally the optional smoothing and hole filling process.

2.3.1 Extraction of trachea, left and right main bronchi

As mentioned in Section 2.2.2, different branches are given different labels in the airway tree segmented using the Schlathölter algorithm. As the Schlathölter algorithm is initialized using partly detected trachea, the trachea is naturally the first branch the algorithm extracts. The main bronchi are then the subsequent two branches that bifurcate from the trachea. Using the centroids of the voxels belonging to the individual branches that are neighboring to the trachea, the branch with the left most centroid is identified as the left main bronchus, while the remaining branch is the right main bronchus.

The detection algorithm described above works well for the majority of the cases, except for the rare anatomical variation called the "pig bronchus" [28], where subjects have an extra tracheal bronchus just above the carina, as shown in Figure 2.3(a). Among the screening scans from approximately 2000 subjects that we have processed, we have encountered around 4 subjects with such anatomical variations.

An extra detection step in the main bronchi extraction is introduced in order to handle the pig bronchus. Comparing the behavior of the bifurcating branches at pig bronchus and trachea to those of the left and right main bronchi, it is observed that the pig bronchus is a lot smaller in radius than the trachea, while the left and right main bronchi are usually of similar radius. Therefore, pig bronchus can be identified easily by comparing the difference between the radius of the bifurcating branches of the trachea. The radius of a branch is approximated as the median of the radii measured at each time stamp interval in the Schlathölter algorithm. At the first bifurcation of a trachea, a pig bronchus is said to be detected if the ratio between radius of the smaller branch and the radius of the larger branch is less than r_{pig}. Upon detection of the pig bronchus, the larger branch will be identified as the trachea, and the left and right main bronchi will be the branches from the next bifurcation. For convenience, we do not assigned a specific label for the pig bronchus, but instead marked is as either left or right main bronchi depending on which lung it branches to. Figure 2.3(b) shows the surface rendering of the main bronchi segmented from a subject with pig bronchus.

2.3.2 Left and right lung segmentation

Our implementation uses voxels from the left and right main bronchi that are neighboring to the trachea as seed points for segmenting the left and right lungs. Ideally, the left and right lungs can be obtained by performing region growing on seed points from the left and right main bronchi respectively. However, in practice, intensity of the pleura separating the left and right lungs can be well within the intensity of lung tissues, causing the region growing processes to leak from one lung to the other.

In order to be able to separate the left and right lungs properly via region growing alone, a scheme involving running two region growing processes (one for each lung) concurrently is proposed. Concurrent execution of both region growing processes is achieved by having each process takes turn in marking one voxel at a time, and both processes are coupled in the following manner:

- **Collision detection**: If a region growing process grows to a voxel that is already marked by the other region growing process, then the voxel will be unmarked as it belongs to the pleura. The voxel will also be prevented from growing further by both processes.
- **Common intensity threshold**: Both region growing processes share the same intensity threshold, which begins at the value T_{min} and is slowly increased up to a maximum value of T_{lung}, after which the region growing processes will then be stopped. Threshold is only increased when both processes have no more neighboring voxels of intensity less than or equal to the current threshold. The increased threshold will be set to the lowest intensity value of the neighboring voxels.
- **Balancing of number of marked voxels**: This is performed if the number of added voxels of a region growing process is more than γ times of the other region growing process and both region growing processes contains neighboring voxels that they can grow to. During the balancing process, the process with the larger number of added voxels is prevented from growing until both process have the same amount of added voxels. The threshold is set to the lowest intensity of the neighboring voxels of both region growing process after the balancing process.

Collision detection is used to prevent both region growing process from growing into each other, with the assumption that voxels where both region growing process meet are low intensity region of the pleura separating the left and right lungs. The use of a common intensity threshold for both region growing processes uses the fact that the pleura has higher intensity than the surrounding lung tissues. Therefore, by slowly raising the threshold of both region growing processes, both region growing processes will converge at the pleura region. In general, collision detection and the use of common intensity threshold are sufficient to extract the left and right lung for most cases. The additional balancing procedure is used to further ensure that both region growing process grow at the same speed and letting the collision detection rule to prevent both regions from crossing the pleura separating the left and the right lungs. The situation where the region growing processes grow unevenly usually arises when one of the lungs is more emphysemic than the other, resulting in the more emphysemic lung to have more low intensity regions.

After the lungs are segmented, the left and right main bronchus obtained in Section 2.3.1 are dilated with a sphere of radius r_{bronc} and subsequently subtracted from the segmented lungs.

2.3.3 Esophagus removal

In rare cases, it has been observed that pleura of separating the lung from the esophagus may have intensity well within the intensity of lung tissues, causing the region algorithm to mark part of the esophagus as lungs. Among the screening CT scans processed, this has happened on approximately 2% of the scans. Therefore, an esophagus detection and removal process is introduced to address this issue.

We propose to detect esophagus by first scanning for possible esophagus candidates on a slice by slice manner, and then identify actual esophagus as weakly connected structures within the segmented lungs that have a high overlap with the esophagus candidates. By applying connected components analysis on all axial slices containing the lung segmentation independently, esophagus candidates at each slice are identified as disconnected regions with left lung on its left side and right lung on its right

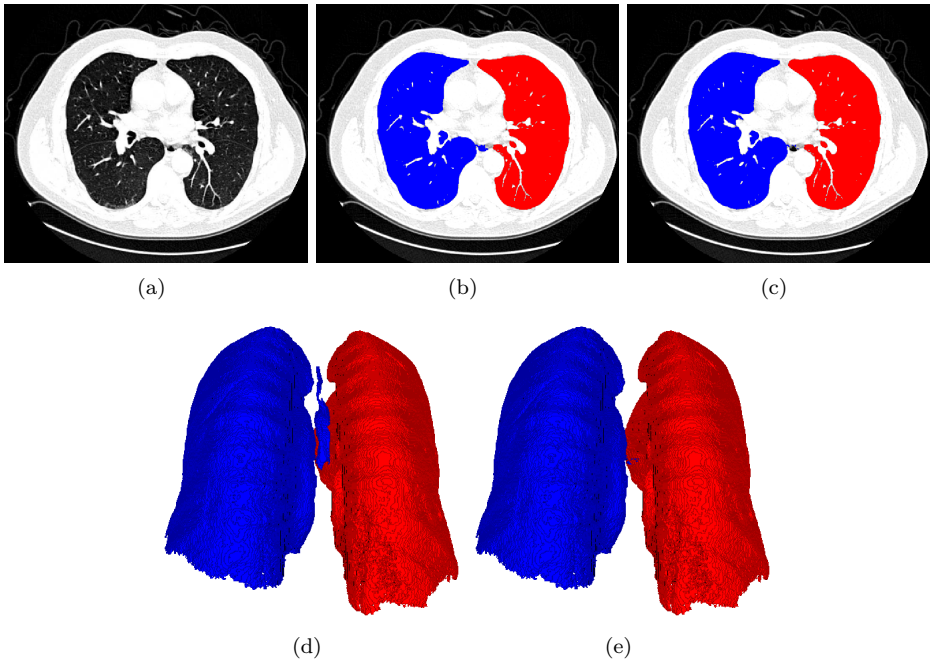

Figure 2.4: An example showing (a) an axial slice of a CT scan, and the same scan overlaid with the lung segmentation (b)without and (c) with esophagus removal, and the surface renderings of the same lung segmentation (d) without and (e) with esophagus removal. Left and right lung fields are indicated in red and blue respectively.

side. Next, erosion with a sphere element of one voxel radius is applied to the segmented lungs to disconnect any weakly connected regions within the segmented lungs. Finally, connected component analysis is applied to the eroded lungs, and any disconnected components with an overlap of more than $p_{overlap}$ with the esophagus candidates are dilated with the one voxel sphere element and removed from the segmented lung fields. An example of the result from the proposed esophagus removal algorithm is shown in Figure 2.4, where it can be observed that, except for a few voxels, the esophagus has been completely removed from the segmented lung fields.

2.3.4 Smoothing and removing holes in segmented lungs

The segmented lung fields obtained previously only consist of parenchyma tissues, which are assumed to be of intensity lower or equal to T_{lung}. This implies that structures with high intensity such as airway walls and vessels are not included in the segmented lung fields. Although this is sufficient for most applications, there are some applications that needed segmented lung fields that do not have holes in it and include all the high intensity structures within the lung fields. One such situation is when the segmented lung fields are meant to be used as masks for segmenting other structures within the lungs, such as airways or vessels.

We propose a two step smoothing and holes filling process, where the first step focuses on filling up small holes within the lungs and the second step focuses on filling up the large vessels in the lungs. This smoothing and holes filling process is performed on each lung individually, removing the need to handle the complications that arise when morphological dilation is applied to the left and right lung fields.

The first step of removing the small holes within a lung starts with the morphological dilation of the segmented lung. Regions belonging to the background that are outside the lung can then be identified by applying region growing on regions that are not marked as lung, with the border of the image as seeds. The remaining non-background region will then be the dilated lung with all holes filled. Finally, morphological erosion is applied on new segmented lung to reduce the effects of the

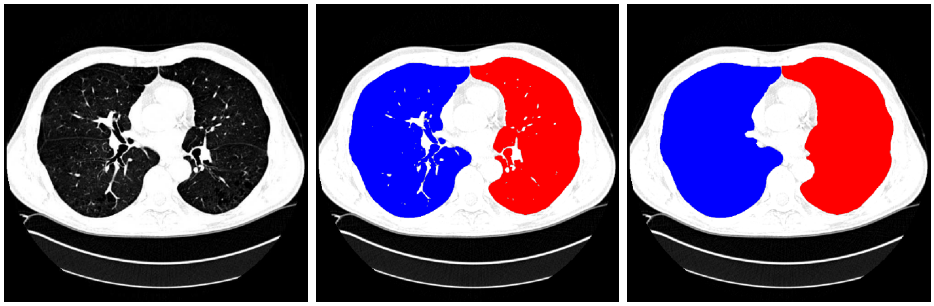

(a) (b) (c)

Figure 2.5: An axial slice showing (a) the original image, segmented lung fields (b) without and (c) with smoothing and holes removal. Left and right lung fields are indicated in red and blue respectively.

dilation applied earlier. A sphere of radius r_{small} is used by both the dilation and erosion operation in this first step.

The second step of filling up the large vessels makes use of the fact that large vessels are near the airways. Excluding the trachea and the left and right main bronchi, the coarse airway tree obtained in Section 2.2.2 is dilated with a large sphere of radius r_{large}, and merged with the resulting lung from the first step. The use of this large dilation element will effectively close off part of the large vessels around the airways, separating the rest of the large vessels from the background region. This is then followed by a modified erosion process, using the same sphere element, to remove dilated regions that are outside the lung. In this modified erosion process, the erosion process only removes voxels that do not belong to the lung segmentation prior to merging with the dilated coarse airway tree. Finally, the same hole filling process as described previously is applied to the processed lung segmentation to fill the regions belonging to the large vessels that are not close off earlier. Figure 2.5 shows an example of a lung segmentation with and without the smoothing and holes removal process.

2.4 Experiments and results

The proposed lung segmentation algorithm has been applied to 6830 low dose screening images from the Danish Lung Cancer Screening Trial (DLCST) study [80], with the values of the parameters as listed in Table 2.1. Among the segmented scans, the proposed algorithm only failed to segment 42 scans due to failure in detecting the trachea (34 scans), error in extracting the main bronchi due to leakage detected at the main bronchi level (3 scans), and having the segmented region leaked into the background region because the lung fields were clipped during acquisition (5 scans).

Two medical doctors experienced in chest CT, Haseem Ashraf and Goutham Edula, have visually evaluated 200 CT scans, which were selected from the first 3500 available scans of the DLCST study. Consensus of the evaluation results was reached with the aid of a pulmonologist, Asger Dirksen, who specialized in chest CT. Among the selected scans, 100 scans were selected randomly, and the remaining 100 scans were selected randomly from a list of outliers. The list of outliers were compiled from series of measures, consisting of 50 scans with the highest measurements and 50 scans with the lowest measurements from each of the measures. The series of measurements used were lung volume, lung weight, lung surface area, average lung intensity, 15^{th} percentile density (PD15), and relative area below -950 HU (RA950). The human observers were to identify the errors and classify them into one of the seven types of errors: lung separation error, esophagus inclusion, bronchial separation error, lung fields excluded due to consolidation/pneumonia, air pockets missed, bowel inclusion and error due to artifacts. Besides identifying the type errors, observers also need to assign one of the three scores to each error indicating the effects of the error on the overall lung fields: less than 1%, between 1 to 5%, and more than 5% of the total lung fields. It should be noted that the observers understood that the scores are not meant to reflect the exact amount of errors, but are actually meant to indicate whether the errors are negligible, minor or major.

Table 2.1: List of parameters and their corresponding values.

$N_{trachea}$	50
$T_{trachea}$	-400 HU
R_{min}	5 mm
R_{max}	17 mm
c_{max}	0.6
$d_{trachea}$	20 mm
T_{air}	-900 HU
d_{skip}	10 mm
α	3
β	300
r_{pig}	0.4
γ	5
T_{min}	-1000 HU
T_{lung}	-400 HU
$p_{overlap}$	90%
r_{small}	2.5 mm
r_{large}	15 mm
r_{bronc}	2 mm

Among the scans evaluated, errors were identified in nine scans. The majority of the errors, consisting of six out of the nine scans with errors, were due to air pockets missed though their effects to the lung segmentation were negligible as the coverage was less than 1% (negligible) of the lung for all cases. Two scans were identified with esophagus error due to a few voxels in the esophagus that were not removed properly by the esophagus removal algorithm. Only one scan had an error coverage between 1 to 5% (minor) due to the inclusion of bowels.

Besides the CT scans from the DLCST study, the algorithm has also been applied to scans from other dataset, such as chest CT scans of babies from Princess Margaret Hospital for Children in Perth (Australia), thick slices (5mm) scans of patients with cystic fibrosis from Erasmus MC Sophia Children Hospital in Rotterdam (the Netherlands), chest CT scans of various qualities from EXACT'09 [59], and 4D CT scans from the Deformable Image Registration (DIR) dataset [15]. For the CT scans of babies, manual placement of a seed in the trachea was required because the trachea radius for babies was a lot smaller than what the automated trachea detection was designed for. For the thick slices, the algorithm was modified to include left and right main bronchi in the lung segmentation, due to difficulties in segmenting the left and right main bronchi reliably caused by the lack of resolution in the z-axis.

2.5 Conclusion

In conclusion, we have proposed a fully automated region growing based lung segmentation algorithm that is meant for screening CT scans. The proposed algorithm has been successfully applied to >6000 screening chest CT scans from the DLCST study, with a failure rate of less than 1% (42 out of 6830 scans). Majority of the failures are caused by failure in detecting the trachea, either due to acquisition errors (inclusion of a large part of larynx) or reconstruction artifacts. Manually placing a point within the tracheal lumen for initialization purpose is usually sufficient to overcome the problem. Manual evaluation has been performed on 200 scans selected randomly from the first 3500 available scans from the DLCST study, where the results from the proposed method has been shown to be highly accurate, with only minor or negligible errors in a small number of cases. Despite the original aim of applying to screening CT scans, the proposed algorithm has been applied to various clinical chest CT scans of pathological subjects successfully with little or no modifications. An explanation for this is probably due to the absence of large dense pathologies in the scans applied. It is expected that the proposed lung segmentation algorithm will not be as effective on such scans mainly due to the assumption that the lungs are objects of low intensity CT.

Chapter 3

Short Term Effects of Changes in Smoking Behavior on Emphysema Quantification by CT

This chapter is based on the manuscript "Short Term Effect of Changes in Smoking Behaviour on Lung Density by Computed Tomography", by H. Ashraf, P. Lo, S. B. Shaker, M. de Bruijne, A. Dirksen, P. Tønnesen, M. Dahlbäck, J. J. H. Pedersen, Submitted, 2010.

Abstract *Background:* We studied the effect of smoking cessation and smoking relapse on lung density using low-dose CT. Methods: From a Cancer Screening Trial, 726 current and former smoking participants (>20 pack-years) were included, where low dose spiral computed tomography (CT) scan was performed using multi-detector CT scanner. Lung density was quantified using the 15th percentile density (PD15), which was adjusted to the predicted total lung capacity. Data was analyzed by linear regression models.
Results: At baseline, mean PD15 was 45 g/L in former smokers ($n = 178$) and 55 g/L in current smokers (n=548), making a difference of 10 g/L ($p < 0.001$). After smoking cessation ($n = 77$) PD15 decreased by 6.2 g/L ($p < 0.001$) in the first year and an additionally 3.6 g/L ($p < 0.001$) in the second year, after which no further change could be detected. Moreover, the first year after smoking relapse ($n = 18$) PD15 increased by 3.7 g/L ($p = 0.02$).
Conclusions: Current smoking status has great influence on lung density by CT. The difference in lung density between current and former smokers observed in cross-sectional studies corresponds closely to the change in lung density seen in the years after smoking cessation. Therefore, current smoking status should be taken into account when using CT lung density to assess the severity of diseases such as emphysema.

3.1 Introduction

Changes in lung density are important characteristics of lung diseases such as emphysema, pneumonia and pulmonary fibrosis. As the measurement of CT is based on the attenuation of X-rays, which is related to the density of the tissues that is penetrated by the X-rays, this makes CT ideal for the diagnosis of these density related lung diseases. In other words, CT is essentially densitometry, where the density within a particular cube, commonly referred to as voxel, is reflected by its gray levels or Houndsfield unit in a CT image. The densitometry nature of CT has been used for monitoring diseases like emphysema, where loss of lung tissue plays a central role [10, 98].

Pulmonary emphysema is a condition characterized by low lung density. It is defined as abnormal, permanent enlargement of airspaces distal to the terminal bronchioles, accompanied by the destruction

of their walls, and without obvious fibrosis [95]. Emphysema leads to loss of pulmonary function (e.g. decline in forced expiratory volume in 1st second (FEV_1)), which leads to respiratory insufficiency and ultimately death [123]. The precise mechanism behind the destruction of alveoli and development of emphysema from smoking is not fully understood. Recent studies highlight the central role of inflammation in the pathogenesis of Chronic Obstructive Pulmonary Disease (COPD) [65, 113]. Smoking is believed to be the main cause of inflammation both in the lung and systemic [88,105]. Inhaled steroids have shown little effect in COPD [112], and abstaining from smoking is still the most important intervention [85]. Studies have shown a beneficial effect of smoking cessation on cough, sputum production and FEV_1 [43]. Fletcher and Peto observed in their landmark study that decline in FEV_1 decreased after smoking cessation [25]. More recently these findings were reproduced in another large landmark study, the Lung Health Study, that showed a slight increase in FEV_1, for the first couple of years after smoking cessation, and thereafter a smaller decline in FEV_1, as compared to the decline observed in continuous smokers [89]. This again underlines the importance of smoking cessation in the treatment and prognosis of COPD.

The effect of smoking cessation on the underlining inflammation present in COPD patients is still a matter of debate. Studies have found that some inflammation may persist after smoking cessation [27,103]. Others have found a clear reduction in inflammatory biomarkers in both blood and bronchial fluids [51]. However, it is generally believed that inflammation plays an important role in the development and progression of emphysema, and that smoking cessation interferes with inflammatory mediators [35]. Most studies have focused on pulmonary function tests (PFT), blood samples and bronchial fluids, and little is known about the short term morphological changes that occur in relation to changes in smoking behavior.

The purpose of this study was to evaluate the short term effect of changes in smoking behavior on lung density both cross-sectionally and longitudinally using repeated CT scans.

3.2 Material

3.2.1 Study population

The study population was selected from the Danish Lung Cancer Screening Trial (DLCST) [3, 80]. DLCST is a 5 year trial investigating the effect of screening with low dose CT on the mortality of lung cancer. In 2005 participants were randomized to either annual CT or a control group. At the time when we decided to perform the present study, 726 participants had been randomized to CT and completed baseline and 1 year follow-up scan, and they were included in the present study. The study was institutional review board approved.

The inclusion and exclusion criteria of DLCST have been published previously in [80]; in short participants were current or former smokers at an age between 50 to 70 years with a smoking history of more than 20 pack years. Former smokers were only included if they had quit smoking after the age of 50 years and less than 10 years before inclusion. FEV_1 was at least 30% of predicted normal. Ineligible were those applicants with body weight above 130 kg or previous treatment for lung cancer, breast cancer, malignant melanoma or hypernephroma. Individuals with a history of any other cancer within 5 years or tuberculosis within 2 years or any serious illness that would shorten life expectancy to less than 10 years were excluded.

3.3 Methods

3.3.1 Imaging

All CT scans were performed on a Multi Detector Computed Tomography (MDCT) scanner (16 rows Philips Mx 8000). Scans were performed supine after full inspiration with caudocranial scan direction including the entire ribcage and with a low dose technique with 140 kV and 40 mAs. Scans were performed with spiral data acquisition with the following acquisition parameters: Section collimation 16×0.75 mm, pitch 1.5 and rotation time 0.5 second. Images were reconstructed with 1 mm slice thickness using a hard algorithm.

3.3.2 Image analysis

Images were analyzed with the lung segmentation algorithm described in Chapter 2 without the optional smoothing and hole removal process. Based on the voxel dimensions, the volume of a single voxel was calculated, and from this the total lung volume (TLV) was computed by adding up the volume of voxels marked as lung. Assuming the density value of a single voxel can be converted from Houndsfield Unit (HU) to the physical unit of gram per liter (g/L) by adding a value of 1000, the lung weight based on density value from CT can be obtained by summing the converted value in g/L, followed by a multiplication with the volume of a single voxel.

The 15th percentile density (PD15) was calculated as the threshold in HU where 15% of the voxels within the segmented lung fields have density values below the threshold [17, 19]. As the density of the lung is dependent on the amount of air in the lung, the adjustment of the PD15 based on [91] was introduced in order to eliminate noise due to variations in inspiration level:

$$\text{Adjusted PD15} = \frac{(\text{PD15} + 1000) \times \text{TLV}}{\text{TLC}}$$

where TLC is the predicted total lung capacity, which is derived from reference equations based on the participant's sex and height.

Note that we will refer to the adjusted PD15 as PD15 or lung density in the rest of this chapter for simplicity.

3.4 Assessments

At baseline and 1 year follow-up, smoking status was determined (self-reported) along with carbon monoxide (CO) level in exhaled air. A CO level above 10 parts per million (ppm) was defined as indicating current smoking [69], and participants who claimed to be former smokers with CO $>$ 10 ppm at baseline or follow-up were excluded from the study because of contradictory information about their smoking status. Smoking habits were further explored with a questionnaire, where cigarettes smoked per day in the last month (0-10, 11-20, $>$20), number of pack years, and for former smokers the year of smoking cessation was determined.

3.5 Definitions and design

Data was collected prospectively and was analyzed both cross-sectionally (by comparing groups and subgroups) and longitudinally (within an observation window) as described below. Former smokers were defined as participants who had abstained from smoking for at least 4 weeks prior to the base-line screening visit. Participants were observed in a 1-year window from baseline to 1-year follow-up, and were divided into 4 groups based on their smoking behavior in this window:

- *Continuous smokers:* baseline smokers who were still smoking at 1-year follow-up,
- *recent quitters:* baseline smokers who had quit smoking at least 4 weeks prior to 1-year follow-up,
- *continuous ex-smokers:* baseline ex-smokers who did not smoke at 1-year follow-up, and
- *re-starters:* baseline former smokers who had resumed smoking at 1-year follow-up.

All continuous ex-smokers had stopped smoking within the last 10 years before inclusion (i.e. 1995-2004), and they were subdivided into 5 subgroups according to how many years they had not smoked at baseline: 1 year, 2 years, 3 years, 4 years and $\geq$5 years. By calculating the change in lung density in the observation window from baseline to 1-year follow-up for these subgroups, change in lung for each of the first 10 years after smoking cessation could be estimated.

Table 3.1: Baseline characteristics of participants. SD indicates standard deviation.

Characteristics	Smoking status at baseline		Statistic
	Current ($n = 548$)	Former ($n = 178$)	(p value)
Gender, Male/Female (n)	295/253	98/80	0.84
Mean age (yrs) (range)	58.0 (49-71)	58.2 (50-69)	0.62
Mean pack years (SD)	36 (12)	35 (12)	0.36
Mean BMI (SD)	24.9 (3.9)	26.2 (3.6)	<0.001
Mean FEV_1 (SD)	2.8 (0.7)	3.0 (0.8)	0.01
Mean Predicted % FEV_1 (SD)	92% (17)	96% (17)	0.004
Mean FEV_1/FVC (SD)	70% (7.5)	72% (7.3)	0.001

3.6 Statistics

The distribution of PD15 was approximately normal, and the influence of smoking behavior on lung density by CT was analyzed in two linear models, which were a cross-sectional model and a longitudinal model. In the cross-sectional model, only baseline scans were analyzed, with smoking status, sex, age, pack years and body mass index (BMI) as explanatory variables, and PD15 as the outcome. In the longitudinal model, the difference in PD15 between baseline and 1 year follow-up (ΔPD15) was used as the outcome, and was analyzed with time between scans, sex, year of smoking cessation, smoking relapse and baseline PD15 as explanatory variables. All analyses were performed using R version 2.7.1 and a p value less than 0.05 was considered to be statistically significant.

3.7 Results

Baseline characteristics of participants ($n = 726$) are shown in Table 3.1. One former smoker was excluded from the study because of a CO value above 10 ppm. At 1 year follow-up 471 participants were continuous smokers, 77 were recent quitters, 160 were continuous ex-smokers and 18 were re-starters.

3.7.1 Cross-sectional analysis of baseline scans

Smoking status had great influence on lung density at baseline; mean PD15 was 44.9 g/L in former smokers and 55.0 g/L in current smokers. The difference between the two groups was 10.2 g/L ($p < 0.001$). The influence of other variables was studied in the cross-sectional model. The difference in PD15 persisted, with a difference of 10.6 g/L ($p < 0.001$), even after adjustment for female gender (14.9 g/L, $p < 0.001$), age (-0.36 g/L/year, $p < 0.001$), BMI (0.19 g/L, $p = 0.14$) and pack years (0.1 g/L, $p < 0.001$).

A dose response relationship was assessed by further subdividing the current smokers into different categories based on the average amount of cigarettes smoked per day in the last month, where the following dose response in relation to the former smokers were observed: 5.7 g/L for 0-10 cigarettes per day ($n = 85$, $p < 0.001$), 10.6 g/L for 11-20 cigarettes per day ($n = 244$, $p < 0.001$) and 11.4 g/L for >20 cigarettes per day ($n = 158$, $p < 0.001$).

3.7.2 Longitudinal analysis of baseline and follow-up scans

The change in lung density between baseline and 1 year follow-up was analyzed in a longitudinal model, the results of which are shown in Table 3.2. In the recent quitters, a significant difference in ΔPD15 of -6.2 g/L ($p < 0.001$) was observed when compared to the ΔPD15 of the continuous smokers. Among the continuous ex-smokers, significant difference between the ΔPD15 (-3.6 g/L, $p < 0.001$) was only observed for the group where smoking cessation occurred in the year preceding baseline. For the rest of the continuous ex-smokers where smoking cessation occurred more than 1 year before baseline, no significant differences in ΔPD15 (<1 g/L, $p > 0.1$) were observed when compared to continuous

Table 3.2: Longitudinal linear regression analysis of change in lung density during follow-up.

Explanatory variable		Coefficient g/L	p value
Time (years)		-0.9	0.009
Gender (female)		-0.9	0.03
Smoking cessation between baseline and follow-up		-6.2	<0.001
Smoking cessation before baseline (years before baseline)	1 year ($n = 47$)	-3.6	<0.001
	2 years ($n = 26$)	0.1	0.92
	3 years ($n = 16$)	-0.5	0.74
	4 years ($n = 10$)	0.6	0.67
	$\geq$5 years ($n = 68$)	-1.0	0.20
Smoking relapse between baseline and follow-up ($n = 18$)		3.7	0.02
Baseline PD15 (individual value - mean)		-0.1	<0.001

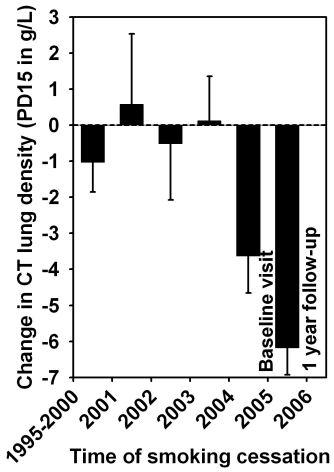

Figure 3.1: Loss of lung density at follow-up in relation to year of smoking cessation. The error-bars indicate standard error of mean.

smokers as shown in Figure 3.1. A modest difference in ΔPD15 of 3.7 g/L ($p = 0.02$) was observed when comparing re-starters to the continuous smokers.

By subdividing the recent quitters into subgroups based on the average amount of cigarettes smoked per day at baseline, the following difference in ΔPD15 in comparison to the continuous smokers was observed: -3.2 g/L for 0-10 cigarettes/day ($n = 16$, $p = 0.04$), -6.1 g/L for 11-20 cigarettes/day ($n = 36$, $p < 0.001$), and -8.8 g/L for >20 cigarettes/day ($n = 17$, $p < 0.001$), again showing a dose-response relationship.

3.8 Discussion

The Danish Lung Cancer Screening Trial constitutes a unique opportunity for analyzing the effect on CT lung density of smoking behavior. This study aims at studying the short term effects on CT based lung density measures due to changes in smoking behavior, where very little is known. Although Soejima et al. [96] studied the relationship between lung density and smoking, it should be noted that they only studied the long term effects of smoking as their study did not include any subjects who changed their smoking behavior during the study.

We found large changes in CT lung density in relation to various smoking behaviors. It was observed that lung density of current smokers was 10 g/L ($p < 0.001$) higher than former smokers.

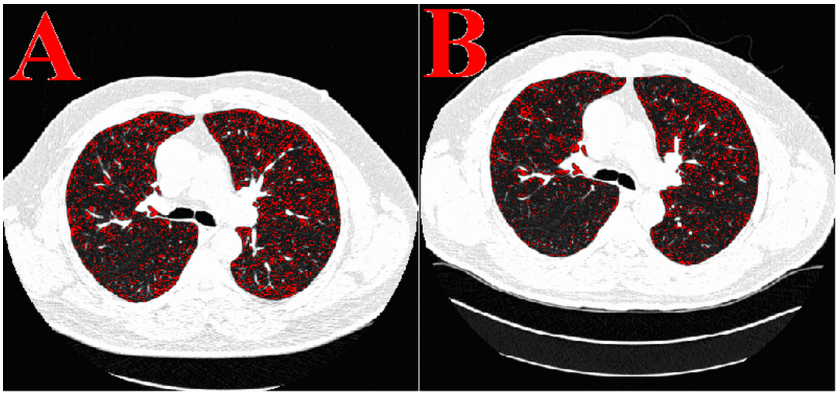

Figure 3.2: Transverse CT scans from a participant who started smoking between baseline visit (A) and 1 year follow-up (B). Slice position and inspiration level was similar in the images (ΔCT volume = 0.04 L). Red areas highlight areas with lung density below -950 HU. Smoking relapse hides underlying low attenuation areas at follow-up.

Accumulation of soot and tar in the lungs (anthracosis) from smoking may explain the higher lung density among current smokers [36]. This accumulation of foreign material provokes inflammation, and the presence of inflammatory cells in the lung contributes to the higher density. Studies have shown that inflammation is present in active smokers [88,105]. We found a clear dose response effect of cigarette consumption on lung density in current smokers, which strongly supports the hypothesis that smoking results in more dense lungs. This is also in line with what was found by Kuschner et al. [50], where dose response relationship between the amount of cigarettes smoked and the inflammatory response was observed.

The cross-sectional difference in CT lung density of 10 g/L between current smokers and former smokers corresponded nicely to the rather dramatic changes in lung density observed in the first couple of years after smoking had stopped. Thus, during the first year after smoking cessation lung density decreased by 6.2 g/L, and additional 3.6 g/L ($p < 0.001$) was lost during the second year after smoking had stopped (Table 3.2). Additional loss of lung density was not observed for former smokers who stopped smoking for more than 2 years. This is consistent with the Lung Health Study [89] in which a beneficial effect of smoking cessation on pulmonary function was observed for 1-2 years, and thereafter, the decline in pulmonary function was similar to the decline in non-smokers. During the first couple of years after smoking cessation the lung probably undergoes a cleansing process where soot, tar and inflammation gradually diminish. Previous studies have shown decreased inflammatory response after smoking cessation [51]. Again we found a dose response effect of cigarette consumption at baseline and loss of lung density after smoking cessation. This indicates that the effects of the cleaning process after smoking cessation is proportional to the amount of cigarettes smoked.

Smoking relapse increased lung density by 3.7 g/L, which is less than the difference of 10 g/L between current and former smokers seen in the cross-sectional analysis. Despite having relatively few re-starters ($n = 18$) and a broad confidence interval (95%: 0.5 - 6.9 g/L), the finding that smoking relapse increases lung density was statistically significant ($p = 0.02$). An explanation for the relatively small increase in lung density for re-starters is probably because it takes some time before a full blown inflammatory process is induced by the accumulation of soot and tar in the lung (Figure 3.2). We expect the lung density to rise for the next several years, provided that smoking is sustained. However, data supporting this hypothesis is not yet available.

Smoking induces emphysema and alveolar destruction, which causes loss of lung density, and therefore smoking has usually been associated with a decrease in lung density [17]. In this study, we observed that smoking cessation is also associated with an intensified decrease in lung density, though only for a couple of years. Therefore, when using CT lung density as outcome measure in clinical trials of COPD, where areas of low density or attenuation are used as a surrogate marker for emphysema [10, 98], it is important to take into account the short term decrease of lung density due to smoking cessation and not misinterpret it as progress of emphysema (Figure 3.3).

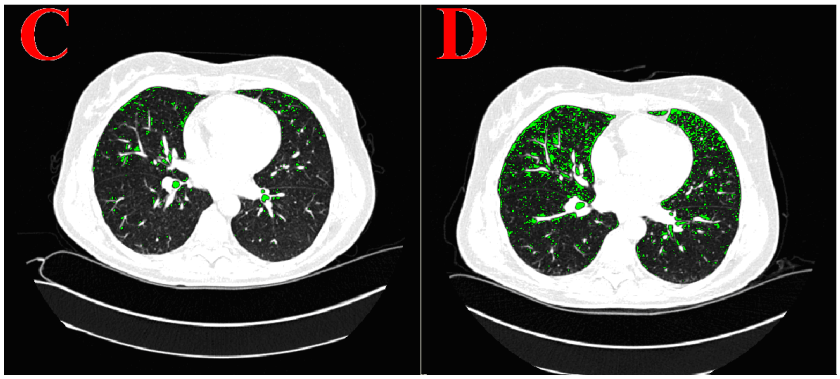

Figure 3.3: Transverse CT scans from a participant who stopped smoking between baseline (C) visit and 1 year follow-up (D). Slice position and inspiration level was similar in the images (ΔCT volume = 0.08 L). Green areas highlight areas with lung density below -950 HU. Smoking cessation revealed more low attenuation areas at follow-up.

Our study showed women have more dense lung (14.9 g/L, $p < 0.001$) than men, which is in agreement with recent studies on gender differences in emphysema score by CT [31]. We also found that the annual loss of lung density was 0.9 g/L larger for women than for men ($p = 0.03$, Table 3.2) supporting previous studies which have shown that women are more susceptible to the deleterious effects of cigarette smoke and more liable developing COPD [84].

Major strengths of this study is the fairly equal distribution of gender in the subjects, the use of CO validated smoking habits, usage of contemporary imaging techniques, and that analyses were performed using linear modeling techniques that focused on statistical noise reduction. To further strengthen the validity of this study, a priori adjustment of PD15 using a physiological model based on the inverse relationship between volume and density [17, 91] that is caused by different level of inspiration during scan acquisition, which is a known principal clinical confounder of CT based lung density measurements.

Other densitometric parameters have been used in previous CT based lung density studies, such as the conventionally used relative area (RA) of emphysema [96]; i.e. the per cent of the lung below a threshold of typically -950 HU. There are several reasons why we chose to use PD15, instead of the conventionally used RA. The first reason is that the rate of decline in PD15 has been shown to be consistent across a wide spectrum of disease severity, whereas the progression of RA increases with greater disease severity [78]. PD15 has also been recommended as a primary outcome measure by the workshop on quantitative computed tomography scanning in longitudinal studies of emphysema [76]. Furthermore, PD15 has been gradually accepted as the most sensitive parameter for CT lung densitometry [79].

There are some limitations to this study. First, never-smokers were not included in the study; this could have given a more direct assessment of the effect of smoking. Secondly, the time at which any change in smoking habit occurred is not very precise. We know that a change occurred at some time between baseline visit and 1 year follow-up, or for smoking cessation before baseline the year of smoking cessation is known. A more precise time frame would make it possible to conduct an even more comprehensive analysis of how the effects of changes in smoking behavior develop.

This study used hard reconstruction images with a slice thickness of 1 mm, which is different to the 3-5 mm slice thickness and soft reconstruction that is commonly recommended for lung density measurements [17]. The main reason for this was because the scans were primarily performed as part of a screening program for lung cancer, where thin slices and hard reconstruction is usually recommended. However, we believe scan settings had little influence on the results because this study focused mainly on changes in lung density over time from scans of the same subject using the same scanner settings.

We believe that further follow-up of the participants could be of interest, and may bring further insight into the effects of smoking on lung density by CT. Currently, we are in the process of waiting

for more data in order to be able to perform further follow-up analysis on the participants.

In conclusion, changes in smoking behavior have great influence on lung density by CT. Cross-sectionally we found 10 g/L ($p < 0.01$) higher lung density in current smokers as compared to former smokers, and this difference was longitudinally accounted for by changes seen in participants who stopped smoking, showing a decrease of 6.2 g/L ($p < 0.001$) in the first year and 3.6 g/L ($p < 0.001$) in the second year after smoking cessation when compared to continuous smokers. Furthermore, smoking relapse at 1 year follow-up was associated with an increase in lung density of 3.7 g/L ($p = 0.02$). This indicates that the decontamination of the lung after smoking cessation lasted for more than a year, which is consistent with previous pulmonary function based studies. Gradual remission of smoke induced inflammation probably in part explains the protraction. In short, current smoking status should be taken into account when evaluating lung density by CT and quantifying the progress of emphysema.

Chapter 4

Voxel Classification Based Airway Tree Segmentation

This chapter is based on the manuscript "Vessel-guided Airway Tree Segmentation: A Voxel Classification Approach", by P. Lo, J. Sporring, H. Ashraf, J. J. H. Pedersen and M. de Bruijne, in Medical Image Analysis, To appear, 2010.

Abstract This chapter presents a method for airway tree segmentation that uses a combination of a trained airway appearance model, vessel and airway orientation information, and region growing. We propose a voxel classification approach for the appearance model, which uses a classifier that is trained to differentiate between airway and non-airway voxels. This is in contrast to previous works that use either intensity alone or hand crafted models of airway appearance. We show that the appearance model can be trained with a set of easily acquired, incomplete, airway tree segmentations. A vessel orientation similarity measure is introduced, which indicates how similar the orientation of an airway candidate is to the orientation of the neighboring vessel. We use this vessel orientation similarity measure to overcome regions in the airway tree that have a low response from the appearance model. The proposed method is evaluated on 250 low dose computed tomography images from a lung cancer screening trial. Our experiments showed that applying the region growing algorithm on the airway appearance model produces more complete airway segmentations, leading to on average 20% longer trees, and 50% less leakage. When combining the airway appearance model with vessel orientation similarity, the improvement is even more significant ($p < 0.01$) than only using the airway appearance model, with on average 7% increase in the total length of branches extracted correctly.

4.1 Introduction

Chronic Obstructive Pulmonary Disease (COPD) is among the leading causes of death and disability in the world, tending to be even more widespread in the future [73, 87]. Measurement of airway lumen dimension and wall thickness, as can be obtained from computed tomography (CT) images, play a significant role in the analysis and understanding of COPD in various studies [9, 18, 75], where measurements from the smaller and higher generation airways are especially important [53]. The success of such studies relies heavily on the availability of accurate and automated methods for airway tree segmentation. However, most airway tree segmentation methods are still limited to the larger and more visible airways, therefore there is an immediate need for a better airway tree segmentation method. Moreover, the lungs are anatomically divided into subregions based on the structure of the airway tree. This makes airway tree segmentation a useful starting point for tasks such as the

segmentation of lobes [49, 104, 122] and pulmonary segments [72]. Segmented airway trees can also be used as landmarks for guiding registration processes (see for instance [55]), resulting in a more accurate and natural transformation for applications such as disease progression monitoring [29].

The general approach to segmentation of the airway tree involves variants of region growing applied on the image intensity [4, 46, 47, 71, 90, 92, 97, 100]. The assumption is that in CT images, the airway lumen is dark and surrounded by brighter structures, i.e. airway walls followed by lung parenchyma. The main problem with this approach is that there often exist small regions, where part of the airway wall is not visible and the airway lumen has intensities similar to the surrounding lung tissue, due to noise or pathologies such as emphysema. This results in 'leakage' in the region growing process in which surrounding lung regions are wrongly labeled as part of the airway tree.

One direct way to reduce leakage is to introduce prior knowledge of the geometry of the airway tree into the region growing algorithm. [71] proposed to monitor the change in volume of the labeled region to detect leakage, and use the highest threshold without any leakage detected to segment the entire tree. Later works focused on the idea of stopping the segmentation locally where leakage occurs, while allowing the segmentation process to continue in other regions [47, 90, 100, 106]. Detection of leakage via the radius of propagating fronts from the fast marching algorithm was introduced in [90]. Van Ginneken et al. [106] replaced the fast marching with a sphere-constrained region growing and investigated a multi-threshold scheme. Both [47] and [100] proposed to use geometrical properties within a volume of interest derived from previously detected airways, where the former used the area of cross sections, and the latter used the topology of the thinned structure for leakage detection. [92] proposed information gain as a region growing criteria to avoid leakage, where the local topology of the labeled region around a candidate voxel is implicitly included into the gain.

Leakage may also be avoided by improved differentiation between airway lumen and surrounding lung tissue. The proposed method falls in this category. The key idea is to base the decision in the region growing not only on the intensity of a single voxel, but also on the information from the surroundings. Sonka et al. [97] used the proximity of airways and vessels as one of the criteria for region growing. Various morphological operators designed specifically for detecting airways have also been investigated [4, 46, 83]. Fetita et al. [23] coupled morphological operators with an energy based reconstruction method that takes into account the appearance of a bronchial tree. A combination of fuzzy logic rules and 2D template matching for segmenting airways was presented in [67]. Ochs et al. [77] presented a pattern recognition technique to classify various structures in lung CT images, including airways, on the basis of training points that were hand picked by experts. Graham et al. [30] presented an airway segmentation algorithm that detects tube parts throughout the image, where the final segmentation is obtained by combining the detected tubes using a graph search technique.

Our contribution is two fold. Firstly, we introduce an airway appearance model that automatically learns the characteristic appearance of the airways and the surrounding tissues from a set of segmented example images. The core of this appearance model is a classifier that is trained to differentiate between airway and non-airway voxels using a set of local image descriptors. We show that good results can be achieved without the need for high quality and complete airway tree segmentations as training data. The idea to use voxel classification for airway segmentation is similar to [77]. However our appearance model differs in the choice of classifier and in the way the training samples are extracted, where we use random samples extracted from easily obtainable low quality airway tree segmentations instead of hand picked training points as described in [77].

Secondly, we propose to incorporate a segmented vessel tree to further improve the performance of the voxel classification based appearance model. The fact that airways are accompanied by arteries is well known, and has previously been used in both airway and vessel segmentation [13, 83, 97]. Vessels are especially useful for airway segmentation in CT because of its better visibility, as shown in [97]. In our work, we extend this idea to using the orientations between vessels and airways, similar to [13] who used it for artery-vein separation. This exploits the fact that every airway branch is accompanied by an artery, and that both structures have similar orientation, which to our knowledge has not been applied to the segmentation of airway trees. The final segmentation is obtained with a 3D region growing algorithm based on a decision function that combines both the airway appearance model and the relationship between airways and arteries.

Early versions of this work were presented in [60] and [58]. This chapter offers an extended evaluation and introduces a multi-scale approach to vessel orientation similarity. This chapter is organized

as follows: We start by explaining the training of the airway appearance model in Section 4.2. Section 4.3 presents the various steps involved in computing the vessel orientation similarity measure. The segmentation framework that combines both the airway appearance model and the vessel orientation similarity is presented in Section 5.4. Section 5.5 presents the results of a set of experiments on 250 low dose CT images. Discussion of the results from our experiments, comparison with other related works, and suggestions for possible improvements are presented in Section 5.6. Finally a conclusion is presented in Section 4.7.

4.2 Classification based airway appearance model

We propose an airway appearance model that is based on voxel classification. A potential drawback of such a classification-based appearance model is that it requires segmented training data, which may be difficult to obtain. In this work, an easily obtainable manual segmentation was used for training instead, which is incomplete but leakage free. The construction of this manual segmentation as well as steps taken to compensate for its incompleteness during the training process are explained in the following. This is followed by a description of the extraction of training samples, which focus on the smaller airways. Finally the choice of the classifier and its training process are presented.

4.2.1 Incomplete manual segmentation as a basis for training

Ideally, a gold standard obtained from hand-tracing by one or multiple human experts should be used for the training of a classification-based appearance model. However, such a gold standard is in general not available for airway trees, due to the extreme amount of manual labor involved. Fortunately, incomplete but leakage free airway tree segmentation can easily be obtained interactively, which we will show is sufficient to train our appearance model.

An intensity based region growing algorithm was used to obtain the manual segmentations needed, where a seed point within the trachea as well as an intensity threshold were determined manually. The highest threshold possible without causing any leakage was selected for each of the training images individually. This typically results in an over conservative segmentation that has many missing branches. However, the 'background' region directly surrounding such a conservative segmentation will always contain airway voxels. To exclude likely airway voxels trained as background, a second 'leaked segmentation' was obtained using a threshold slightly higher than the one used for the manual segmentation, which results in more and often longer airway branches, but also with some leakage. The voxels that were marked in the leaked segmentation denote uncertain regions that may be either airway or background, and were excluded from the training process. Figure 4.1 shows an example of the manual and leaked segmentation.

Training was performed using two classes: the airway class and the non-airway class. The airway class consists of all voxels that were labeled in the manual segmentations, excluding the trachea, left and right main bronchi. The non-airway class was limited to voxels within the lung fields and close to the airways. The lung fields were extracted using the lung segmentation algorithm described in Chapter 2, with the smoothing and holes filling process. The region within the lung fields that is close to the airways were obtained by dilating the manual segmentation with a sphere of radius R_{dilate}. The non-airway class then consists of all voxels within this dilated region not marked by the leaked segmentation.

Only a fraction f_s of the voxels belonging to the airway class was used as training samples, excluding the trachea and the left and right bronchi. This results in a total of $N_s = f_s V$ training samples, where V is the total number of airway class voxels in the manual segmentation with trachea, and both left and right main bronchi excluded. The same number of training samples were also extracted from the non-airway class. In order to prevent the large number of voxels in the larger airways from dominating the appearance model, we sample evenly along the distance from the main bronchi. The distance from a voxel to the main bronchi is defined as the shortest distance measured within the segmented tree, which was obtained by applying the fast marching algorithm [63, 102] on the manual segmentation with the main bronchi as seeds.

The sampling process was performed by first grouping the voxels based on their distance from

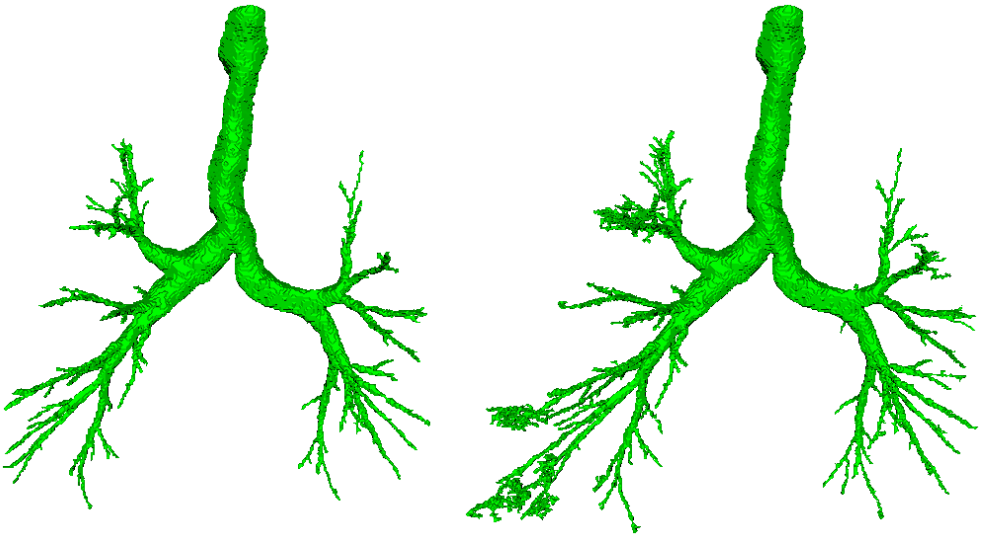

(a) Manual segmentation (b) Leaked segmentation

Figure 4.1: Surface renderings of the interactively obtained segmentations used for training.

the main bronchi in bins of width W, and then randomly sampling a total of $N_b = N_s W/D_{max}$ training samples from each bin, where D_{max} is the maximum distance between a voxel in the manual segmentation to the main bronchi. In order to prevent a bin from being sampled too densely, only a fraction f_b ($\gg f_s$) of all voxels belonging to the bin were used as samples for extraction. Finally, samples were extracted by starting from the bin furthest away from the main bronchi. If the required number of samples from a bin was larger than the number of samples available in the bin itself, the remaining samples were extracted from the next available bin of shorter distance.

4.2.2 Airway probability

The training samples of Section 4.2.1 were used to train a classifier to differentiate between voxels belonging to the airway and non-airway class. Any classifier that outputs a posterior probability or other soft classification can be used here, but in this work we choose the k nearest neighbors (KNN) classifier [16, 20]. An initial feature set of local image descriptors was computed from the training samples, which consisted of spatial derivatives up to and including the second order, eigenvalues of the Hessian matrix (λ_1, λ_2 and λ_3, where $|\lambda_1| \geq |\lambda_2| \geq |\lambda_3|$), determinant and trace of the Hessian matrix, Frobenius norm of the Hessian matrix, and combinations of Hessian eigenvalues that measure tube, plate and blobness ($|\lambda_2/\lambda_1|$, $|\lambda_3/\lambda_1|$, $(|\lambda_1| - |\lambda_2|)/(|\lambda_1| + |\lambda_2|)$, $|\lambda_3|/\sqrt{|\lambda_1\lambda_2|}$). The partial derivatives of the image were computed at multiple scales by convolving the image with the partial derivatives of the Gaussian kernel [116], and the features were standardized to zero mean and unit variance.

Sequential floating forward feature selection [86] was used to find an optimal set of image descriptors that maximizes the area under the receiver operating characteristic (ROC) curve of the classifier. To this end, the training samples were randomly partitioned into two parts to compute the ROC curve: one third for training of the classifier and two thirds for validation. We constructed the final KNN classifier using the optimal combination of features and all training samples.

With the constructed KNN classifier, for each voxel we can now estimate the posterior probability of it belonging to the airway class, given a set of optimal features $\vec{x}$, using:

$$p(A|\vec{x}) = \frac{K_A(\vec{x})}{K} \tag{4.1}$$

where A is the airway class, $K_A(\vec{x})$ is the number of neighbors around $\vec{x}$ belonging to the airway class, obtained among the K nearest neighbors.

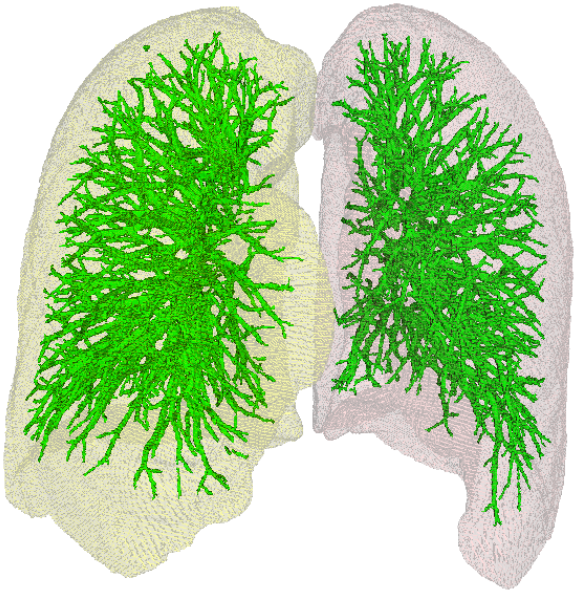

Figure 4.2: An example of a segmented vessel tree.

4.3 Obtaining vessel orientation similarity

The vessels were first segmented from the lung fields using a multi-scale Hessian eigen analysis approach. The scale for calculating the Hessian matrix was selected for each voxel independently using the scale normalized [57] Frobenius norm of the Hessian matrix:

$$\omega(\sigma_i) = \sigma_i^2 \sqrt{\lambda_1(\sigma_i)^2 + \lambda_2(\sigma_i)^2 + \lambda_3(\sigma_i)^2}$$

where the local vessel scale, σ_v, was then obtained by selecting the smallest scale that corresponds to a local maximum of ω across scales. Using the Hessian eigenvalues at scale σ_v, the following criteria were used to evaluate whether a voxel was part of a vessel or not:

- $\lambda_1, \lambda_2 < 0$ (Brightness)
- $\omega \geq T_\omega$ (Contrast)
- $(|\lambda_1| - |\lambda_2|)/(|\lambda_1| + |\lambda_2|) < T_1$ (Tubeness 1)
- $(|\lambda_1| - |\lambda_3|)/(|\lambda_1| + |\lambda_3|) > T_2$ (Tubeness 2)

where a voxel was labeled as vessel when all four criteria were satisfied. The brightness criterion ensures that only voxels that were brighter than their surroundings were selected, the contrast criterion reduces the effect of noise by ensuring a certain minimum contrast between the voxel and its surroundings, and finally the two tubeness criteria require vessels to locally resemble bright, solid cylinders. Within a solid bright tubular structure, λ_1 and λ_2 correspond to the principal curvatures along the directions perpendicular to the tube axis, and λ_3 corresponds to the tube axis. Hence, the eigenvalues within a tubular structure have a relationship of $|\lambda_1| \approx |\lambda_2| \gg |\lambda_3|$, resulting in a value near zero for the tubeness 1 criterion and a value near one for the tubeness 2 criterion.

Segmentation using the vessel criteria often results in additional small, isolated regions due to noise. A connected component analysis using a 6-connected neighborhood scheme was employed in order to remove these small isolated regions, where components with volumes less than V_{min} voxels were discarded. Figure 4.2 shows an example of the vessel segmentation. Finally, the vessel centerlines were obtained using the 3D thinning algorithm presented in [114].

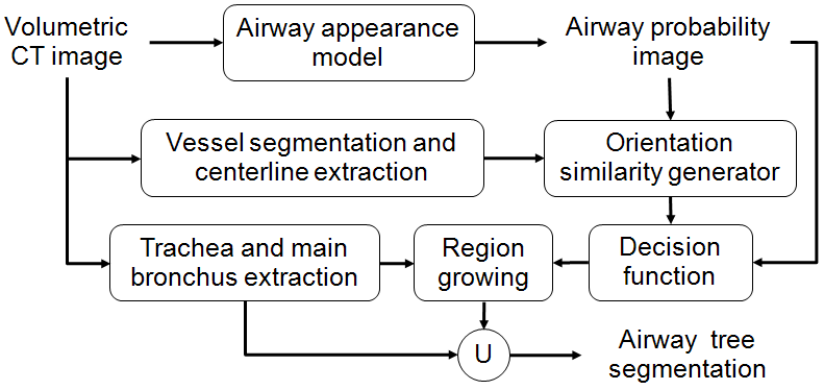

Figure 4.3: Block diagram of the segmentation framework

The vessel orientation at the centerline voxels was obtained as the eigenvector corresponding to λ_3 computed at the vessel scale σ_v. This measure is less sensitive to noise and inaccuracies in the vessel segmentation than the orientation obtained directly from the centerline itself. The orientations of the airways were also extracted the same way as the orientations of the vessels, but in contrast to vessels, we calculated the multi-scale Hessian matrix on the airway probability (5.1), where airways appears as solid, bright tube structures.

Given θ as the angle between the local tube orientation at an airway candidate voxel and the orientation measured at the centerline of a vessel nearest to it, we use $s = |cos(\theta)|$ as vessel orientation similarity measure. When the two orientations are similar, then $s \simeq 1$, and when the orientations are perpendicular, then $s \simeq 0$.

4.4 Segmentation framework

We obtain the airway tree segmentation using a 3D region growing algorithm, with a connectivity of 6-connected neighbors and a decision function that combines both the airway appearance model of Section 4.2 and the vessel orientation similarity of Section 4.3. The trachea, left and right main bronchi were automatically segmented and used as seeds for the region growing algorithm. Figure 4.3 shows a block diagram of the proposed segmentation framework.

4.4.1 Preprocessing

A set of seed points within the trachea was first obtained automatically by searching for a dark elliptical object in the top few slices of a volumetric CT image. This set of seed points was then used to extract the trachea and the main bronchi using a fast marching based algorithm that detects bifurcations. This algorithm is based on the work by [90], where we use only the bifurcation detection of the original algorithm for preprocessing (refer to Section 4.8 for details). The algorithm was made to process voxels with intensity value below -900 HU, which was chosen slightly higher than the intensity of air in order to cope with noise and possible artifacts within the trachea. To only extract up to the left and right main bronchi, the algorithm was made to stop after extraction of all first generation branches.

4.4.2 Airway segmentations

The trachea and the left and right main bronchi obtained in Section 5.4.1 were used as seed points in a region growing process to extract the remainder of the airway tree, using the airway probability and vessel orientation similarity measures. Here, the vessel orientation similarity was used as a means to lower the threshold on airway probability in regions with low airway probability according to the appearance model, but with local tube orientation that is similar to the orientation of nearby vessels. Three thresholds were introduced for this purpose: upper probability threshold T_u, lower probability

threshold T_l, and vessel orientation similarity threshold T_s. All voxels with an airway probability larger than or equal to T_u were accepted automatically. For voxels with airway probability between T_u and T_l, the decision was made based on the vessel orientation similarity and T_s. The decision function for the acceptance of a candidate voxel is defined as

$$D(p(A|\vec{x}), s) = \begin{cases} 1, & p(A|\vec{x}) \geq T_u \\ 1, & T_u > p(A|\vec{x}) \geq T_l \text{ and } s \geq T_s \\ 0, & \text{otherwise,} \end{cases} \tag{4.2}$$

where $p(A|\vec{x})$ is the airway probability computed from (5.1), and s is the vessel orientation similarity of the candidate voxel. The voxel is labeled as an airway when $D(p(A|\vec{x}), s) = 1$.

4.5 Experiments and results

Experiments were conducted on 250 low-dose CT images (120 kV, 40 mAs) from 250 different subjects enrolled in the Danish Lung Cancer Screening Trial (DLCST) [80], where participants were current or former smokers at an age between 50-70 years. All images had a slice thickness of 1 mm and in-plane voxel size ranging from 0.72 to 0.78 mm. Three different datasets were used:

Dataset 1: Images from 32 randomly selected subjects. For these images, the leakage free manual segmentations and the leaked segmentations, as described Section 4.2.1, were made for training purpose;

Dataset 2: Images from 18 subjects with moderate to severe emphysema (an average of 24.25% of the lung volume has intensity below -950 HU). For these images, obvious leakage already occurred using intensity based region growing at the minimum threshold of -1000 HU;

Dataset 3: Images from 200 randomly selected subjects.

The performance of appearance model based region growing was evaluated with and without vessel orientation similarity and was compared to that of region growing based on intensity alone for all 3 datasets.

The objective of the experiment on dataset 1 is to study the feasibility of the proposed voxel classification approach, which is trained using a manual segmentation that was incomplete but leakage free. Dataset 2 investigates the ability of the proposed method to avoid leakages that are unavoidable using intensity alone. The experiment conducted on the dataset 3 shows the general performance of the proposed method on a large set of images.

4.5.1 Parameter settings

KNN classification was performed using the ANN library for approximate nearest neighbor searching [2]. A neighborhood of $K = 21$ was used, and the approximation error *eps* was set to zero to turn off the approximation part of the algorithm. For the extraction of training samples, as described in Section 4.2.1, a dilation radius $R_{dilate} = 5$ mm was used in order to include both the airway walls and some surrounding lung tissues of the small airways. The fraction of voxels sampled was set to $f_s = 0.05$, the bin width for the sample extraction process was set to $W = 3$, and the fraction of voxels used as samples for extraction in each bin was $f_b = 0.5$. A total of 7 scales, distributed exponentially between 0.5 mm and 3.5 mm were used to compute the features. The same scales were also used to segment the vessels in Section 4.3. A contrast threshold $T_\omega = 100$, and tubeness measure thresholds $T_1 = T_2 = 0.5$ gave acceptable vessel segmentation results for our application. $V_{min} = 20$ voxels was used to filter off the small isolated regions in the segmented vessel tree.

Suitable settings for the probability thresholds T_u and T_l, and the vessel orientation similarity threshold T_s were selected automatically using the leakage detection algorithm as described in Section 4.8. This algorithm, derived from [90] and [106], is used to compute the tree length (TL) and percentage of leakage voxels (LVP). We define TL as the total length of all correct branches excluding the trachea. LVP is defined as the percentage of leakage voxels among all labeled voxels, with the

Table 4.1: Average results from two-fold cross validation experiment with dataset 1.

	TPR (%)	FDR (%)	BC	TL (mm)	LVP (%)
Intensity	90.41	7.43	101.12	1347	6.19
Airway probability	98.40	21.62	150.44	1939	2.40
Airway probability + Vessel orientation similarity	98.68	24.94	161.44	2084	2.95

trachea and the left and right main bronchi excluded. The probability thresholds T_u and T_l were varied over 21 different values (with 0 excluded), which was equivalent to the number of neighbors K used for the KNN classifier. The vessel orientation similarity threshold T_s was varied over 21 different values ranging from 0 to 1. A total of 4011 different combinations of thresholds were tested. The threshold combination selected was the one where further increase in the LVP will not give any significant increase in the TL, with a maximum allowed LVP of 5%.Only images from the training set were involved in selecting the threshold settings. The airway probability for each image was obtained from a KNN classifier constructed in a leave-one-out manner.

4.5.2 Comparison to manual segmentation

A two-fold cross validation experiment was conducted on the 32 images of dataset 1, where the subjects were randomly separated into two groups of 16 images each. The first group was used as training set for selecting the features, constructing the KNN classifier and determining the thresholds that were to be applied to the second group and vice-versa. Because of the lack of a ground truth, true positive and false positive rate based analysis is insufficient to evaluate the results of the experiments. We therefore also detect leakage using the modified Schlathölter algorithm, as described in Section 4.8, for evaluation purpose. We report the TL and LVP as described in Section 4.5.1, as well as the branch count (BC), which is the number of correct branches excluding the trachea. As the modified Schlathölter algorithm is prone to being too sensitive and ended up rejecting true airway branches, detected leakage that overlapped with the manual segmentation was added back into the segmentation to reduce the number of true airway branches rejected.

We compare three different segmentation approaches: region growing on intensity, region growing on airway probability, and the proposed approach of using both airway probability and vessel orientation similarity. The threshold for region growing using intensity was determined based on the training set using the optimal threshold selection procedure described in Section 4.5.1, from a range of intensities between -1000 HU and -900 HU. The threshold for using airway probability alone was obtained by selecting the best performing threshold settings when $T_u = T_l$ and $T_s = 0$.

Table 4.1 shows the average results from the cross validation experiments, given as true positive rate (TPR = TP/(TP+FN)), false discovery rate (FDR = FP/(FP+TP)), BC, TL, and LVP, where TP, FP and FN are true positives, false positives and false negatives respectively. The airway probability based methods have significantly higher TPR than the intensity based region growing. The combination of airway probability and vessel orientation similarity results in significantly longer TL ($p < 0.01$) than using only airway probability, with no significant increase in LVP ($p = 0.33$). The average LVP is the highest for the experiment with intensity based region growing, which is in part caused by 2 cases of severe leakage with LVP $> 97\%$. Figure 4.4 and Figure 4.5 shows the surface renderings and slice view of 3 cases of segmented airways using the different methods, with two common cases and one case where intensity regions growing results in severe leakage.

4.5.3 Effects of parameter settings

To investigate the impact of the parameters related to the airway appearance model, the cross validation experiment in Section 4.5.2 was repeated with varying parameter settings. Three main parameters were considered, which were the number of nearest neighbors K, dilation radius R_{dilate} and sampling

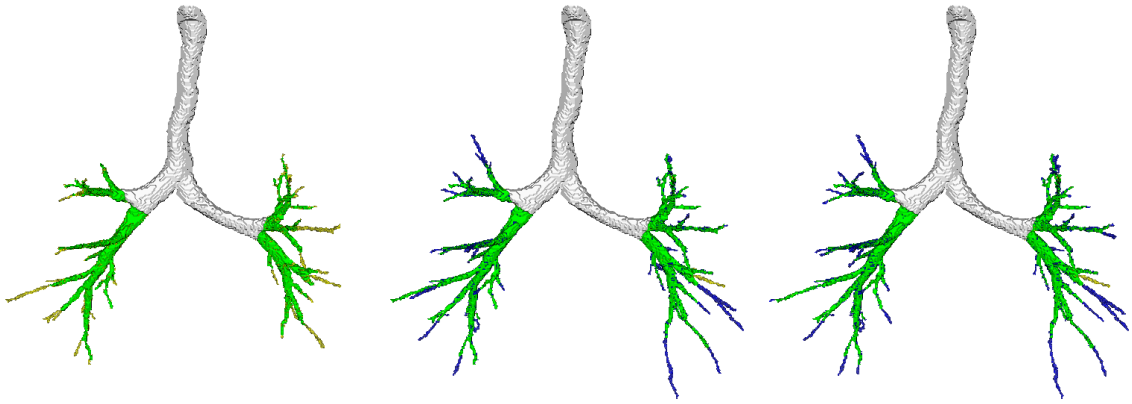

(a) TL: 764 mm, 1414 mm, 1497 mm

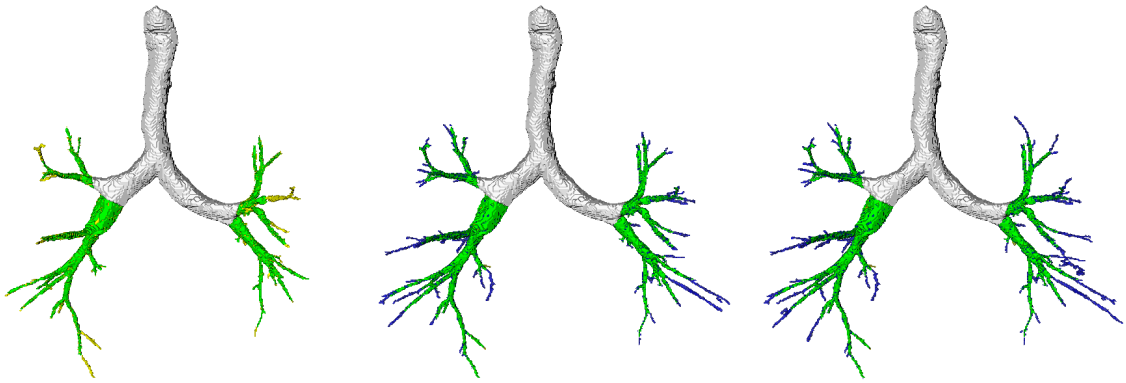

(b) TL: 1008 mm, 1750 mm, 2030 mm

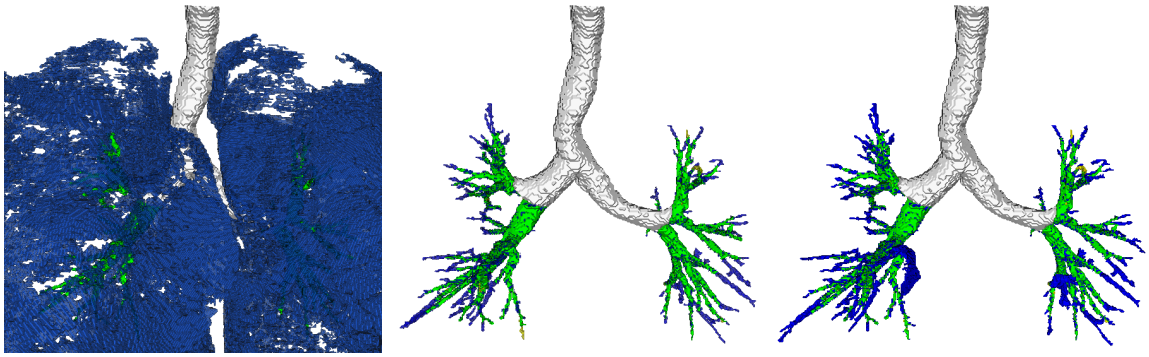

(c) TL: 1953 mm, 2084 mm, 2304 mm

Figure 4.4: Surface renderings of results of 3 different subjects from the two-fold cross validation experiment, along with the TL from the different results. From left to right: surface renderings of segmentation results using intensity, using airway probability, using both airway probability and vessel orientation similarity. Pre-segmented trachea, left and right main bronchi are shown in white, TP, FP and FN are shown in green, blue and yellow respectively.

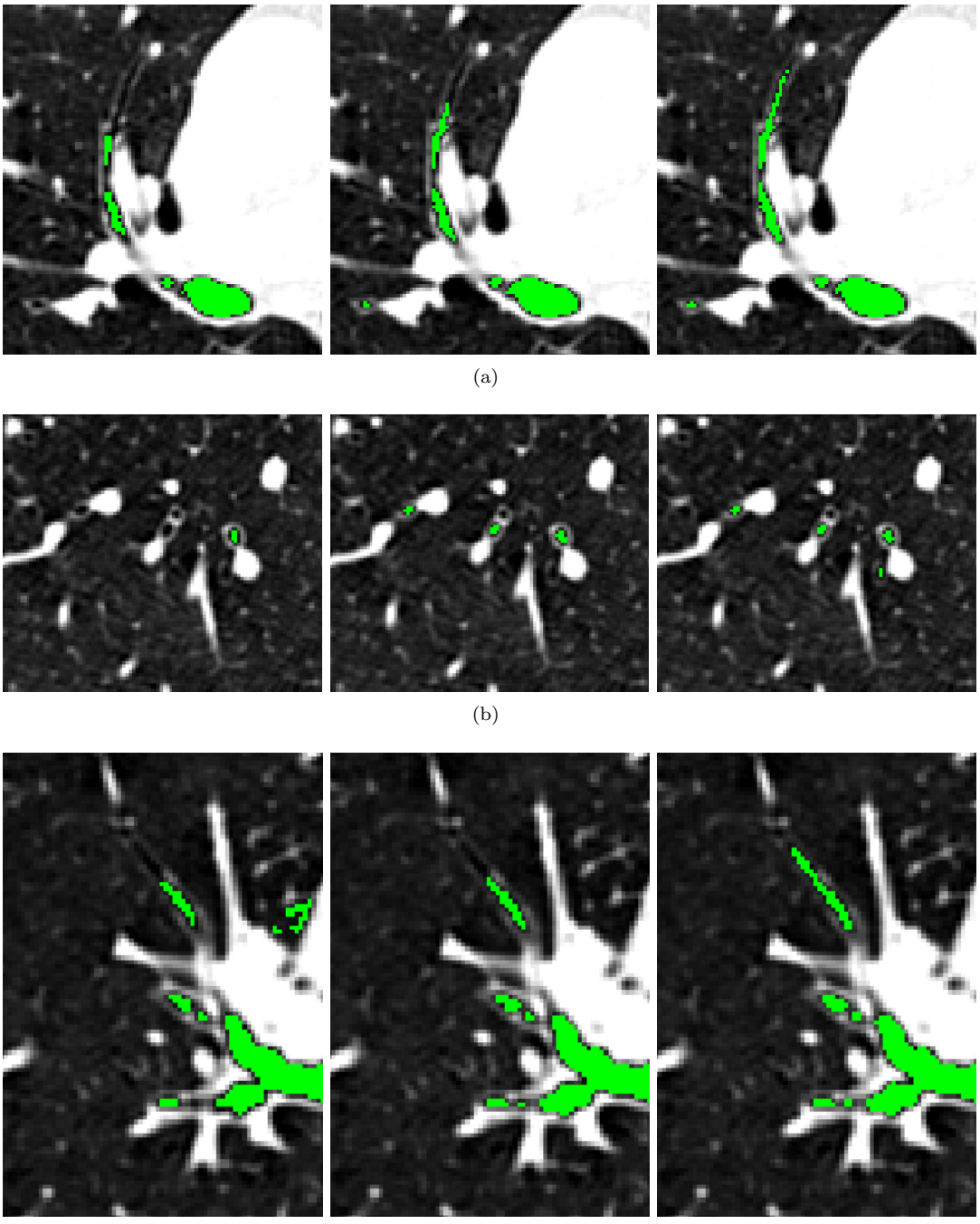

Figure 4.5: Axial view images of 3 different subjects from the two-fold cross validation experiment. From left to right: segmentation results using intensity, using airway probability, and using both airway probability and vessel orientation similarity.

Table 4.2: Results from a series of experiments conducted using different parameter settings for the construction of the appearance model. Changed parameters are indicated in bold.

K	R_{dilate}	W	TPR (%)	FDR (%)	TL (mm)	LVP (%)
21	5	3	98.40	21.62	1939	2.40
11	5	3	97.78	20.52	1911	1.60
31	5	3	98.48	21.47	1906	2.08
21	**2.5**	3	98.58	18.89	1851	4.92
21	**10**	3	98.58	24.13	1938	2.59
21	5	**10**	98.31	19.13	1852	1.95
21	5	**20**	98.63	25.84	1966	7.35

Table 4.3: Average results from 18 cases in dataset 2, with severe leakage for intensity based region growing at -1000 HU.

	TL (mm)	BC	LVP (min - max) (%)	LVP > 10%
Intensity	2057	151.33	76.76 (5.22 - 98.94)	16
Airway probability	2377	174.28	12.77 (0.35 - 89.65)	4
Airway probability + Vessel orientation similarity	2590	193.17	28.79 (0.47 - 97.20)	6

bin width W. These parameters were varied from their original values in Section 4.5.1 one at a time. To simplify comparison and isolate the effects of the appearance model, the thresholds were chosen equal to those used in Section 4.5.2 for the region growing based on the appearance model and without vessel orientation similarity, thus with $T_u = T_l$ and $T_s = 0$. Table 4.2 shows the average results of the different parameter settings.

4.5.4 Leakage avoidance and performance on large dataset

The 32 images of dataset 1 were used to train the classifier and to select the thresholds for processing datasets 2 and 3. As there were no manual segmentations available for the test data, we report the BC, TL and LVP as computed directly using the modified Schlathölter algorithm. Unfortunately, this also means that there will be more overestimation in the LVP as compared to the Section 4.5.2 and 4.5.3, due to the lack of manual segmentation.

Table 4.3 shows the average results for dataset 2, which contains images from 18 subject with different degree of emphysema, where leakage occurs at -1000 HU. The minimum and maximum LVP, and the number of cases with LVP exceeding 10% are also presented to give a better indication of the amount of leakage occurring in the different methods. Figure 4.6 shows an example of the results obtained by the different methods.

All three methods were applied to the 200 screening images in dataset 3, with the average TL, BC and LVP shown in Table 4.4. We also visually inspected the surface renderings of all results from the proposed method that combines both airway appearance model and vessel orientation similarity. Obvious leakage were observed in only eight cases, all of which were correctly identified by the leakage detection algorithm. We also observed some obvious falsely detected leakages in five cases, where a whole subtree of true airway branches was classified as leakage by the modified Schlathölter algorithm. Figure 4.7 shows results of 4 different subjects from this dataset from the proposed method.

4.6 Discussion

We investigate whether:

Table 4.4: Average results from 200 cases in dataset 3.

	TL (mm)	BC	LVP (%)
Intensity	1401	99.26	13.29
Airway probability	2012	146.39	2.23
Airway probability + Vessel orientation similarity	2115	154.11	4.54

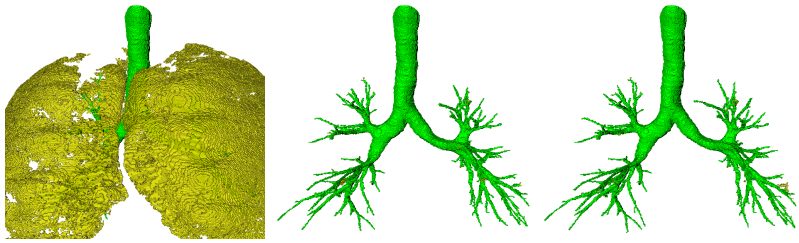

Figure 4.6: Surface renderings of results from a subject with emphysema. From left to right: surface renderings of segmentation results using intensity, using airway probability, and using both airway probability and vessel orientation similarity. Leakages are marked in yellow.

1. Local image descriptors can improve upon intensity based airway segmentation;
2. A trained appearance model is feasible;
3. Inclusion of co-orientation between vessels and airways can improve results.

A simple 3D region growing framework is used with no further geometrical constraints. Airway probability estimates based on local image descriptors as well as vessel orientation similarity are incorporated in this framework and the performance gain compared to intensity region growing is measured.

Table 4.1 shows that the methods that use the classifier based appearance model perform better in terms of true positive rate and tree length than intensity based region growing. The voxel classification based methods resulted in higher false discovery rate compared to intensity based method, but it must be noted that a slightly higher false discovery rate may actually be desirable in our case, as new branches found that are not in the manual segmentation are labeled as false positives as well. Upon visual inspection, the majority of 'false positives' from the appearance based methods in our

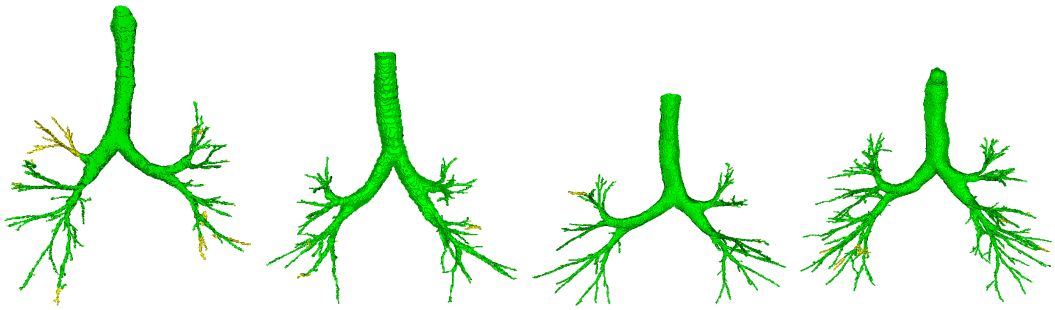

Figure 4.7: Surface renderings of results from 4 different subjects from the large dataset obtained using appearance model and vessel orientation similarity measure. The yellow regions are regions classified as leakages by the modified Schlathölter algorithm.

experiments turned out to be valid airways that were missing in the manual segmentation. An example of this is shown in Figure 4.5. This is further verified by the modified Schlathölter algorithm, where we observe a large difference between false discovery rate and percentage of leakage voxels in Table 4.1, with over 20% in false discovery rate compared to less than 5% in percentage of leakage voxels. This suggests that the majority of the false positives in the voxel classification based methods are actually real airways. For the intensity based region growing method, the false discovery rate (7.43%) is only slightly higher than percentage of leakage voxels (6.20%).

Results from our experiments on the three dataset in Table 4.1, Table 4.3 and Table 4.4 all showed a similar trend, with the proposed method having the highest tree length and branch count, followed by region growing with airway probability, and with region growing with intensity having the lowest tree length and branch count. The appearance model based region growing methods are also less prone to leakage, and is capable of avoiding leakages that are unavoidable by region growing with intensity. This is shown in Table 4.3, where the appearance model based methods clearly have less percentage of leakage voxels and also less cases with severe leakage (LVP $> 10\%$), as compared to region growing with intensity.

4.6.1 Sensitivity to parameter settings

As mentioned earlier in Section 4.5.3, the threshold for the airway probability used for each fold of the experiment were fixed to those used in Section 4.5.2 to simplify comparison and isolate the effects of the appearance model. Therefore, the threshold settings used may not be optimal for the parameter settings used in Table 4.2. Nonetheless, the overall true positive rate and tree length as observed in Table 4.2 are still quite high, with a minimum of 97.78% and 1851 mm repectively. Although the percentage of leakage voxels varies quite a bit, with a maximum of 7.35%. It should be noted that all, except for a single case, have percentage of leakage voxels of less than 5%, which to our experience is well within acceptable range. The high tree length and low percentage of leakage voxel over most of the tested parameter settings suggests that the appearance model performs quite well for a wide range of parameters.

Varying the number of nearest neighbors K in the appearance model has very little effect on the performance, resulting in a slight decrease in tree length of no more than 30 mm, and with percentage of leakage voxels remaining well below 3%. Performance degrades when the dilation radius R_{dilate} for extracting non-airway samples becomes too small. Since the over conservative, region growing based segmentation used for training underestimates the lumen, a small value of R_{dilate} results in a large number of actual airway lumen samples being labeled as 'non-airway' in the training. On the other hand, if the R_{dilate} becomes too large, then non-airway samples will be taken from voxels far away from the airway walls, which are less relevant for discriminating between airway lumen and background. A suitable value of R_{dilate} ensures that samples are taken from the airway walls as well as the nearby background. A sharp increase in percentage of leakage voxels is observed when taking a large bin width W in extracting samples along the tree. The reason is that samples from the large airway branches start to dominate the appearance model, causing the appearance model to be less sensitive to the smaller scale features that are required to avoid leakages in the smaller airway branches.

The modified Schlathölter algorithm described in Section 4.8 contains a large number of parameters and rules, which to our experience are not robust and depended heavily on the quality of the images and conditions of the subjects, e.g. ultra-low dose or scans of patients showing airway pathology. For this particular reason, we only use the modified Schlathölter algorithm for selecting suitable values for T_u, T_l and T_s, which in practice can also be done manually. It should be noted that the proposed method only uses simple region growing for generating the segmentation results. We also use the modified Schlathölter algorithm to estimate the amount of leakage in segmentation results for evaluation purpose, due to the lack of ground truth.

4.6.2 Effects of vessel orientation similarity measure

The airway probability image from the appearance model provides a good indication of the location of the airways in the image, but it is noisy, with many single voxels or small areas within the airways having relatively low airway probability. In a region growing process this can lead to entire subtrees

being discarded due to one broken connection caused by a small cluster of low probability voxels. This happens especially in the thin, peripheral airway branches, where one or two low probability voxels are sufficient to block the entire descending subtree. A simple post processing of the airway probability image is not sufficient to remove these problems; we have experimented with coherence enhancing anisotropic diffusion [115] to remove the low probability areas, but did not observe a significant improvement. Incorporating vessel orientation similarity as an additional criterion in the region growing helps to overcome these areas, which is supported by the improvements shown in Table 4.1.

A single scale version of the proposed method was reported in our previous paper [58]. In comparison, the current, multi-scale approach enables reliable computation of the orientation of airways and vessels of various sizes rather than targeting only the small airways and vessels, which results in an overall improvement in the amount of branches segmented.

A potential weakness of the proposed vessel orientation similarity measure is that it is not well defined near airway or vessel bifurcations. We therefore rely more on the airway probability and accept all voxels where the airway probability is high, and only use the weaker vessel orientation similarity as a second opinion when the airway probability is low. This is implemented using the upper probability threshold T_u, which makes the decision independent of the vessel orientation similarity when the airway probability is high.

4.6.3 Comparison to results in literature

It is difficult to compare our results to the results obtained by other authors as most airway tree segmentation methods were evaluated by visual inspection only. One of the exceptions is the work by [100], where the number of extracted branches were counted. However, the segmentation results were restricted to the sixth generation and only the number of 'named branches' extracted were counted, which makes a direct comparison with our results impossible. Another exception is the recent work by [106], in which the average tree length, the number of branches extracted, and the branch length at different generations were reported for several different datasets including a set of 50 low dose images from the NELSON study [108]. Our results on the large dataset in Section 4.5.4 are similar to the results reported in [106], who reported a tree length of 2184 mm and an average branch count of 166, as compared to 2127 mm and 155 from our proposed method. A slightly smaller tree length would be expected in our case since our population contains more women (52% compared to 17% for the NELSON study), who typically have smaller lungs and shorter airway branches than men. The scans from DLCST are also of lower resolution as compared to the NELSON study, where the slice thickness is 1 mm for the DLCST study and 0.7 mm for the NELSON study. The method presented in this chapter, using a smart airway appearance model with a single, global threshold setting with a simple 3D region growing algorithm, is complementary to the method in [106]. Combining the two approaches may result in even better results.

4.6.4 Possible improvements

One might expect that a trained appearance model, such as is used here, cannot perform much better than the segmentations that were used to train it, which in our case were obtained using a simple intensity based region growing. However, the airway generation and the number of subtrees that can be extracted in such a simple region growing method differ from image to image and from lobe to lobe. Therefore, even though the airway tree segmentations used for training are incomplete individually, it is still possible to obtain sufficient examples of voxels that cover an entire airway tree by using a collection of these incomplete airway trees.

Since decisions are made for each voxel independently, small holes do occur in the segmentation, especially in the larger airways. These holes could, for instance, be removed by applying a morphological closing operator on the segmentation results. Alternatively, more accurate segmentations of the inner and outer airway walls could be sought around the centerlines extracted in this paper using, for instance, graph cut segmentation, as was presented in [81]. In the current paper, we aimed to extract the airway trees as complete as possible and were less concerned with the accuracy of the extracted airway lumen. We therefore did not perform such post processing in this work.

Despite the good results, the current setup still misses many small peripheral airways branches. The reason for this is that examples of such small airways are not available in the training segmentations obtained by the interactive intensity based region growing algorithm. A way to approach this problem would be to create a better training set, for instance using manual or interactive segmentation, such as in [101], or by first segmenting high quality, high resolution, clinical dose data, using the intensity region growing method described in Section 4.2.1, and then train the classifier on lower quality simulated low dose images.

Due to the threshold relaxation introduced by the vessel orientation similarity, the proposed method is more prone to leakage as compared to using airway probability alone, with slightly more number of cases with severe leakage (LVP $> 10\%$) and percentage of leakage voxels, as shown in Table 4.3 and Table 4.4. This is mainly caused by emphysematous areas around the hilum that locally resemble airway lumen. Leakage into these areas can cause leakage to the lung surface, which usually has high response in the airway appearance model. Figure 4.4c (right-most image) shows an example of such case. A way to reduce the severity of this effect would be to prevent the border of the lungs from being evaluated, for instance by restricting the evaluation on regions marked by an eroded lung segmentation.

Our current implementation assumes that the detected vessel nearest to an airway candidate voxel is the accompanying artery. It may be useful to discard airway candidates that are too far away from the detected vessels, in order to further improve segmentation results, similar to [97]. In addition, an artery-vein separation algorithm [13] could be applied to process only those points that are at a certain distance from the extracted arteries. However, the majority of the false positives we observed in our experiments are caused by high responses from the appearance model at the hilum as mentioned above. Therefore the extent of improvements introduced by adding this extra step may be minimal.

Another approach to improve results would be to use a more flexible decision function, e.g. a second stage classifier that takes into account the airway probability, vessel orientation similarity, distance from nearest vessel and etc. One drawback of a second stage classifier is the increase in computation time. However, a more serious problem would be the continuous usage of the incomplete manual segmentations for training, which may result in a classifier that produces over conservative segmentations. It should be noted that our proposed method performs very well, despite using a relatively simple threshold based approach, as very few branches in the training data are missed, especially when taking into account the number of extra branches found.

Despite of the good results, it is a fact that the proposed method requires a relatively long computation time. On average, the total time needed to segment the airway tree from a single CT scan using the proposed method was 55 minutes on a single CPU of an Intel Xeon X5355 processor (2.66 GHz). The majority of the time is spent on voxel classification to generate the airway probability image (ca. 25 minutes), and on computing the seven Gaussian blurred images for the original image and the airway probability image (ca. 20 minutes). The final segmentation process however is relatively fast, with a total execution time of around 10 minutes. However, it should be noted that not only most of the processes are independent from each other, the operations within are also highly independent. This makes the proposed approach highly parallelizable, and therefore a large performance gain can be expected from the usage of parallel processing technologies such as multi-core processors and graphics processing unit.

4.7 Conclusion

An airway tree segmentation method that is based on a trained airway appearance model is presented. It is shown that good results can be obtained even with imperfect training data, with segmentation results that are better than the training data itself. We combine the airway appearance model with a measure of orientation similarity between airways and vessels, which results in an additional significant improvement in segmentation performance with an increase in detected airway tree length and little or no increase in leakage.

4.8 Appendix: Automated detection of leaks and extraction of branch length

The algorithm for leakage detection and branch length extraction is based on the algorithms presented in [90] and [106]. Their observation was that a wave front propagating through a tree structure remains connected until it encounters a bifurcation, and any side branches can thus be detected as new disconnected components in the propagating front. We use the fast marching algorithm [63, 102] to propagate the wave front, similar to what was proposed in [90], with the front monitored through the set of "trial" points. For our purpose of evaluating a segmentation, we use a speed function that gives a value of 1 within the segmented structure and a value of 0 outside. This limits the propagation to only the segmented region.

Besides being able to detect bifurcations, the algorithm is also able to extract centerlines of individual branches and detect leakages. The centerline of a branch is constructed from the centroids of the propagation front at each time stamp. This also makes it possible to obtain the length of each individual branch by measuring the length of its centerline. Leakages were detected through a series of rules based on the geometric properties of the front, as described in [90] and [106]. Similar to [106], we divided the leakage detection rules into two levels: a segment level and a tree level.

The segment level rules were applied when a branch was still being segmented by the fast marching algorithm, and the radius and connectivity of the propagation front were being monitored. At this level, three criteria were used for leakage detection:

$$D_{seg}(S) = \begin{cases} 1, & r_c/r_{prev} > 3 \\ 1, & r_c/min(R_{max}) > 1.5 \\ 1, & n_f > 5 \\ 0, & \text{otherwise,} \end{cases} \tag{4.3}$$

where r_c is the radius of the current front, r_{prev} is the average radius of the previous 5 fronts, R_{max} is a set containing the maximum radius obtained at each of the ancestor branch segments and n_f is the number of disconnected fronts detected. The current segment, S, was discarded if $D_{seg}(S) = 1$. Furthermore, a sub segment was automatically accepted once its length exceeds 5 mm in order to prevent rejection of long segments due to small faults at the end.

The tree level rules were applied after all branch segments have been extracted. The criteria were defined as:

$$D_{tree}(S) = \begin{cases} 1, & n_b > 3 \\ 1, & \theta_{parent} > 100^\circ \\ 0, & \text{otherwise,} \end{cases} \tag{4.4}$$

where n_b is the number of children and θ_{parent} is the angle between a segment and its parent. Segment S along with its children were removed when $D_{tree}(S) = 1$. All connected non-bifurcating segments, due to their children being rejected at some point in the process, were then merged into a single segment. Finally, all end segments with lengths less than 1 mm were considered as noise and were subsequently removed.

It should be noted that the values of the various parameters values were similar to those suggested in [90] and [106], and were selected on the basis of pilot experiments on a number of images in dataset 1.

Chapter 5

Classification Based Airway Segmentation on Diverse CT Scans

This chapter is based on the manuscript "Multiscale Vessel-guided Airway Tree Segmentation", by P. Lo, J. Sporring and M. de Bruijne, in Proceeding of Second International Workshop on Pulmonary Image Analysis, pp. 323-332, 2009.

Abstract This chapter presents a method for airway tree segmentation that uses a combination of a trained airway appearance model, vessel and airway orientation information, and region growing. The method uses a voxel classification based appearance model, which involves the use of a classifier that is trained to differentiate between airway and non-airway voxels. Vessel and airway orientation information are used in the form of a vessel orientation similarity measure, which indicates how similar the orientation of the an airway candidate is to the orientation of the neighboring vessel. The method is evaluated within EXACT'09 on a diverse set of CT scans. Results show a favorable combination of a relatively large portion of the tree detected correctly with very few false positives.

5.1 Introduction

Most existing airway segmentation methods are based on region growing, with the assumption that the airway lumen has low intensity and is surrounded by higher intensity airway walls. The main problem with such an intensity based region growing algorithm is that the contrast between the airways and their surroundings is sometimes very low, due to noise or pathologies such as emphysema. Such low contrast regions often cause the region growing algorithm to leak into the surrounding lung tissue. Currently there are two approaches to address this problem: explosion control and the use of more advance image descriptors than intensity alone.

The idea of explosion control is to stop the segmentation in the low contrast regions where otherwise leakage would occur, while the segmentation continues in other regions. Strategies for explosion control generally involve heuristic rules based on geometrical properties of the regions labeled. Some examples of these geometrical properties are: volume of the regions segmented [44], radius of propagation front [90, 106], cross section area [47] and topology of thinned structure [100].

The second approach makes use of local image information to better differentiate between airways and their surroundings, for instance using pattern recognition techniques [58, 60, 77] or local tube fitting [30]. The method presented here belongs to this second approach.

This chapter presents an extension of Chapter 4, where the proposed method is applied and evaluated within the EXACT'09 [59] airway extraction challenge on a database of 20 scans taken at different sites under a variety of different conditions. The results were manually evaluated by trained observers and compared to results submitted by other participants.

This chapter is organized as follows: Section 5.2 gives a brief description on the construction of the airway appearance model using the training set. Section 5.3 presents a short description of the various steps involved in computing the vessel orientation similarity measure. The segmentation framework that combines both the airway appearance model and the vessel orientation similarity is presented in Section 5.4. Section 5.5 presents the results of the 20 cases in the EXACT'09 testing set. Finally, a discussion of the results and comparison with results submitted by other teams are presented in Section 5.6.

5.2 Airway appearance model

The steps for constructing the appearance model is the same as described in Section 4.2. The manual and leaked segmentation are obtained for all the training cases, using a interactive intensity based region growing algorithm. An example of a manual and a leaked segmentation are shown in Figure 5.1(a) and (b).

Before the extraction of training samples, we extract the lung fields with the smoothing and holes filling process, as described in Chapter 2. Training samples from two classes are then extracted using both segmentations from the training data: the airway class and the non-airway class. The airway class consists of all voxels that are labeled in the manual segmentation, excluding the trachea and main bronchi. Areas belonging to the non-airway class are those that are within the lung fields that are close to the airways, defined by dilating the manual airway segmentation with a sphere of radius R_{dilate}, and are not marked by the leaked segmentation.

Only a small percentage S_{sample} of the voxels belonging to the airway class are used for training, and the same number of training samples is also extracted from the non-airway class. Sampling of airway class is made such that samples are extracted evenly along the airways, where voxels are first grouped into bins based on their distance from the main bronchi, with the width of each bin fixed to W. In addition, each bin is made such that they only contains 50% (selected randomly) of all the voxels belong to it. A total of $N = S_{sample}VW/D_{max}$ training samples are then sampled randomly from each bin, where V is the total number of airway class voxels in the manual segmentation and D_{max} is the maximum distance between a voxel in the manual segmentation to the main bronchi. If the required number of samples from a bin is larger than the number of voxels available in the bin, the remaining samples are extracted from the next available bin of shorter distance.

Gaussian derivatives and Hessian eigen analysis based local image descriptors are computed for each of the samples, which are then used as input features to a k nearest neighbors (KNN) classifier [20]. In order to identify an optimal set of features that gives the best performance for the KNN classifier, sequential forward feature selection [86] is used, where we sought to maximize the area under the receiver operating characteristic (ROC) curve of the classifier. Given a voxel with a set of optimal features $\vec{x}$, the posterior probability of this voxel belonging to the airway class can then be estimated using the following:

$$p(A|\vec{x}) = \frac{K_A(\vec{x})}{K} \tag{5.1}$$

where A is the airway class, $K_A(\vec{x})$ is the number of neighbors around $\vec{x}$ that belong to the airway class, obtained among the K nearest neighbors.

5.3 Vessel orientation similarity

The same steps for obtaining the vessel orientation similarity described in Section 4.3 is used here. The vessels are segmented from the lung fields, using a multi-scale Hessian eigen analysis approach, which uses the scale normalized [57] Frobenius norm of the Hessian matrix as selection criterion:

$$\omega(\sigma_i) = \sigma_i^2 \sqrt{\lambda_1(\sigma_i)^2 + \lambda_2(\sigma_i)^2 + \lambda_3(\sigma_i)^2}$$

The local vessel scale, σ_v, is then obtained by selecting the smallest scale that corresponds to a local maximum of $\omega(\sigma_i)$ across scales. Using the Hessian eigenvalues at scale σ_v, the following criteria are used to evaluate whether a voxel belongs to a vessel or not:

Brightness:	$\lambda_1, \lambda_2 < 0$
Contrast:	$\omega \geq T_\omega$
Tubeness 1:	$(\|\lambda_1\| - \|\lambda_2\|)/(\|\lambda_1\| + \|\lambda_2\|) < T_1$
Tubeness 2:	$(\|\lambda_1\| - \|\lambda_3\|)/(\|\lambda_1\| + \|\lambda_3\|) > T_2$

A voxel is labeled as vessel when it fulfills all four criteria. After obtaining the vessels, a connected component analysis using a 6-connected neighborhood scheme is employed to remove regions that are smaller than V_{min} voxels. Finally, the vessel centerlines are obtained using the 3D thinning algorithm presented in [114].

The vessel orientation at the centerline voxels is obtained as the eigenvector corresponding to λ_3 computed at the vessel scale σ_v. The orientation of an airway is extracted the same way as the orientation of a vessel, through multi-scale Hessian eigen analysis, except that the Hessian matrix is constructed using the airway probability image generated using (5.1). Given θ as the angle between the local tube orientation at an airway candidate voxel and the orientation measured at the centerline of a vessel nearest to it, the vessel orientation similarity is defined as $s = |cos(\theta)|$. When the two orientations are similar then $s \simeq 1$, and when the orientations are perpendicular then $s \simeq 0$.

5.4 Segmentation framework

The airway tree segmentation is obtained using a 3D region growing algorithm, with a decision function that combines both the airway appearance model of Section 4.2 and the vessel orientation similarity of Section 4.3. An initial airway segmentation described in Section 5.4.1 is used as seeds for the region growing algorithm. Figure 5.1(f) shows a block diagram of the proposed segmentation framework.

5.4.1 Initialization

The segmentation process is initialized with a coarse segmentation of the first four airway generations obtained using intensity based region growing. First, starting from the trachea and main bronchi as obtained in Section 4.2.1, all connecting voxels with intensity lower than a threshold T_{airway} are added. This is followed by a closing operation with a sphere mask of 3 voxels in radius. Finally, an algorithm [90] that is capable of tracking generations via bifurcation detection is applied to the smoothed segmentation, and only branches up to the fourth generation are retained. The threshold T_{airway} is dynamically determined by searching from -1000HU, with an increment of 5 HU, until the resulting initial segmentation, excluding trachea and main bronchi, is larger than 1000 voxels.

5.4.2 Airway segmentation

The initial segmentation obtained previously is used as seed points in a region growing process to extract the remainder of the airway tree, using the airway probability and vessel orientation similarity measures. The vessel similarity is used as a means to relax the requirements on airway probability in regions with a local tube orientation that is similar to the orientation of nearby vessels. We achieve this by using the following decision function to decide on whether to accept an airway candidate voxel $\vec{x}$ or not

$$D(p(A|\vec{x}), s) = \begin{cases} 1, & p(A|\vec{x}) \geq T_u \\ 1, & T_u > p(A|\vec{x}) \geq T_l \text{ and } s \geq T_s \\ 0, & \text{otherwise,} \end{cases} \tag{5.2}$$

where $p(A|\vec{x})$ is the airway probability computed from (5.1), s is the vessel orientation similarity of the candidate voxel, T_u, T_l and T_s are the upper probability threshold, lower probability threshold, and vessel similarity threshold respectively. The voxel $\vec{x}$ is labeled as an airway when $D(p(A|\vec{x}), s) = 1$.

5.4.3 Parameter settings

KNN classification was performed using the ANN library for approximate nearest neighbor searching [2]. A $K = 21$ was used, and the approximation error *eps* was set to zero to turn off the approximation part of the algorithm. For the extraction of training samples, as described in Section 4.2.1,

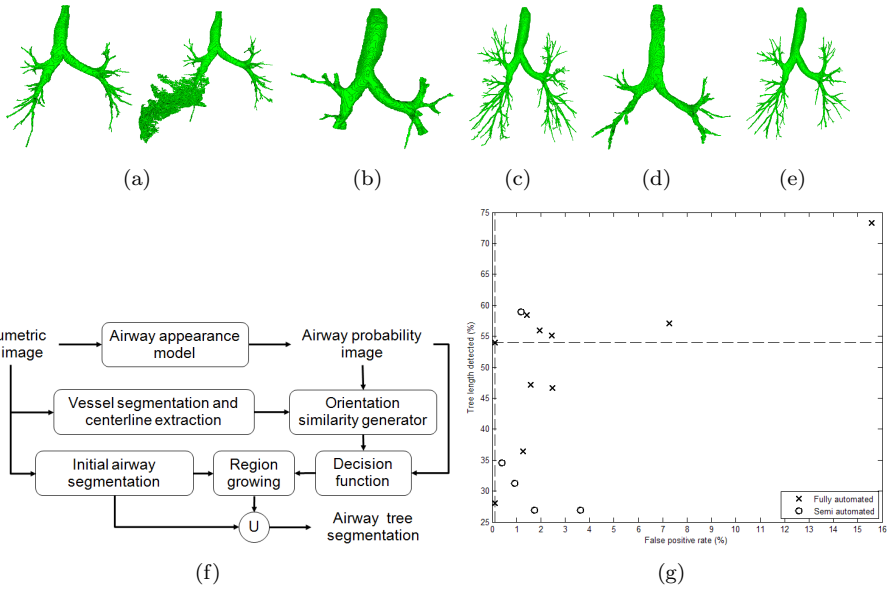

Figure 5.1: Surface renderings of (a) a manual (left) and leaked (right) segmentation used for training, (b) initial segmentation, test results with (c) largest (CASE40) and (d) smallest (CASE37) percentage of tree detected. (e) Surface renderings of segmentation from CASE40 obtained using screening study scans from [58] as training. (f) Block diagram of the segmentation framework. (g) A scatter plot of average tree length detected versus average false positive rate of all participating teams in EXACT'09, with the proposed method at the intersection of the dashed lines.

the dilation radius R_{dilate} was set to 5 mm, sampling percentage S_{sample} was set to 0.05, and the bin width W was set to 3 voxels. A total of 7 scales, distributed exponentially between 0.5 mm and 3.5 mm, were used to compute the features, as well as for the multi-scale Hessian eigen analsysis in Section 4.3. A contrast threshold T_ω of 100, and tubeness measure thresholds T_1 and T_2 of 0.5 were used for the vessel criteria. Detected vessel regions smaller than $V_{min} = 20$ voxels were discarded. All these parameter values are the same as those reported in Section 4.5.1.

The thresholds for the decision function (5.2) was hand tuned based on the training set, where the airway probability images were generated with KNN classifiers that were constructed in a leave-one-out manner. Our experiments with the training set showed that $T_u = 0.86$, $T_l = 0.62$ and $T_s = 0.8$ gives good results, where a significant amount of new branches not in the training data were found without any significant leakages.

5.5 Experiments and results

Among the 20 cases (CASE01-CASE20) in the training set from EXACT'09, manual segmentations for training were successfully obtained from all cases except one (CASE06), where leakage was observed even when using the lowest possible threshold. Therefore only 19 cases from the training set were used to train the KNN based appearance model.

The training process of our method took approximately 13 hours on a single CPU of an Intel Xeon X5355 processor (2.66 GHz), with the feature selection process occupying around 11 hours. The average computation time to segment an image in the test case was approximately 1 hour and 30 minutes. Most of the computation time was spent generating the airway probability image, which took an average of 50 minutes. The remaining computation time was mainly spent on generating the Gaussian blurred images and performing the multi-scale Hessian eigen analysis.

Table 6.3 shows the evaluation results of our method on the 20 EXACT'09 test images. Surface renderings of the best case and worst case according to the detected tree length are shown in Figure 5.1(c) and (d).

Table 5.1: Evaluation measures for the twenty cases in the test set.

	Branch count	Branch detected (%)	Tree length (cm)	Tree length detected (%)	Leakage count	Leakage volume (mm^3)	False positive rate (%)
CASE21	114	57.3	64.2	58.1	0	0.0	0.00
CASE22	276	71.3	227.1	68.7	1	0.2	<0.01
CASE23	186	65.5	137.9	53.0	1	15.4	0.12
CASE24	128	68.8	106.0	65.1	0	0.0	0.00
CASE25	152	65.0	116.9	46.4	0	0.0	0.00
CASE26	48	60.0	32.9	50.0	0	0.0	0.00
CASE27	49	48.5	36.9	45.6	0	0.0	0.00
CASE28	77	62.6	57.3	52.2	0	0.0	0.00
CASE29	117	63.6	81.3	58.9	1	10.0	0.12
CASE30	140	71.8	109.5	71.7	3	26.2	0.32
CASE31	159	74.3	117.8	67.1	3	39.1	0.31
CASE32	151	64.8	120.9	55.5	2	7.3	0.05
CASE33	108	64.3	81.3	55.2	0	0.0	0.00
CASE34	301	65.7	213.1	59.6	3	14.0	0.07
CASE35	136	39.5	95.2	30.8	0	0.0	0.00
CASE36	187	51.4	185.2	44.9	0	0.0	0.00
CASE37	57	30.8	46.4	26.1	0	0.0	0.00
CASE38	36	36.7	27.8	41.8	0	0.0	0.00
CASE39	253	48.7	195.1	47.7	6	37.0	0.30
CASE40	333	85.6	315.5	81.5	17	214.8	0.90
Mean	150.4	59.8	118.4	54.0	1.9	18.2	0.11
Std. dev.	85.2	13.6	75.4	13.4	3.9	48.0	0.22
Min	36	30.8	27.8	26.1	0	0.0	0.00
1st quartile	77	48.7	57.3	45.6	0	0.0	0.00
Median	138	63.9	107.7	54.1	0	0.0	0.00
3rd quartile	253	71.3	195.1	67.1	3	26.2	0.30
Max	333	85.6	315.5	81.5	17	214.8	0.90

5.6 Discussions and conclusion

At the expense of a relatively long computation time and laborious training procedure, we obtain a favorable combination of a relatively large portion of the tree detected correctly with very few false positives. Table 6.3 shows that the proposed method is able to extract at least 50% of the total tree length for 70% of the cases, with a false positive rate of less than 1% for all cases. Although many branches were either extracted only partly or missed completely, it should be noted that no method was able to extract more than, on average, 77% of tree length or branches in the ground truth. Among the 15 methods that were compared in EXACT'09, 7 methods resulted in both a lower tree length and a higher false positive rate. Compared to the remaining 7 methods, our results stand out mainly by the small amount of leakage; in 11 cases there were no false positives at all, and in the remaining cases both leakage volume and false positive rate were small. Figure 5.1(c) shows few clear leakages even in the case with the largest number of detected leaks (CASE40). Our method is also the only method with an average false positive rate below 1% (0.11%) that is still able to achieve an average detected tree length of higher than 50% (54%), as shown in Figure 5.1(g). Among all methods with an average false positive rate below 5%, the method achieving the highest tree length, which is a semi-automated method, detected only 5% more of the total tree length at a false positive rate of 1.19%.

The presented method was originally developed for segmenting the airway tree in more standardized, low-dose cancer screening scans obtained at a single site [58, 80]. While the main approach and parameter settings used for the current work are the same as in [58], the implementation differs

from this previous work in three ways. Firstly, the Hessian eigen analysis to determine vessel and airway orientations, performed at a single resolution level in [58], was replaced by a multi-resolution analysis. This modification had already been developed for the screening study and improved results considerably for that data.

To cope with the much more diverse data of EXACT'09, the method was further modified in two ways from our experiments on the training images. The first modification is that a more complete segmentation is used to initialize the classification-based region growing, instead of using only the trachea and main bronchi as reported in [58]. The reason for this is because we found that otherwise the segmentation was sometimes already terminated within the first four generations in noisy images. The second modification is that the thresholds for the decision function in this work were manually tuned based on the training data, while those in our earlier work were tuned automatically using an automatic leakage detection algorithm similar to [90] and [106]. In the diverse and sometimes very noisy CT scans from EXACT'09, this rule-based, automatic leakage detection algorithm turned out to be unreliable. The criterion used in selecting the thresholds was that no obvious leakage should be present in the results on the training set, which is probably one of the reasons why our results are on the conservative side compared to other methods. A different set of thresholds may lead to longer tree lengths at the expense of an increase in false positives.

In the EXACT'09 study, a training set was provided with carefully selected images that were of similar quality as the images in the test set. If the training data does not match the test data, results may deteriorate. To illustrate this, segmentation of CASE40, obtained using a Siemens Sensation 16 scanner and very sharp convolution kernel B70s, was repeated with the same setup and same parameter settings but using the training data of [58], which consisted only of scans obtained using a Philips Mx8000 IDT 16 scanner with softer kernel D, resulting in less noisy images. The result is shown in Figure 5.1(e). The method trained with different data has still little or no leakage, but finds fewer branches. In this case, this was mainly because the appearance model is not capable of handling the noise and often misclassifies bright noise voxels in the airway lumen as non-airway. Although the method should be trained on similar data for optimal results, the good results on the diverse set of EXACT'09 data indicate that application of this method is not limited to studies in which acquisition conditions can be standardized.

Note that, although the proposed method requires training data, in this work only very low quality segmentations were available for this purpose. The segmentations used for training consisted of on average 93 branches and had a total length of 99 cm. Application of the trained models on the test set of similar images resulted already in much more complete segmentations, with 150 branches and a total length of 118 cm. Clearly, our method can achieve better results than the training segmentations, but the lack of training examples from small branches does limit the ability of the system to extract higher generation airways. With the availability of a set of high quality segmentations for training, such as the ground truth resulting from EXACT'09, we expect to obtain even better results in the future.

In conclusion, an airway segmentation method that uses a voxel classification based appearance model and the similarity between the orientation of an airway and its neighboring vessel is presented. Compared to the results from other algorithms submitted to EXACT'09, our method is especially effective in avoiding leakage, while still being able to extract a fair amount of airway branches.

Chapter 6

Extraction of Airways from CT (EXACT'09): An Evaluation Study

This chapter is an extension of the manuscript "Extraction of Airways in CT (EXACT'09)", by P. Lo, B. van Ginneken, J. M. Reinhardt and M. de Bruijne, in Proceeding of Second International Workshop on Pulmonary Image Analysis, pp. 175-189, 2009.

Abstract This paper describes a framework for establishing a reference airway tree segmentation, which is used to quantitatively evaluate different airway tree extraction algorithms in a standardized manner. Because of the sheer difficulty involved in constructing a complete reference standard manually from scratch, we propose to construct the reference using results from all algorithms that are to be evaluated instead. Each of the segmented airway trees is subdivided into its individual branch segments, where each branch is visually inspected by trained observers to determine whether or not it is correctly segmented. Finally, reference airway trees are constructed by taking the union of all correctly extracted branches. Using the so constructed reference, a total of three performance measures covering the different aspects of segmentation quality are computed. A total of 15 airway tree extraction algorithms from different research groups are evaluated on a diverse set of 20 chest computed tomography (CT) scans, from subjects ranging from healthy volunteers to patients with severe pathologies, scanned at different sites using different CT scanner models and scanning protocols. Results from the evaluation showed that no algorithm is capable of extracting more than an average of 74% of the total length of all branches in the reference standard, indicating a large difference in branches obtained by the different methods.

6.1 Introduction

Segmentation of the airway tree in chest volumetric computed tomography (CT) scans plays an important role in the analysis of lung diseases. An application of airway tree segmentation algorithm is in measuring dimensions of airway lumen and wall, which have been shown to correlate well with Chronic Obstructive Pulmonary Disease (COPD) [9, 75]. As the lungs are subdivided anatomically based on the airway tree, airway tree segmentation is also needed for other segmentation tasks such as segmentation of the lobes [104, 122] and the pulmonary segments [72]. Despite the amount of algorithms proposed, evaluation of the results in most works is limited to only qualitative measurements based on visual inspections. Although quantitative measures are reported in some works [100, 106], such as the number and the total length of branches extracted, the differences in datasets used and in the way the measurements are obtained make it difficult to compare the different works.

The aim of this paper is to develop a framework to establish a reference airway tree segmentation that can be used to evaluate different airway tree extraction algorithms in a standardized manner. We believe that such standardized comparison of different algorithms is critical for future development, as the weaknesses of current algorithms can be identified and improved upon. Because of the sheer difficulty of establishing a complete reference standard manually from scratch, we propose to use the results from the algorithms that are to be evaluated to construct the reference. Segmented airway trees are subdivided into their individual branches. These individual branches are then inspected visually by trained observers and correctly segmented branches are retained, while wrongly segmented branches are rejected. Since the individual branches are from segmented airway trees obtained using different algorithms from the same set of images, branches are bound to overlap. Therefore, the branch inspection process can be accelerated by automatically accepting branches that have high overlap with previously accepted branches. Finally, the reference standard is established by taking the union of all accepted branches.

A total of 40 scans from eight different institutions, obtained under various acquisition conditions and from subjects with different pathologies, are used in this study,. The first 20 scans are designated as training set, to be used for algorithm training and/or parameter tuning purpose. The remaining 20 scans are used as test set, and is used to evaluated the performance of the participating algorithms.

The evaluation is designed to only take into consideration the depth of the airway trees segmented by an algorithm. We do not take the exact airway shape and dimensions into account; a branch is said to be correct as long as there is no significant leakage outside the airway walls. It should be noted that the term "segmentation" is used loosely in this chapter, and can range from actual segmentation of the airway tree lumen to extraction of the centerlines of the airway tree.

The comparative study was organized as a challenge at the 2nd International Workshop on Pulmonary Image Analysis[1], which was held in conjunction with the 12th International Conference on Medical Image Computing and Computer Assisted Intervention (MICCAI 2009). Invitations were sent out to several mailing lists and to authors of published papers on airway tree segmentation. A total of 22 teams registered to download the data, and out of these, 15 teams [6, 7, 11, 21, 22, 24, 38, 52, 61, 68, 82, 101, 111, 119, 120] submitted their results in the end. Ten teams [6, 7, 22, 24, 38, 52, 61, 111, 119, 120] submitted to the fully automated category and five teams [11, 21, 68, 82, 101] submitted to the semi-automated category. All results submitted by participating teams were used to establish the reference standard.

The results from the evaluation of the 15 participating teams are the same as the ones reported in [59] and on the EXACT'09 website[2]. However instead of having seven measures, as reported previously, we only report the three most important measures in this article that best represents the sensitivity and specificity of the different algorithms. In addition, we also investigate the effects of fusing/combining results from the participating algorithms.

6.2 Data

A total of 75 chest CT scans were contributed by eight different sites. The scans were acquired from several different CT scanner models, using a variety of scanning protocols and reconstruction parameters. The conditions of the scanned subjects varied widely, ranging from healthy volunteers to patients showing severe pathologies in the airways or lung parenchyma. A total of 40 scans were selected from the contributed scans to be used as the dataset for the study, which were further divided into a training set and a testing set. Care was taken to ensure that scans from all eight sites were represented in both the training and testing sets and that the files were all anonymized properly. We also ensured that no scans of the same subject were in both the training and testing sets, and that the same number of scans of similar quality obtained at the same site and acquired using similar protocol were included in both sets. The 20 images in the training set were named CASE01 to CASE20, and the 20 images in the testing set were named CASE21 to CASE40. Table 6.1 presents the acquisition parameters, and visual scoring of noise level as well as anomalies from a radiologist of the 20 test cases.

[1] See http://www.lungworkshop.org/2009/
[2] See http://image.diku.dk/exact/

Table 6.1: Acquisition parameters for the 20 test cases. Thickness (T) is given in mm. Exposure is presented in mAs. The breathing status (BS) indicates whether the scan is acquired at full inspiration (I) or full expiration (E). Contrast (C) indicates whether intravenous contrast was used during acquisition ("Y" for yes and "N" for no). Perceived reconstruction (R) indicates whether the scan was reconstructed using soft (S), middle (M) or hard (H) kernel based on visual inspection. The noise level (N) of the scan is scored via visual inspection as high (H), middle (M) or low (L). * indicates that the scan is from the same subject as the previous scan. A continuation of the table is given in Table 6.2.

	T	Scanner	Kernel	Exposure
CASE21	0.6	Siemens Sensation 64	B50f	100
CASE22*	0.6	Siemens Sensation 64	B50f	100
CASE23	0.75	Siemens Sensation 64	B50f	100
CASE24	1	Toshiba Aquilion	FC12	5
CASE25*	1	Toshiba Aquilion	FC10	75
CASE26	1	Toshiba Aquilion	FC12	5
CASE27*	1	Toshiba Aquilion	FC10	75
CASE28	1.25	Siemens Volume Zoom	B30f	120
CASE29*	1.25	Siemens Volume Zoom	B50f	120
CASE30	1	Philips Mx8000 IDT 16	D	40
CASE31	1	Philips Mx8000 IDT 16	D	40
CASE32	1	Philips Mx8000 IDT 16	D	40
CASE33	1	Siemens Sensation 16	B60f	42
CASE34	1	Siemens Sensation 16	B60f	200
CASE35	0.625	GE LightSpeed 16	Standard	N/A
CASE36	1	Philips Brilliance 16P	C	130
CASE37	1	Philips Brilliance 16P	B	30
CASE38*	1	Philips Brilliance 16P	C	20
CASE39	1	Siemens Sensation 16	B70f	205
CASE40	1	Siemens Sensation 16	B70s	105

6.3 Airway branch scoring

This section describes how the individual airway branch segments are scored. We start by describing how an airway tree segmentation is subdivided into its individual branch segments. This is followed by a description how slices from different views for an airway branch segment are extracted for visual assessment. The different labels used for scoring are then described. Finally, we describe how certain branch segments that overlap with previously scored branches are accepted automatically to reduce the burden of the human observers.

6.3.1 Subdividing an airway tree into branches

The proposed evaluation framework centers around being able to subdivide airway tree into its individual branch segments, which makes it possible to perform evaluation on each branch segment individually. The subdivision of airway tree is achieved by detecting bifurcations with a wave front propagation algorithm, as described in [90]. The key idea is that a wave front, propagating through a tree structure, remains connected until it encounters a bifurcation, and any side branches can thus be detected as disconnected components in the wave front.

The front is propagated using the fast marching algorithm [63, 102], with a speed function that results in 1 within and 0 outside the segmented structure, effectively limiting the front to only propagate within the segmented structure. The front is monitored through a set of "trial" points in the fast marching process that represents the propagating front. The number of disconnected components is monitored by applying connected component analysis to the trial points each time the time stamp from the fast marching algorithm is increased by $1/\Delta D$, where ΔD is the average distance between

Table 6.2: Continuation of acquisition parameters for the test cases in Table 6.1.

	BS	C	R	N	Anomalies
CASE21	E	N	H	H	None
CASE22*	I	N	H	H	None
CASE23	I	N	H	M	None
CASE24	I	N	M	H	Small lung nodule
CASE25*	I	N	M	M	Small lung nodule
CASE26	I	N	M	H	Intrafissural fluid
CASE27*	I	N	M	M	Lympheadenopathy, bronchial wall thickening, airway collapse, septal thickening, intrafissural fluid
CASE28	I	Y	M	L	None
CASE29*	I	Y	M	L	None
CASE30	I	N	M	M	Diffuse ground glass
CASE31	I	N	M	L	Diffuse emphysema
CASE32	I	N	M	L	Pleural plaques, mucus plug right lower lobe, few nodules
CASE33	I	N	H	H	Mild bronchiectasis, mucus plugging, tree-in-bud pattern/small infiltrates
CASE34	I	N	H	M	Mild bronchiectasis, mucus plugging, tree-in-bud pattern/small infiltrates
CASE35	I	N	M	M	None
CASE36	I	N	S	L	Bronchiectasis, bronchial wall thickening, mucus plugs, infiltrates
CASE37	I	N	M	M	None
CASE38*	E	N	M	H	Air trapping
CASE39	I	Y	H	H	Extensive bronchiectasis, many infiltrates and atelectasis, tree-in-bud, mucus plugging, central airway distortion
CASE40	I	N	H	L	Extensive areas with ground glass

two voxels. The propagation is stopped if multiple disconnected components are detected in the front, whereupon the process is repeated on the individual split fronts to obtain the branches at the next level. The whole subdividing process ends when all marked regions of the tree have been evaluated. During each application of the connected component analysis, the centroid of the front is computed and stored. Centerlines can then be constructed using the stored centroids. Figure 6.1 illustrates the steps involved in the airway tree subdivision algorithm.

6.3.2 Visual assessment

To enable visual inspection of extracted branches, each of the branches is presented to the trained observers using a fixed number of slices through the branch at different positions and orientations. Two different views are used for visual inspection: a reformatted view that is obtained by straightening the centerline of a branch segment, and a reoriented view that is obtained by rotating the branch segment such that its main axis coincides with the x-axis.

A total of eight slices are extracted from the reformatted view. The first four slices are taken perpendicular to the centerline, distributed evenly from the start to the end of the centerline. The other four slices are taken along the centerline, at cut planes that are angled at 0°, 45°, 90° and 135°. A schematic view of the cut planes for the reformatted view is shown in Figure 6.2(b).

For the reoriented view, a total of nine slices are extracted, three from each axis. For the y-axis and z-axis, which are perpendicular to the axis of the branch segment, the cut planes are placed at 15%, 50% and 85% of the width of the branch measured in the respective axis. On the x-axis, the cut

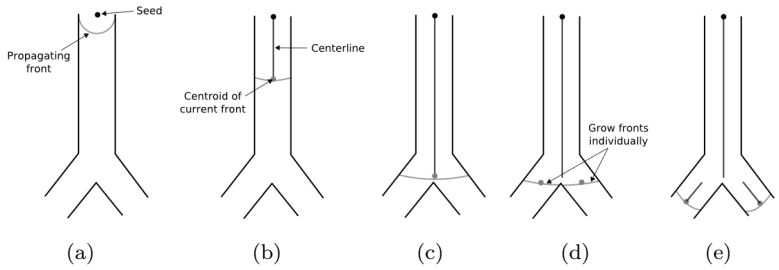

Figure 6.1: Illustration of the process of dividing the airway tree into branches. (a) A seed point is set at the root of a tree and the front propagation process starts. (b) Centroid of the propagating front is stored as centerline at each time step. (c) The centerline is stored up to the point before a bifurcation. (d) Bifurcation is detected as the front splits. The individual fronts are used as seeds to perform front propagation in each of the branches. (e) Front propagation proceeds in each branch.

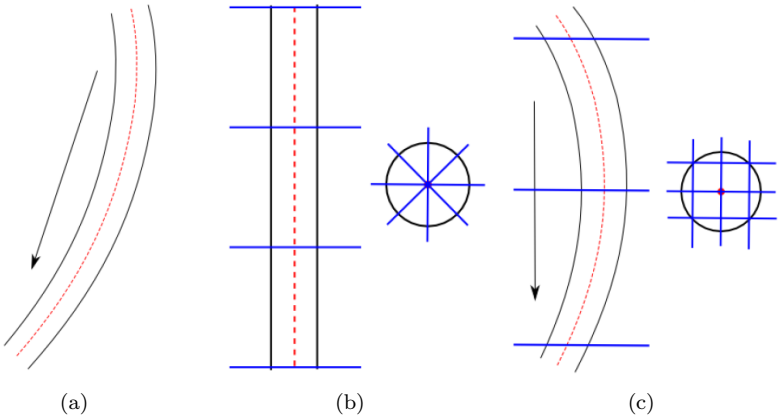

Figure 6.2: Schematics showing the (a) original airway, (b) reformatted view and (c) reoriented view. The arrow is the main orientation of the airway and the cut planes are shown in blue.

planes are placed at 5%, 50% and 95% of the length of the branch. Figure 6.2(c) shows a schematic view of how cut planes are extracted from the reoriented view.

Figure 6.3 shows the slices of the two views extracted from a correctly segmented branch and a segmented branch with leakage.

6.3.3 Scoring of individual branches

Based on the slices from the two views described in Section 6.3.2, trained observers are to assign one of the four following labels to each branch: "correct", "partly wrong", "wrong" or "unknown". A branch is "correct" if it does not have leakage outside the airway wall. "Partly wrong" is assigned to a branch if part of the branch lies well within the airway lumen, while part of it lies outside the airway wall. A branch is "wrong" if it does not contain airway lumen at all. The "unknown" label is used when the observers are unable to determine whether a branch is an airway or not.

The scoring of each branch is performed in two phases. At phase one, two observers are assigned to score a branch. If the same label is assigned by both observers, then the scoring is complete. Otherwise the scoring proceeds to phase two, where three new observers are assigned to re-score the branch. In this phase, the final label assigned to the branch is the label that constitutes the majority vote among the three new observers. In case where there is no majority, the branch is labeled as "unknown". The entire scoring process was automated through a web-based system, where the branches from the submitted segmentation of the test cases were distributed among ten trained observers. The observers were all medical students who were familiar with CT and chest anatomy. They were trained with a

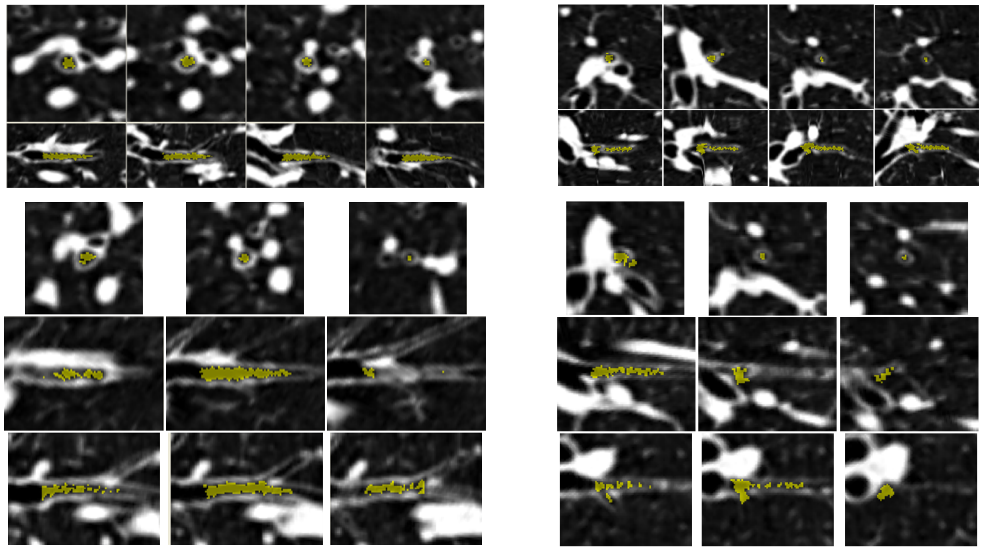

(a) (b)

Figure 6.3: Example of the slices in the views on (a) a correctly extracted branch and (b) a branch with leaks. Top two row are slices perpendicular to the branch segment and slices taken in the direction of the branch segment respectively. In the bottom three row, the first row are axial slices, and the second and third row are cut planes parallel to the branch axis.

set of examples and were assigned to evaluate at least two full airway tree segmentation of different scans, which were used to evaluate the reliability of their scores (see Section 6.6 for details).

6.3.4 Automated branch acceptance

To speed up the scoring process and to reduce the number of branches that observers need to score, branches that are very similar to branches that have previously been labeled as "correct" are accepted automatically.

The following two criteria are used to determine whether to exempt a branch from manual evaluation or not:

1. Centerline overlap: Every point in the centerline is within a 26-neighborhood to a "correct" voxel.
2. Volume overlap: More than 80% of the voxels of the branch are labeled as "correct" in the reference.

Branches that fulfilled both criteria are labeled as "correct" automatically and are exempted from manual evaluation.

6.4 Establishing a reference

The construction of the reference segmentation involves segmentations from all participating teams, and it is done by fusing branches based on the labels assigned during the branch scoring process (as described in Section 6.3).

6.4.1 Updating the reference

The labels assigned to the branches are stored in the form of a reference image. Integer values used to represent the different labels are made such that $L_c > L_w > L_p > L_u > 0$, where L_c, L_w, L_p and L_u are the the values for "correct", "wrong", "partly wrong" and "unknown" respectively.

Initially, a reference image for a given CT scan is an empty image filled with zeros. Scored branches from a new segmentation of the same scan are added to the reference by applying the following update rule on all voxels $\vec{x}$ belonging to the image:

$$G_{t+1}(\vec{x}) = max(G_t(\vec{x}), L(\vec{x})),$$

where G_{t+1} and G_t are the reference image after and before the update respectively, and L is the label assigned by the observers.

6.4.2 Final reference

The final reference of a scan is obtained once it has been updated with the evaluated branches from all participating teams. In this final reference, only voxels that are labelled as "correct" are retained. The remaining voxels are assigned the value zero and are treated as "wrong", except for those labelled as "don't know", which are ignored during the evaluation.

The consequence of only retaining "correct" regions is that correct regions within "partly wrong" regions will be treated as wrong and will be penalized during the evaluation. However, as segmented airway trees from different algorithms of the same scan are used, a vast majority of voxels that are previously labeled as "partly wrong" during the intermediate step will eventually be relabeled, as they overlap with either "correct" or "wrong" regions of branches from other algorithms. Although there are still correct regions within "partly wrong" regions being discarded, they should have minimal impact on the evaluation results, as these regions are small and few in general.

6.5 Evaluation of participating teams

In order to compare the centerlines from the results of the different algorithms in a standardized manner, all centerlines from the different algorithms are projected to those from the reference segmentations (obtained using Section 6.3.1). The detected length of a branch in the reference from a given segmentation can now be obtained by measuring the length of the projected centerline directly.

For a branch in the reference that is longer than $\Delta l = 1$ mm, a segmented airway tree is said to detect the branch only if the detected length for the branch is $>\Delta l$. The reason for this is to prevent long branches from being trivially detected, for instance, where only a single voxel of a branch is being detected.

Three performance measures were computed for each segmented airway tree submitted by the participating teams:

1. Branch detected: The fraction of branches that are detected correctly with respect to the total number of branches present in the reference, N_{ref}, defined as

   $$\frac{N_{seg}}{N_{ref}} \times 100\%$$

   where N_{seg} is the number of branches detected correctly by the segmentation.

2. Tree length detected: The fraction of tree length that is detected correctly relative to the tree length in the reference, L_{ref}, defined as

   $$\frac{L_{seg}}{L_{ref}} \times 100\%$$

   where L_{seg} is the total length of all branches detected by the segmentation.

3. False positive rate: The fraction of the total segmented voxels that is not marked as "correct" in the reference, defined as

   $$\frac{N_w}{N_c + N_w} \times 100\%$$

   where N_c and N_w are the number of voxels in the segmented airway that overlaps with the "correct" and "wrong" regions in the reference respectively. Note that "don't know" regions in the reference are not included in the calculation of the false positive rate.

The trachea is excluded from all the measures. Further, for measure 3, the left and right main bronchi are excluded as well.

6.6 Training and evaluation of human observers

A total of ten human observers took part in the scoring of the branches. Among the ten observers, four observers participated at the early phase of the study, where both the dataset and segmentation results from the participating teams were still not available. Training of these four observers was conducted by the first author, and this consisted of an explanation of the various views and the definition of the labels, and a hands-on experience on the software used for the scoring process. Segmentations of two low dose screening chest CT scans, not used in this study, from pilot experiments of [61] and [111] were used in the hands-on session. During this session, errors made by the observers were pointed out and corrected on the fly. The errors mainly consisted of wrongly assigning "correct" label to branches that are known to be "wrong" or "partly wrong". The whole session lasted approximately one and a half hour. A documentation containing a brief explanation of the different views, four examples of "correct" and "partly wrong", ranging from obvious cases to borderline cases, and three examples of "wrong" cases, was also given to the observers later.

The remaining six observers participated later on, when the dataset and part of the segmentation results from the participating teams were available. The documentation mentioned earlier was provided to the six observers and training sessions were conducted by the first four observers. Hands-on sessions for these observers were conducted on at least two of the available segmentations from the participating teams that were fully evaluated (without automated branch acceptance) by two of the first four experienced observers. Automated branch acceptance was also turned off for the new observers during these training sessions. The number of disagreements between the new observer and one of the experienced observers was compared to the number of disagreements between the experienced observers, where the new observer was said to be *good enough* if the amount of disagreements from the new observer was no more than 10% of the those from the experienced observers. In general, the errors of observers that were not *good enough* were usually due to confusion between "correct" and "partly wrong" labels. For these observers, an extra session was held, where their obvious errors, mainly those similar to the examples in the documentation, were pointed out and the correct labels were shown to them.

6.7 Evaluated algorithms

A total of ten fully automated methods and five semi-automated methods (indicated by *) are evaluated in this study. Fully automated in this context implies that no user interactions were needed during the segmentation process. Semi-automated indicates that user interactions, such as manual selection of seed points or parameters, were needed during the segmentation process.

1) Morphological filtering and operations: A morphology based approach is proposed in Irving et al. [38]. Possible regions belonging to the airway are first marked using morphological filtering and reconstruction. Region growing is then performed on the marked region to obtain the final airway segmentation. Closed space dilation is used to detect leakage during region growing. The method takes an average of 71 minutes to segment an image on a 2.83 GHz personal computer (PC).

2) Morphological aggregative: Fetita et al. [22] reconstructs airway tree based on airway candidates selected using the flood size-drain leveling morphological operator. The reconstruction of the actual airway tree is performed by applying several propagation schemes iteratively that encourages propagation within airways and avoid leakage to lung parenchyma. An extra pre-filtering procedure is also introduced to further improve results, where the filter used was chosen based on the scanner model, reconstruction kernel and dosage. The entire process takes an average of 5 minutes to segment an image.

3) Neighboring affinity and dynamic local cylindrical volume of interest:* Pinho et al. [82] proposed a method that extends the work presented in [100], which obtains airway branch segmentation by applying region growing in iteratively obtained cylindrical volumes of interest. They proposed to use of a simplified skeleton constructed based on the starting point and end points of a branch segment

to improve computation speed, which is also used to estimate the heights, radii and orientations of the cylindrical volumes that are to be added in the next iteration. A neighbor affinity technique, which involves testing whether the intensity of the surroundings of a candidate voxel is lower than a certain threshold, is used as a criterion for the local cylindrical bounded region growing algorithm. The method requires specific tuning of the parameter involving the height of the cylindrical volume of interest for certain cases. Segmentation of an image requires less than 8 seconds for most cases on a 2.4 GHz PC.

4) Tracing via adaptive cuboidal volume with Laplacian of Gaussian: Feuerstein et al. [24] proposed to segment on images enhanced using a sharpening filter that is based on Laplacian of Gaussian. The airway tree is extracted using a tracing scheme that uses cubical volumes constructed from the orientation of detected branches. A region growing process is iterated within each of the cubical volumes until a suitable threshold is found, which is determined by the number of furcating branches. The method takes average of 5 minutes to process an image on a 2.66 GHz PC.

5) Voxel classification and vessel orientation similarity: Lo et al. [61] proposed to perform region growing on the output of a classifier trained to differentiate between airway and non-airway voxels. A vessel similarity measure that compares how similar is the orientation of an airway candidate to neighboring vessel is used to overcome local false positives from the classifier. The whole framework takes approximately 90 minutes to process an image on a 2.66 GHz PC. (See Chapter 5 for details)

6) Morphological gradient:* Fabijanska [21] proposed a two step segmentation approach. The first step consists of obtaining an initial segmentation by performing region growing on an image where the intensities are normalized. The initial segmentation is then used as seeds for a second region growing process that is performed on the morphological gradient of the original image. The method requires manual selection of a threshold related to the second region growing process in some cases. No computation time is provided for this method.

7) Tube detection: Bauer et al. [7] proposed the use of a tube detection filter, where centerlines are extracted using a ridge traversal procedure that is based on hysteresis thresholding. The airway tree can then be reconstructed by iteratively merging unconnected tubular objects to the centerlines of the trachea. Prior knowledge of the airway tree such as branching angle, radius and etc. are utilized during the merging process. Using an implementation that makes use of graphics processing unit (GPU), the method takes an average of 3 minutes to process a single case.

8) Maximal contrast adaptive region growing:* Mendoza et al. [68] proposed a segmentation approach that uses a sequence of region growing processes that maximizes an evolving contrast measure, which involves previously segmented regions. A preprocessing step that involves non-linear normalization using a sigmoidal transfer function and denoising via an in-slice bidimensional median filter is introduced to improve robustness. The method requires user to manually place several seed points in the upper trachea for initialization. Segmentation of a single case requires an average of 2 minutes on a 2 GHz PC.

9) Centricity-based region growing: Wiemker et al. [120] proposed the use of a voxel-wise centricity measure with prioritized region growing. The centricity measure quantifies how central a given voxel is to the surrounding airway walls by measuring the lengths of rays projected from the voxel itself. A ray terminates if the density difference, with respect to the starting point, of a point along the path of the ray is higher than a certain threshold. A region growing process is used to obtain the actual segmentation, where it proceeds until all connected voxels below a certain density threshold and above a certain minimum centricity value are extracted. The runtime of the method for an image is 19 seconds on average on a 3 GHz PC.

10) Dynamic thresholded region growing with local cylindrical volume of interest: Lee et al. [52] proposed a method that is similar to [100], which segments airways within cylindrical volumes of interest that are added iteratively. A acceptance criterion requiring that at least half of the neighbors of a candidate voxel is below a certain threshold is used for the region growing process. Threshold for the region growing process is incremented until leaks occur, which are detected by analyzing segmented regions at the boundary of the volume of interest. Segmentation of an image takes less than 30 seconds on a 3 GHz PC.

11) Template matching:* Born et al. [11] proposed the use of a 2D template matching technique along with a set of fuzzy rules to detect and prevent leakage. Airway tree segmentation is obtained through an iterative procedure that iterates between a 3D region growing, a 2D wave propagation

and a 2D template matching process. Their method requires user to set a seed point in the trachea manually. The method requires around 25 seconds to segment a image on a 2.4 GHz PC.

12) Self adapting region growing with histogram correction: Weinheimer et al. [119] proposed a self adapting region growing that is based on monitoring the volume of the segmented region, where threshold is increased when no leakage is detected. The acceptance criteria for a single voxel, which is used in a region growing framework, is based on fuzzy logic rules that are applied on features from projected rays from the voxel. A normalization procedure based on histogram analysis is introduced as a preprocessing step to correct for miscalibrated scans. An average of 6 minutes is required to segment a case on a 2.83 GHz PC.

13) Gradient vector flow: Bauer(a) et al. [6] proposed a method that is based on an edge preserving gradient vector diffusion function called the gradient vector flow. A tube-likeness measure is computed for every voxel based on the vector obtained from the gradient vector flow. Subsequently, centerlines are extracted by applying hysteresis thresholding on the tube-likeness measure. Voxels near to the extracted centerlines are finally marked by inversely tracking the gradient vector to form a segmented airway tree. The method requires 6 minutes to process an image with a GPU based implementation.

14) Rules based sphere constricted region growing with multi-threshold: van Rikxoort et al. [111] proposed a wavefront propagation approached that is based on sphere constricted region growing, where geometric characteristics of a branch such as furcation and radius are obtained from the propagating front. A series of rules such as radius growth, furcating angles and etc. are used to detect and prevent leaks. The method also features a multi-threshold approach, where the threshold used is increased as long as no leaks are detected. Segmentation of an image takes around 10 seconds on a single-core PC.

15) Automated region growing with manual branch adding and leak trimming:* Tschirren et al. [101] proposed a manual segmentation tool that trim leaks and add branches from an initial airway tree segmentation obtained using a method similar to [70]. Leaks are identified by manually selecting segments that are obtained by skeletonizing the initial segmentation. New branches are added manually by applying region growing on user-placed seed points, where the Dijkstra algorithm is used to connect the new branches to the initial segmentation if they are not connected to the overall segmented airway tree. An average of 59 minutes human interaction time is required to segment a single image.

6.7.1 Fused airway tree from all participating teams

An additional airway tree segmentation obtained via fusing segmentations from all participants is added to the evaluation. A simple voxel based fusion scheme is used, where a voxel is classified to be part of the airway tree as long as it is marked by two or more methods.

The changes in the results when different teams are included in the fusion scheme is investigated via the sequential forward selection (SFS) algorithm, where it is used to determine the sequence of the teams. The SFS algorithm starts with an empty list of teams, and a single team is added into the list at every iteration. At each iteration, the individual performances of the remaining teams, which are not in the list, in combination to the teams in the list are computed, and the team with the best performance is added to the list. The algorithm stops once all teams have been added into the list. The average tree length detected is used as performance measure for the SFS algorithm, which we seek to maximize at each iteration.

6.8 Results

6.8.1 Quality of the reference

Each observer were asked to score all the branches of two to four, randomly selected, segmented airway trees from the participating teams. In comparison to the final labels used for constructing the reference, the observers showed an average accuracy of 93.74%, with a standard deviation of 10.48%. Note that for the cases where the final labels are "don't know", observers are considered correct no matter what labels they assign. Among the errors made, the majority (68.75%) of the errors were due to correct branches being labelled as "partly wrong". This was expected as it is usually difficult to determine whether the marked region belonging to a branch is within the airway wall or not. Besides

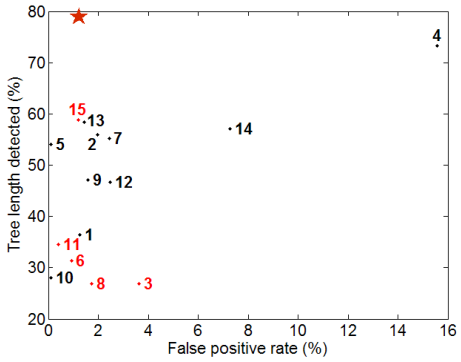

Figure 6.4: Average false positive rate versus tree length detected of all participating teams, with teams in the semi-automated category in red. The fusion scheme is indicated with ⋆.

that, it also depends on how lenient the observers are, which is something that differs from person to person. Errors due to correct branches being labelled as "wrong" and vice versa were less frequent, and covered only of 8.21% and 6.31% of the errors respectively.

Most of the final labels assigned to the branches were assigned without any conflicts, where the same labels were assigned by either both observers in the first phase or the three observers in the second phase of the scoring process, consisting of an average of 94.71% of branches per case. All "don't know" in the final labels were assigned due to the lack of majority in the labels, which consists of an average of 0.73% of branches per case. No "don't know" labels from the observers were present when deciding the final labels.

Prior to generating the final reference, where "partly wrong" regions are relabeled as "wrong", a look at the distribution of the labels from all labelled voxels in the reference shows that majority of labelled voxels are marked as "correct", consisting an average of 81.02% of all labelled voxels. The ratio of voxels marked "partly wrong" is slightly higher than those marked as "wrong", which are 11.16% and 7.12% respectively. At first glance, relabeling 11% "partly wrong" voxels as "wrong" in the final reference may seemed risky. But in truth, only around half of these "partly wrong" region will be "correct". Therefore, mislabelled "correct" regions will probably only consist of 6% of all labelled voxels, which is quite low. Finally, as expected, only a small amount of voxels are marked as "don't know", consisting only 0.70% of all marked voxels on average. Note that the trachea, and the left and right main bronchi were excluded when computing the above percentages.

6.8.2 Results from individual teams

Table 6.3 presents the three evaluation measures for the 15 participating teams and for the fused segmentation obtained in Section 6.7.1, averaged across the 20 test cases. Figure 6.4 gives an overview of the average performance of the participating teams and the fusion scheme in terms of false positive rate over tree length detected. Box plots of tree length detected and false positive rate for the different methods are given in Figure 6.5. Box plots in Figure 6.6 give the branch count and leakage volume from the participating teams on a per case basis. The branch count is defined as number of branches detected correctly, while the leakage volume is defined as the volume of marked voxels that are not within the "correct" region in the reference.

In the box plots, the median is indicated by the red line, and the 25th and 75th percentile are indicated by the lower and upper edges of the box respectively. The lines below and above the box, or "whiskers", represent the largest and smallest values that are within 1.5 times the interquartile range, while the red open circles show all outliers outside this range.

Surface renderings from two cases are given in Figure 6.7 and Figure 6.8, with correct and wrong regions indicated in green and red respectively.

Table 6.3: Evaluation measures averaged across the 20 test cases of each team. * indicates teams in the semi-automated category and the best result from the participating teams for each measurement is indicated in bold. Result from the fusion scheme is indicated using ⋆.

	Branch detected (%)	Tree length detected (%)	False positive rate (%)
(1) Irving *et al.*	43.5	36.4	1.27
(2) Fetita *et al.*	62.8	55.9	1.96
(3*) Pinho *et al.*	32.1	26.9	3.63
(4) Feuerstein *et al.*	**76.5**	**73.3**	15.56
(5) Lo *et al.*	59.8	54.0	0.11
(6*) Fabijanska	36.7	31.3	0.92
(7) Bauer *et al.*	57.9	55.2	2.44
(8*) Mendoza *et al.*	30.9	26.9	1.75
(9) Wiemker *et al.*	56.0	47.1	1.58
(10) Lee *et al.*	32.4	28.1	**0.11**
(11*) Born *et al.*	41.7	34.5	0.41
(12) Weinheimer *et al.*	53.8	46.6	2.47
(13) Bauer(a) *et al.*	63.0	58.4	1.44
(14) van Rikxoort *et al.*	67.2	57.0	7.27
(15*) Tschirren *et al.*	63.1	58.9	1.19
⋆	84.3	78.8	1.22

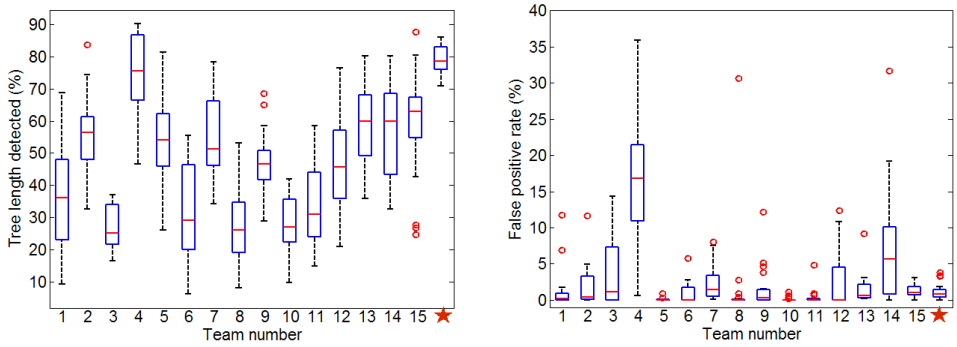

(a) (b)

Figure 6.5: Box plots of (a) tree length detected and (b) false positive rate of the teams. The fusion scheme is indicated with ⋆.

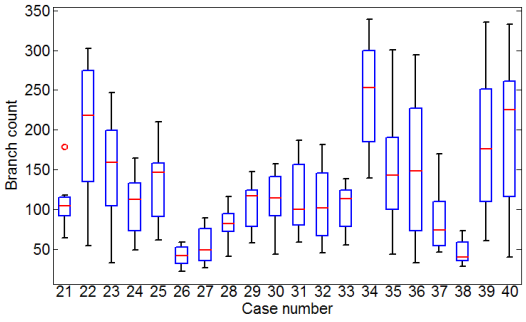

(a)

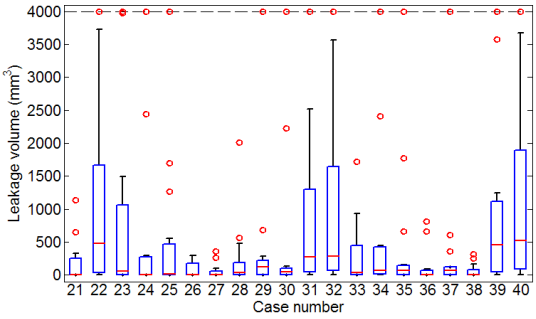

(b)

Figure 6.6: Box plots of (a) branch count and (b) leakage volume, with the maximum leakage volume clipped at 4000 mm^3, of the 20 test cases computed across the 15 participating teams.

6.8.3 Effects of fusing results from different methods

As observed from the results of the individual teams presented in Section 6.8.2, the team with the highest score in terms of average branch length only manage to extract an average 76.5% of the branches in the reference for each case. Figure 6.9 shows a bar plot of the percentage of branches categorized based on the number of participating teams that detected them, averaged across the 20 test cases. Figure 6.10 shows the surface renderings of the reference segmentations of the testing set, with the branches color coded by the number of methods that detected them. As observed, more than 30% of the branches for a case are on average extracted by no more than three methods. A simple fusion scheme, as introduced in Section 6.8.3, results in much better airway tree extracted as observed in Table 6.3 and Figure 6.4, where the results from the fusion scheme have the highest average tree length with a relatively low average false positive rate. Figure 6.11 shows the effects on tree length detected and false positive rate when different team are added into the fusion scheme using the SFS algorithm.

6.9 Discussions

As expected, there appears to be a trade off between sensitivity and specificity in the airway tree extracted by the participating teams. This is shown in Figure 6.4 and Figure 6.5, where it is observed that more complete trees are usually accompanied by a larger percentage of false positives. The most conservative algorithm is that of Lee et al. [52], which obtains the smallest average false positive rate (0.11%) and is among the methods with the lowest average tree length detected (32.4%). On the other hand, the algorithm by Feuerstein et al. [24] is the most explorative one, yielding the highest average tree length detected (76.5%), but at the expense of having the highest average false positive

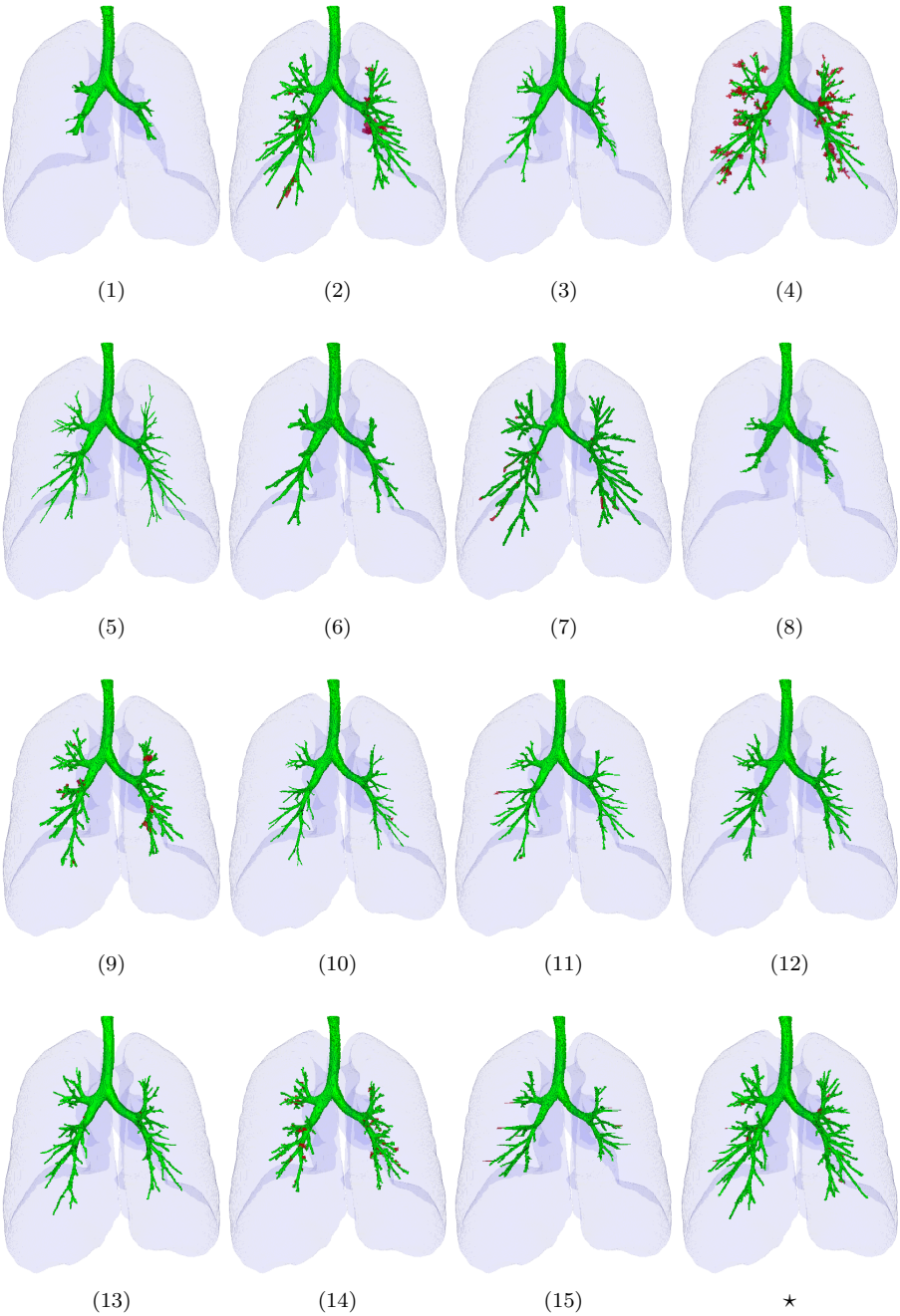

Figure 6.7: Surface renderings of results for case 23, with correct and wrong regions shown in green and red respectively.

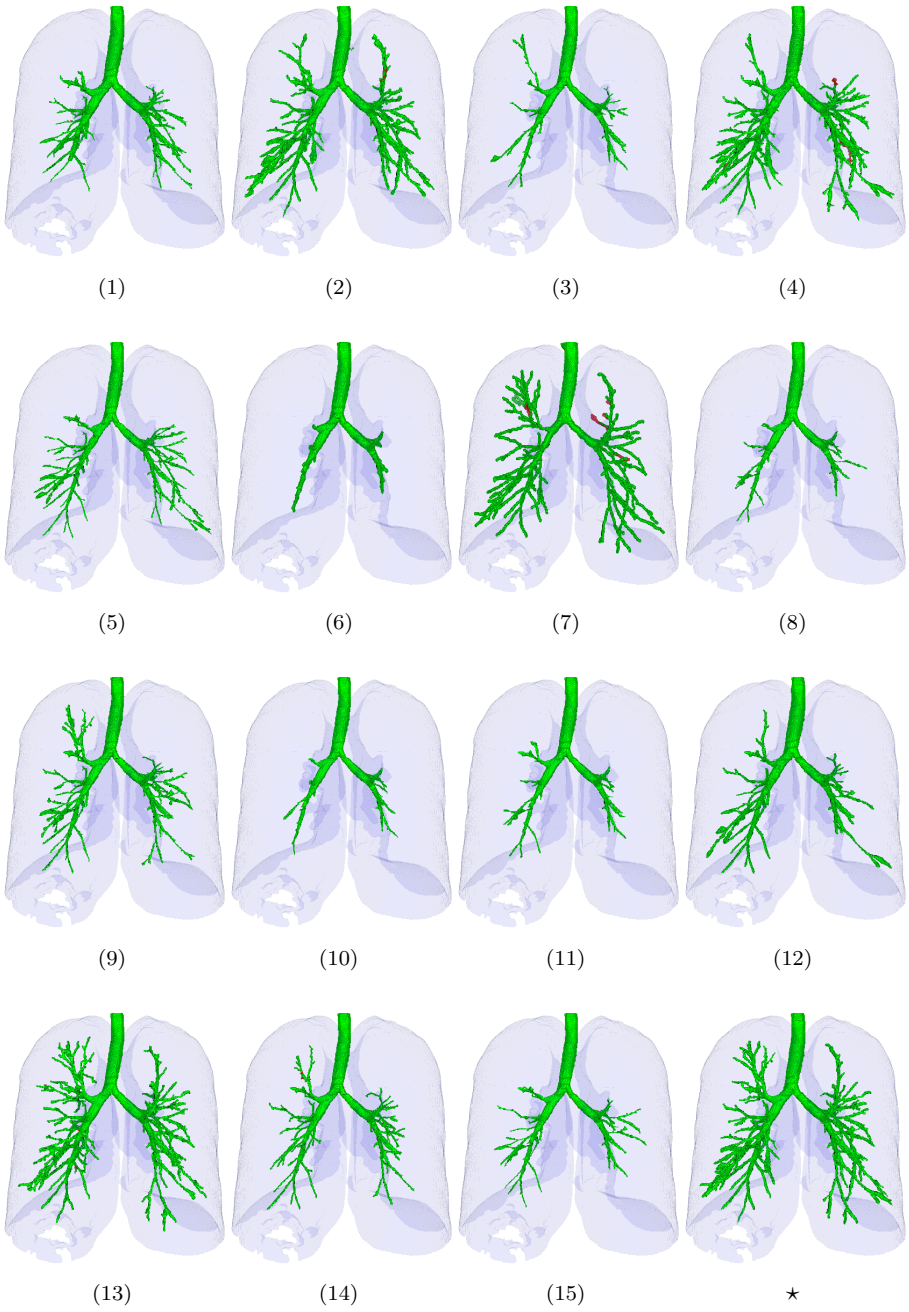

Figure 6.8: Surface renderings of results for case 36, with correct and wrong regions shown in green and red respectively.

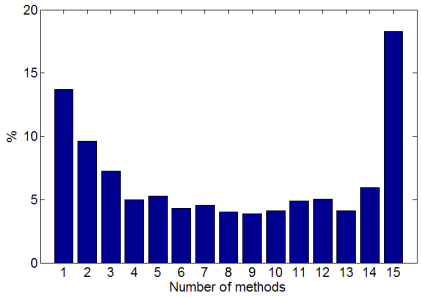

Figure 6.9: Bar plot of the percentage of branches categorized based on the number of participating teams that detected them, averaged across the 20 test cases.

rate (15.56%).

In general, semi-automatic methods perform no better than fully automatic methods. This is probably due to the fact that manual interactions for all semi-automatic methods, except for Tschirren et al. [101], are limited to selecting initial seed points for the trachea [11, 68] or tuning parameters manually [21, 82] for a few test cases.

Because of the use of different CPUs and in some cases the use of GPU during execution, it is not possible to directly compare the execution time of the different algorithms. However, we do observe a wide range of computational time, ranging from less than half a minute to more than an hour. Majority of the execution time falls between two to five minutes.

The box plots of the results for the test cases measured across different teams shown in Figure 6.6 reveal that ultra low dose scans (cases 24, 26, 37, and 38) are generally more difficult to segment than low dose or clinical dose scans. From these scans, significantly fewer branches were extracted ($p < 0.01$ from Student's t-tests) with no significant difference in leakage volume ($p = 0.10$). For the two pairs of low dose and ultra low dose scans (case 24 and 25, and 26 and 27), branch count were significantly higher ($p < 0.01$ from paired Student's t-tests) for the low dose scans (93 branches) than for the ultra low dose (73 branches) scans, while there was no significant difference in leakage volume ($p = 0.54$). The difference in the amount of branches extracted can also be confirmed from the surface renderings of the reference segmentations in Figure 6.10.

From the available paired inspiration and expiration scans (case 21 and 22, and 37 and 38), not only do segmentations of the inspiration scans have more correct branches, but they also have more leakage than their expiration counterparts as well. It is observed that inspiration scans exhibits an average branch count of 145 branches and leakage volume of 942 mm^3 as compared to 76 branches and 115 mm^3 from expiration scans. A paired Student's t-tests shows that these difference are indeed significant, with $p < 0.01$ for both branch count and $p = 0.02$ for leakage volume. The difference in branch count for inspiration and expiration scans is especially obvious from the surface renderings in Figure 6.10.

The image pair case 28 and case 29 consists of scans from the same subject reconstructed using soft and hard kernel respectively. Although the difference in reconstruction is not obvious to a human observer as both scans are marked as middle kernel via visual inspection, significantly more branches ($p < 0.01$) were extracted from the scan constructed using the hard kernel, with an average of 106 branches compared to 80 branches from the soft kernel reconstructed scan. The same can also be observed in the surface renderings in Figure 6.10 of the two case. Although average leakage volume for hard kernel scan was higher, 418 mm^3 compared to 236 mm^3, the difference was not significant ($p = 0.30$).

Among the scans acquired at full inspiration, except for case 22, it is observed that most algorithms leak less on cases from healthy subjects (case 23, 28, 29, 35 and 37) than cases from pathological subjects (case 24-27, 30-34, 36, 39 and 40), as observed in Figure 6.8.2. Among the cases from subjects with pathology, leakage seems to be most pronounced in case 31, 32, 39 and 40, where the pathologies are not mild.

Interestingly, no algorithm came close to detecting the entire reference airway tree, as observed

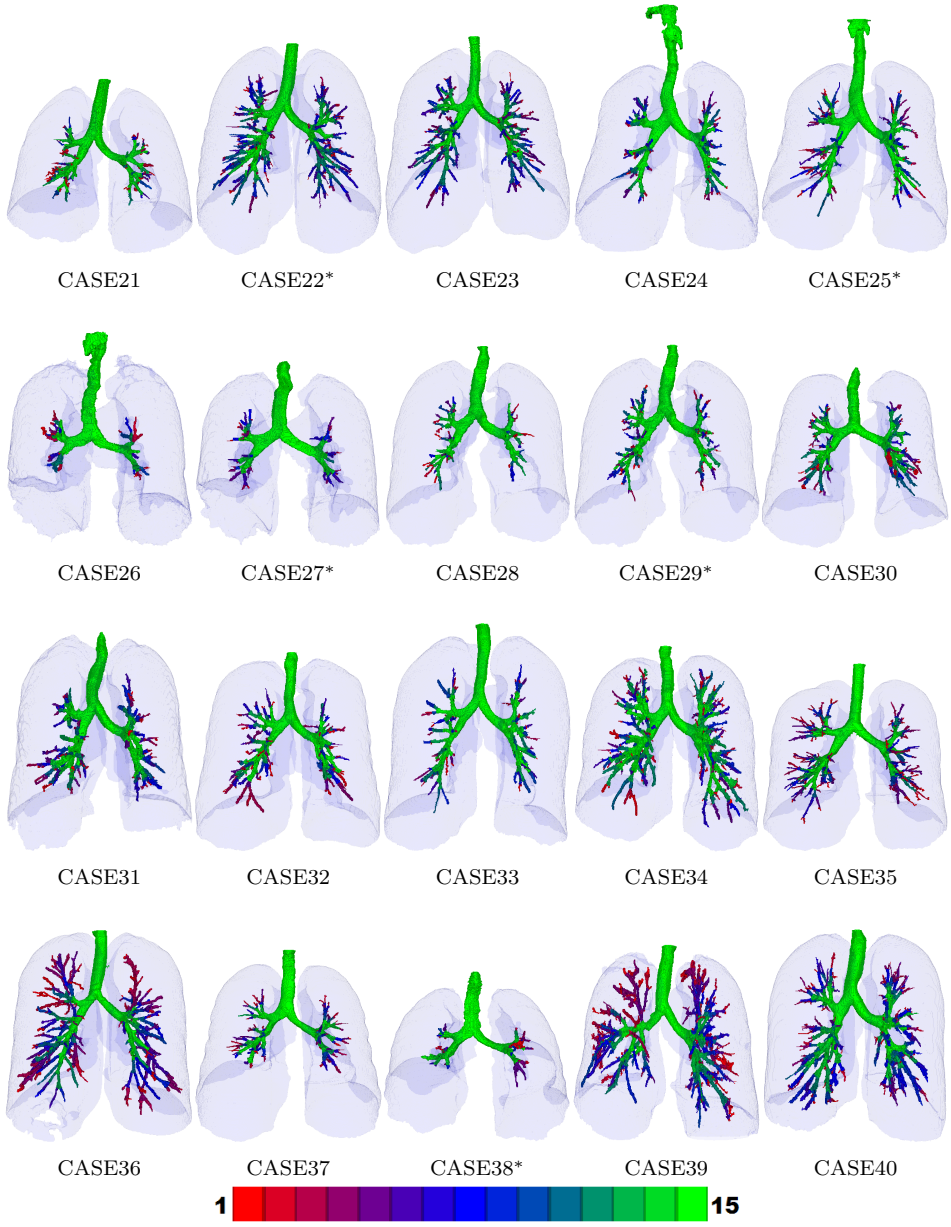

Figure 6.10: Surface renderings of the reference. * indicates that the case is from the same subject as the previous case. The branches are color coded from red (detected by a single team) to green (detected by all 15 teams) as shown by the colorbar at the bottom.

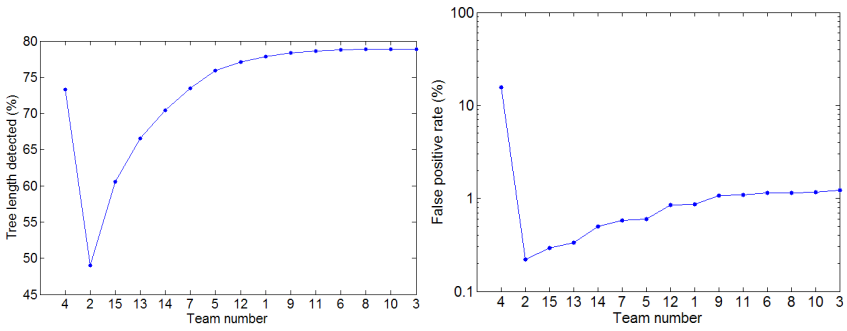

(a) (b)

Figure 6.11: Average tree length detected and false positive rate of including different teams into the fusion scheme using the SFS algorithm. The first left most entry in the x-axis indicates the results are from team 4 alone. The second entry indicates results obtained by fusing team 4 and 2, the third entry indicates results from team 4, 2 and 15, and so on.

from Figure 6.8.2. The highest branch count and tree length detected for each case range from 64.6% to 94.3% and 62.6% to 90.4% respectively, with the average branch detected and tree length detected of less than 77% and 74% respectively. Fusing results from the participating algorithms improves overall results, reaching an average branch detected of 84.3% and average tree length detected of 78.8%, with only an average false positive rate of 1.22%, as shown in Table 6.3. Experiments on the inclusion of the results from different teams using sequential forward selection shows that the tree length detected of the fused results converges quite rapidly, as shown in Figure 6.11(a). This indicates that reasonably good results can be obtained by fusing results from a subset of the participating algorithms.

It should be noted that the fusion scheme presented in Section 6.8.3 is just a simple scheme to illustrate the fact that better results can be obtained by fusing results from different algorithms. The proposed fusion scheme is by no means an extensively optimized fusion scheme, and we expect more elaborate fusion schemes to produce even better results. It is noticed that the average branch detected of the fusion scheme is a lot higher than the average tree length detected, which is 84.3% compared to 78.8%. The reason for this is probably because the fusion scheme uses the same segmentations that make up the reference, thus branch detected of the fusion scheme is bound to be rather good since the evaluation is biased to it by design. Although improvements of the fusion scheme may be overestimated due to this bias, the fact that results from the fusion scheme is better than individual algorithms shows that the different extraction algorithms are actually complementary to each other.

All training and testing data are publicly available at the EXACT'09 website[3]. Besides the evaluation results, the renderings, as seen in Figure 6.7 and 6.8, for the test cases will also be made available at the website. We also plan to make the evaluation service available to the public, and provide both renderings and the performance measures described in Section 6.5 as results. However, due to limited resources, the evaluation will only be made using the currently available reference, without involvement of trained observers. A disadvantage of this would be that new branches not in the current reference will be classified as errors. To solve this, we hope to organize another round of evaluation that involves trained observers in the future, where the reference will be updated and previously submitted results will be re-evaluated.

6.10 Conclusion

A framework for establishing a reference segmentation and using it to evaluate airway extraction algorithms in a standardized manner is presented. This is the first study that performed quantitative evaluation of a large number of different airway tree extraction algorithms (a total of 15 algorithms), which were applied to a single dataset (20 chest CT scans from various institutes) and evaluated using

[3]See http://image.diku.dk/exact/

a reference standard. A total of three performance measures were used to evaluate the sensitivity and specificity of the different algorithms. Results showed that no algorithm is capable of extracting more than an average of 74% of the total length of all branches in the reference. However, the experiments showed that better results can be obtained by a simple fusion scheme that retains regions that are marked by two or more methods, resulting in extracting on average 78.84% of the total length of all branches in the reference, with a relatively low average false positive rate of only 1.22%.

Chapter 7

Airway Tree Extraction with Locally Optimal Paths

This chapter is based on the manuscript "Airway Tree Extraction with Locally Optimal Paths", by P. Lo, J. Sporring, J. J. H. Pedersen and M. de Bruijne, in Medical Image Computing and Computer-Assisted Intervention, Lecture Notes in Computer Science, volume 5762, pp. 51-58, 2009.

Abstract This chapter proposes a method to extract the airway tree from CT images by continually extending the tree with locally optimal paths. This is in contrast to commonly used region growing based approaches that only search the space of the immediate neighbors. The result is a much more robust method for tree extraction that can overcome local occlusions. The cost function for obtaining the optimal paths takes into account of an airway probability map as well as measures of airway shape and orientation derived from multi-scale Hessian eigen analysis on the airway probability. Significant improvements were achieved compared to a region growing based method, with up to 36% longer trees at a slight increase of false positive rate.

7.1 Introduction

Analysis of the airways in computed tomography (CT) is crucial for the understanding of various lung diseases [9]. However due to the difficulties of the extraction process, the airways remain among the least understood structures in the lungs.

Most methods used for segmenting the airway tree from CT images are based on the concept of region growing [58, 90, 100, 106]. The main problem with the standard region growing approach is that the segmentation may "leak" to surrounding lung parenchyma, if the contrast with the airway wall is low due to e.g. noise or pathology. Various strategies have been used to solve this problem, e.g. using geometric criteria to detect and remove leakage [90, 100, 106], or using improved appearance models to avoid leakage [58].

In this chapter, we propose a new method for airway tree extraction method that continually extends the tree with locally optimal paths. The advantage of using such a path search approach is that the algorithm is able to look further ahead and can therefore overcome local occlusions. Occlusions may be caused for instance by noise or pathologies such as mucus plugging. Using the trained appearance model described in [58] as the basis for our cost function, the Dijkstra algorithm is applied within a sphere centered at a seed point to obtain candidate airway paths. Candidate paths that satisfy various criteria based on airway probability, shape, and orientation are retained, and potential bifurcation points and new end points are stored and subsequently used as new seed points. This process is repeated until no more valid candidate paths can be found.

The work is inspired by minimal path based approaches in vessel segmentation and diffusion tensor imaging (DTI) tractography (see e.g. [39, 40]). These approaches are however typically either limited to extracting a single optimal path or require a user to specify the end points in advance. Another example is [32], where a complete vessel tree is extracted as a collection of optimal paths from a converged fast marching algorithm. In contrast to [32], we may be able to extract also less salient branches and thus find a more complete tree by searching for optimal paths locally and recursively. The notion of performing optimal path extraction locally was recently also proposed in [8], where various examples are shown in which a local approach outperforms the global approach. However, the focus of that paper was on extracting single paths or contours and the method is not capable of handling bifurcations.

Our work is similar in spirit to [30], which aims at reaching a more global solution for airway segmentation by detecting potential airway branches throughout the lungs with a tube detection scheme, and subsequently connecting these using a graph search method. However, our method is more flexible and can be customized to other tree segmentation tasks by simply modifying the cost function and the confidence measure.

7.2 Tracking locally optimal paths

This section explains how the Dijkstra algorithm is applied locally and how the optimal paths are selected. We assume that a cost function F, a confidence measure D, and a list of initial candidate points are provided. A candidate point is a point that belongs to a previously extracted airway branch, and for which the departing paths are not yet extracted. Each candidate point is associated with the orientation and the average radius of the airway branch it belongs to.

At every iteration, a candidate point is taken from the list and evaluated. New paths extending from the candidate points are generated through a process of candidate path extraction and selection. Additional new candidate points from these new paths will then be added into the list. The iterative process ends once no more candidate points are available for evaluation.

7.2.1 Extracting candidate paths

Given a candidate point $\vec{x}_0$, with the branch orientation $\vec{d}_0$, optimal paths are computed from $\vec{x}_0$ to every point within a sphere of radius r_s using the Dijkstra algorithm. We refer to these optimal paths as the candidate path from $\vec{x}_0$ to $\vec{x}$. The traveling cost between two neighboring voxels is computed using cost function F.

Candidate paths are extracted for all points on the surface of the sphere that satisfy the following conditions:

1) Local minima: End points should form a local minimum, in terms of minimal cost from $\vec{x}_0$, on the surface of the sphere.

2) Departing angle: To limit the search to branches that do not deviate too much from the initial direction, end points should satisfy $\angle(\vec{x} - \vec{x}_0), \vec{d}_0 \leq \alpha$, as shown in Fig. 7.1(c).

7.2.2 Evaluating the candidate paths

The most likely airway branches are selected from the extracted candidate paths by the following three selection criteria in a low to high cost order:

1) Confidence: The majority of points on a path must have high confidence measure D. Hence, we require the Nth percentile of the confidence measure of a path to be greater than β in order to be selected.

2) Straightness: As airway branches are relatively straight in general, we require a path C to satisfy $l_{path}(C) < \gamma l(\vec{x}_0, \vec{x})$, where $l_{path}(C)$ is the length of the path C and $l(\vec{x}_0, \vec{x})$ is the distance from $\vec{x}_0$ to $\vec{x}$.

3) Non-overlap: Selected paths are not allowed to overlap each other and should be at least δ mm apart. The distance between a candidate path and the previously selected paths is measured as the minimum distance between the end point of the candidate path and the points in the selected

paths. We also ensure that a selected candidate path will not intersect with other paths obtained from previously evaluated candidate points. Prior to applying this criterion, an additional trimming process is added to remove low confidence points at the end of the path, which exist because of the used of fixed end points. The trimmed path is stored if the path is selected.

A maximum of N_{max} paths is retained.

7.2.3 Updating the list of candidate points

The end points of the newly selected paths are added to the list of candidate points. All potential bifurcation points, defined as points where candidate paths depart from a selected path, are also added to the list. The direction for each of the new candidate points is the direction of the selected path it belongs to.

7.3 Cost function

Unlike most current airway segmentation methods [30, 90, 100, 106] that use only image intensity, our proposed method operates on the soft classification resulting from a voxel classification based appearance model [58].

The appearance model uses a K nearest neighbors (KNN) classifier that is trained to differentiate between voxels from airway and non-airway classes using various local image descriptors at different scales. To circumvent the requirement for high-quality ground truth segmentations of the complete airway tree, we follow the interactive training procedure described in [58]. A moderated KNN [48] output is used, where the posterior probability of a feature vector $\vec{f}(\vec{x})$, obtained at voxel position $\vec{x}$, to belong to the airway class is defined as

$$P_A(\vec{f}(\vec{x})) = \frac{K_A(\vec{f}(\vec{x})) + 1}{K + 2},$$

where $K_A(\vec{f}(\vec{x}))$ is the number of nearest neighbors around $\vec{f}(\vec{x})$ that belong to the airway class obtained from a total of K nearest neighbors.

The airway probability $P_A(\vec{f}(\vec{x}))$ is used directly as the confidence measure D in Section 7.2 to discard unlikely paths. The cost function F is designed such that local paths are searched in the direction of probable airways, which appear as bright, cylindrical structures in P_A. The local orientation of the airways is derived through multi-scale Hessian eigen analysis on the airway probability map. The scale is selected for each voxel independently using the scale normalized [57] Frobenius norm of the Hessian matrix $\omega(\sigma_i) = \sigma_i^2\sqrt{\lambda_1(\sigma_i)^2 + \lambda_2(\sigma_i)^2 + \lambda_3(\sigma_i)^2}$, where $|\lambda_1| \geq |\lambda_2| \geq |\lambda_3|$ are the eigenvalues of the Hessian matrix. The local scale, σ_l, is then obtained as the smallest scale that corresponds to a local maximum of $\omega(\sigma_i)$ across a list of scales $\{\sigma_{min}, \ldots, \sigma_{max}\}$, where σ_{max} is chosen slightly larger than the current airway radius. A measure M_{tube}, indicating how well the surrounding image structure fits the model of a solid bright tube, can then be defined as

$$M_{tube}(\vec{x}) = \begin{cases} 0, & \lambda_1(\sigma_l) \geq 0 \text{ or } \lambda_2(\sigma_l) \geq 0, \\ \frac{|\lambda_2(\sigma_l)| - |\lambda_3(\sigma_l)|}{|\lambda_2(\sigma_l)|}, & \text{otherwise,} \end{cases}$$

The orientation of the tube at $\vec{x}$ is given by $\vec{v}_3(\vec{x})$, which is the eigenvector corresponding to $\lambda_3(\sigma_l)$.

The cost function F combines the airway probability, tubeness measure, and airway direction estimates as:

$$F(\vec{x}_s, \vec{x}_t) = \frac{\|\vec{x}_s - \vec{x}_t\|_2}{| < \frac{\vec{x}_s - \vec{x}_t}{\|\vec{x}_s - \vec{x}_t\|_2}, \vec{v}_3(\vec{x}_t) > | P_A(\vec{f}(\vec{x}_t)(1 + M_{tube}(\vec{x}_t))},$$

where $\vec{x}_s$ and $\vec{x}_t$ is the source and target location. The cost $F(\vec{x}_s, \vec{x}_t)$ is low, when both the local airway probability is high and the propagation direction is parallel with the estimated airway orientation. The term with M_{tube} is used to lower the cost further, when the local structure at $\vec{x}_t$ resembles a solid bright tube.

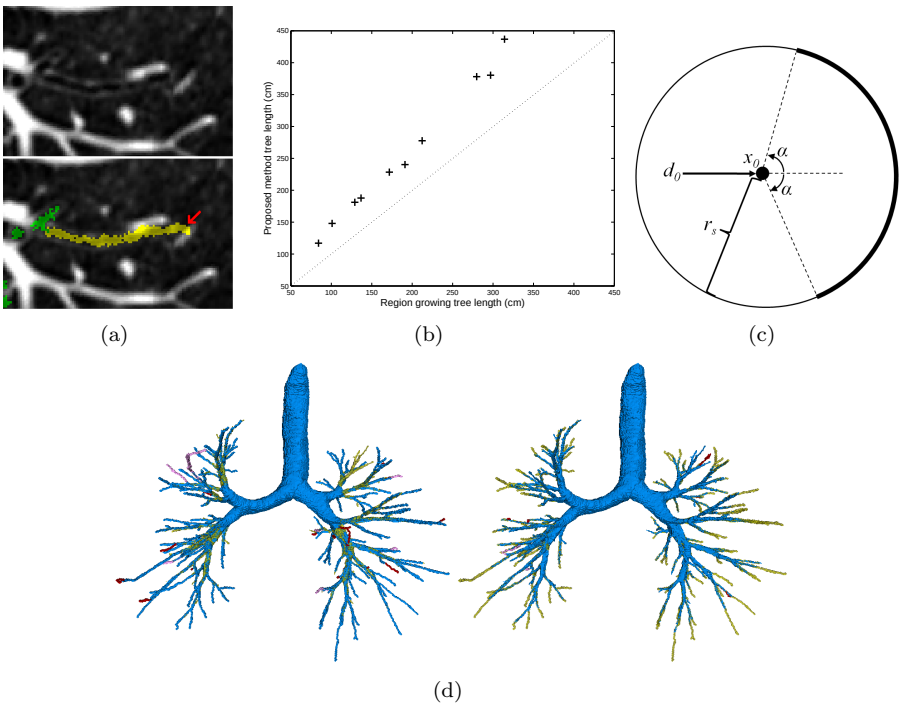

Figure 7.1: (a) Example of a case where it is not possible to segment the correct part (the largest part of the branch) from the leakage, with the branch segment highlighted in yellow and an arrow indicating the leakage. (b) A scatter plot of the tree length obtained by both methods for the 10 test cases. (c) A schematic of the search sphere. (d) Surface rendering of the results from proposed method (left) and region growing based method (right), with correct regions in blue, missing regions in yellow, partly wrong regions in purple and false positives in red.

7.4 Experiment and results

Experiments were conducted on low-dose CT images from the Danish Lung Cancer Screening Trial (DLCST) [80], where participants were current or former smokers at an age between 50-70 years. All images had a slice thickness of 1 mm and in-plane voxel size ranging from 0.72 to 0.78 mm. A total of 32 randomly selected images were used for the training of the voxel classification based appearance model. The method was tested on an additional 10 randomly selected CT scans from different subjects.

Results were compared to a region growing based method that uses a trained airway appearance model and exploits the fact that orientation of airways and vessels are similar [58]. Airways branches from the second up to and including the third generation obtained by this method were used to initialize the proposed method. Since extraction of these first few branches is relatively easy, simpler methods such as intensity based region growing could be used for initialization instead.

The centerlines of the initial segmentation were used as the initial set of candidate points needed for the proposed method. A simplified version of the segmentation algorithm presented in [90], without any leakage detection, were used to extract the centerlines. The direction and radius associated to each candidate point is derived from the branch they belong to. For newly added candidate points, the radius is simply propagated directly from their parents.

7.4.1 Parameter and settings

For extracting the optimal paths, the radius of the search sphere was set to $r_s = 20$ mm and the maximum allowed angle to $\alpha = 100$ degrees. In selection of the optimal paths, at most $N = 30$ percent of points on the path may have a confidence below $\beta = 0.5$, the straightness measure $\gamma = 1.05$, minimum required distance between selected optimal paths $\delta = 3$ mm. The maximum number of

selected paths from a single candidate point N_{max} was set to 2.

For the appearance model, $K = 21$ was used for the KNN classifier and 7 scales distributed exponentially from 0.5 to 3.5 mm were used both to generate the features (refer to [58] for details) and for the multi-scale Hessian eigen analysis.

To prevent paths from growing into border of the lungs, candidate points that were within 3 mm of the lung surface were not evaluated.

7.4.2 Results

All results were evaluated manually by an experienced observer using the dedicated airway segmentation evaluation tool developed for the EXACT'09 airway extraction challenge [61]. The results were divided into individual branches using the simplified version of [90], without any leakage detection. Airway branches are subsequently visually inspected and classified into the categories 'correct', 'wrong', or 'partly wrong' based on several views obtained from different cut planes at different angles and positions. Branches are said to be correct, if there is no leakage visible at all. A branch is said to be wrong, if the majority (more than 50%) of it is leakage, and partly wrong, if the majority is correct.

As the evaluation tool was designed for evaluating segmentation and not centerlines, results from the proposed method were dilated in order to make them compatible with the evaluation tool.

As the evaluation process only separates branches at bifurcations, we are unable to isolate leakage from a branch, if it extends from the endpoints and does not bifurcate. This usually occurred at the end segments, where a whole branch is classified as 'partly wrong' due to a small amount of leakage at the end. Figure 7.1(a) shows an example of this situation. All partly wrong regions were excluded from further evaluation.

Compared to the results from the region growing approach, we observe a significant ($p < 0.01$) increase of 36% in total tree length for the results of the proposed method, from an average of 192 cm tree length to 258 cm. The tree length is defined as the sum of the lengths of all branches obtained, excluding the trachea and main bronchi. The average false positive rate, computed as a percentage of the total tree with the trachea and main bronchi excluded, was 3.79% for the proposed method, slightly larger than for the region growing based method (1.35%). The total number of branches extracted was similar for both methods, around 174 branches on average. A plot showing the tree length for the 10 cases from the two methods are given in Fig. 7.1(b). Surface renderings of a randomly selected case are given in Fig. 7.1(d).

Finally, a third segmentation was constructed as the union of the airway trees extracted from the two methods. A comparison of the union against the result from the region growing based method shows a significant ($p < 0.01$) increase of 9% in branch count. Results from the proposed method cover 96% of the tree length in the union, while results from the region growing based method only have 71% coverage.

7.5 Discussion and conclusions

The proposed method improves results significantly, especially in terms of tree length, where an average improvement of 36% was observed. The branches missed by the proposed method that were extracted correctly using the region growing based method were very short, with an average length of 5 mm. Despite having similar branch count when comparing the proposed method and the region growing based method, significant increase (9%) in branch count was observed when comparing the results from the region growing based method against the union. This indicates that the proposed method is capable of obtaining new branches, and not only merely extending branches obtainable by the region growing based method. It should be noted that the multi-scale version of the work from [58], used for comparison, is a method that gives results comparable to other recent state of the art methods such as [106].

In the current work, the estimate of the airway radius is propagated from old to new candidate points unaltered. Although this estimate is only used to determine the upper bound in the scale selection of Section 7.3, more reliable estimates of local tubeness and tube orientation may be found if

the radius is updated with each bifurcation to reflect the overall decrease in airway diameter towards the higher generations. Alternatively, an airway wall segmentation algorithm such as [45] could be used to obtain the radius, with the additional advantage that the result can be directly used for airway dimension analysis.

Another potential improvement would be to introduce a "multi-radius" scheme, which involves searching paths within multiple search spheres of different radii. This might increase the number of new branches found, as shorter branches may then be extracted using a smaller radius, while occlusions can still be overcome using the larger radii.

In conclusion, an airway tree extraction method that is based on a recursive search for locally optimal paths is presented. In contrast to common airway tree segmentation methods that only consider the immediate neighbors of seed points, our method considers both the appearance and structure of a whole path. This enables the method to extend past local occlusions caused by noise or pathologies such as mucus plugging. The proposed method handles bifurcations automatically, which is a topic rarely touched upon by optimal path tracking methods.

Chapter 8

Vessel Tree Extraction using Locally Optimal Paths

This chapter is based on the manuscript "Vessel Tree Extraction Using Locally Optimal Paths", by P. Lo, B. van Ginneken and M. de Bruijne, in IEEE International Symposium on Biomedical Imaging, To appear, 2010.

Abstract This chapter proposes a method to extract vessel trees by continually extending detected branches with locally optimal paths. Our approach uses a cost function from a multiscale vessel enhancement filter. Optimal paths are selected based on rules that take into account the geometric characteristics of the vessel tree. Experiments were performed on 10 low dose chest CT scans for which the pulmonary vessel trees were extracted. The proposed method is shown to extract a better connected vessel tree and extract more of the small peripheral vessels in comparison to applying a threshold on the output of the vessel enhancement filter.

8.1 Introduction

Extraction of vessels in computed tomography (CT) is a key component for the diagnosis of vascular diseases, such as stenosis, hypertension and embolism. The vessel tree is also an important cue for registering images of the same patient [34]. Another role of vessel tree extraction is as an aid to improve detection of other structures, such as lung nodules detection, where it has been shown to help in reducing false positives [1].

In this chapter, we propose a method for vessel tree extraction that continually extends detected branches with locally optimal paths, based on the work presented in [62], which was originally used for airway tree extraction. Based on a cost function that uses the vesselness response from a multiscale vessel enhancement filter [26], the Dijkstra algorithm is applied within a sphere centered around a given seed point to obtain candidate vessel paths. Subsequently, plausible paths are selected based on a series of criteria such as vesselness response, shape, orientation and geometric relationship with other extracted paths. The end points and potential bifurcation points from the newly selected paths are stored and used as new seed points. The process is repeated until all seed points have been processed.

The radius of the search sphere should be sufficiently large so that one can derive meaningful statistical and geometrical information from the extracted path. However, a large search radius also means that true, short paths will most probably be rejected. A multi-radius implementation is introduced in this work to allow detecting such short branches. The path selection process is designed such that paths obtained from search spheres with larger radii have a higher chance of being selected than those from smaller radii.

An advantage of the proposed method is its robustness to local low vesselness response, either due to bifurcations or artifacts. This is because the decisions are made based on the statistics of a path, thus allowing the proposed method to ignore such outliers. This is in contrast to growing based methods [12,64] that make decisions based on a single voxel. This is also the case with certain tracking methods [32, 56] that rely on threshold based stopping criteria.

Different strategies have been employed to deal with problems related to vesselness response, such as [5] that perturbs data locally to overcome effects of noise and [1] that connects tubes and bifurcations that are detected using different filters. An extra step taken by the proposed method is the incorporation of prior knowledge of the geometrical characteristics of the vessel tree to suppress false positives, such as furcation number, furcation angle, and the fact that branches do not intersect.

The proposed method is used to extract pulmonary vessel tree from low dose chest CT scans from the ANODE09 [107] dataset. The results are compared to those obtained by thresholding the vesselness filter output, and we demonstrate that the proposed method finds better connected segmentations and is capable of finding connections to thin, peripheral vessels.

8.2 Tracking locally optimal paths

The tracking of locally optimal paths starts with a given list of seed points (see Section 8.4.1 for details on seed points extraction). At every iteration, a seed point is taken from the list and evaluated. New paths extending from the seed point are generated through a process of candidate path extraction and path selection. New seed points from these paths are then added to the list. The iterative process ends once no more seed points are available for evaluation.

Given a seed point $\vec{x}_0$ and its accompanying branch orientation of $\vec{d_0}$, optimal paths are computed from $\vec{x}_0$ to every point on the surface of a sphere of radius r_s. These optimal paths are computed via the Dijkstra algorithm, based on a cost function $\mathcal{F}$ (see Section 8.3 for details) that defines the cost of traveling between neighboring voxels. We refer to these local optimal paths as candidate paths.

The list of candidate paths is sorted in an ascending manner, according to the total cost needed to travel from the seed point to their respective end points. Then, from low to high cost, the first N_{max} candidate paths fulfilling the following criteria are selected:

1) Local minima: The total cost needed to travel from the seed point to the end point should form a local minimum on the surface of the search sphere.

2) Departing angle: Vessels usually bifurcate within a certain angle, we enforce this by only selecting paths with an end point $\vec{x}$ that satisfy the condition $\angle(\vec{x} - \vec{x}_0), \vec{d_0} \leq 100°$.

3) Straightness: A small section of vessel should be relatively straight. We therefore require a path C to satisfy $l_{path}(C) < \gamma l(\vec{x}_0, \vec{x})$, where $l_{path}(C)$ is the length of the path and $l(\vec{x}_0, \vec{x})$ is the shortest possible distance from $\vec{x}_0$ to $\vec{x}$ in the image grid.

4) Vesselness: The majority of points on a path must have high vesselness response (see Section 8.3). Hence, we require the Nth percentile of the vesselness response of a path to be greater than ρ_p. In addition, any trailing points with vesselness response lower than ρ_t at the end of the path are removed.

5) Distance from selected paths: Except for the seed point itself, a path is not allowed to have any overlap with any of the selected paths and should be at least 4.5 mm away from other selected paths in order to be selected. The distance of a candidate path from a selected path is measured as the minimum distance between the end point of the candidate path and the points in the selected path.

6) Proximity with previously extracted paths: A path is not allowed to be within a proximity of previously extracted paths obtained from previously evaluated seed points. We mark the proximity of previously extracted paths by dilating them with a sphere of radius 1.5 mm.

All rejected candidate paths that satisfy criteria 1 and 2 are treated as possible bifurcations and are stored during the selection process. After the selected paths are obtained, points where the stored rejected candidate paths branch off from the selected paths are extracted. These points are added along with the end points of the selected paths into the list of seed points. The accompanying branch orientation for each of these new seed points is the orientation of the selected path it belongs to.

As the list of seed points consists also of all possible bifurcation points, a seed point needs not be an end point of a previously extracted path. Therefore, it is important to also take into account the

path that the seed point belongs to, if the seed point is not an end point of a previously extracted path. This is done by extracting the section of the previously extracted path that is within the search sphere. If the end point of this previously extracted path lies within the search sphere, possible extensions from this end point to the surface of the search sphere are also extracted. The possible extensions are subjected to the selection criteria above, where only a single path will be selected. In the case where all the possible extensions are rejected, the previously extracted path itself will be added to the list of selected paths. The selection process then proceeds with selecting $N_{max} - 1$ paths from the list of candidate paths.

The above explained the tracking of locally optimal paths using a single search radius. In case of multiple search radii, paths are first searched using the largest radius. Then, if the maximum number of selected paths N_{max} is not yet reached, the search process continues with the next smaller radius.

8.3 Cost function

We used the multiscale vessel enhancement filter proposed by Frangi et al. [26] as the basis for the cost function. This filter is designed to detect bright tubular structures in 3D image based on Hessian eigen analysis, and it defines a vesselness response as follows:

$$\mathcal{V}(\sigma) = \begin{cases} 0, & \lambda_2 > 0 \text{ or } \lambda_3 > 0, \\ \mathcal{R}_\mathcal{A}\mathcal{R}_\mathcal{B}\mathcal{S}, & \text{otherwise,} \end{cases}$$

$$\mathcal{R}_\mathcal{A} = 1 - \exp\left(-\frac{1}{2\alpha^2}\left|\frac{\lambda_2}{\lambda_3}\right|^2\right),$$

$$\mathcal{R}_\mathcal{B} = \exp\left(-\frac{1}{2\beta^2}\frac{|\lambda_1|^2}{|\lambda_2\lambda_3|}\right),$$

$$\mathcal{S} = 1 - \exp\left(-\frac{1}{2c^2}\left(\lambda_1^2 + \lambda_2^2 + \lambda_3^2\right)\right),$$

where $|\lambda_1| \leq |\lambda_2| \leq |\lambda_3|$ are the three eigenvalues of the Hessian matrix, while α, β and c are thresholds that control the sensitivity of the filter. The second order derivatives of the Hessian matrix were computed by convolving the image with the scale normalized second order derivatives of a Gaussian kernel, with a standard deviation or scale of σ. The vesselness response is calculated over a range of scales from σ_{min} to σ_{max}, where the final vesselness response for a point $\vec{x}$ is given as

$$\mathcal{V}(\vec{x}) = \max_{\sigma_{min} \geq \sigma \geq \sigma_{max}} \mathcal{V}(\vec{x}, \sigma) \tag{8.1}$$

In order to avoid false positive response from low intensity noise, $\mathcal{V}$ is set to 0 for voxels with intensity below I_{min}.

The cost function $\mathcal{F}$ provides the cost needed to travel from a source point $\vec{x}_s$ to a neighboring point $\vec{x}_t$, and is defined as

$$\mathcal{F}(\vec{x}_s, \vec{x}_t) = \frac{\|\vec{x}_s - \vec{x}_t\|_2}{\max\left(\left|\left\langle \frac{\vec{x}_s - \vec{x}_t}{\|\vec{x}_s - \vec{x}_t\|_2}, \vec{v}_1 \right\rangle\right| \mathcal{V}\left(\vec{x}_t\right), \epsilon\right)} \tag{8.2}$$

where $\vec{v}_1$ is the eigenvector corresponding to λ_1, indicating the direction along the vessel axis, computed at the scale selected in (8.1), and ϵ is a small constant meant to prevent division by zero. The dot product with $\vec{v}_1$ introduces a directional affinity into the cost function, making it cheaper to travel in the direction of the vessel axis.

8.4 Experiment and results

We evaluated the proposed method on a subset of the ANODE09 [107] dataset , consisting of 10 low-dose CT scans of current or former heavy smokers between 50 and 75 years of age. All images have a slice thickness of 1 mm, a slice spacing of 0.7 mm, and an in plane resolution between 0.62 to 0.81 mm. Results from the proposed method were compared to vessel trees segmented by thresholding on the vesselness response (8.1).

8.4.1 Preprocessing and seed points extraction

Both the proposed method and the thresholding of the vesselness were only performed within the lung fields, segmented with the algorithm used in [62]. The lung fields were eroded by a sphere structure with a radius of three voxels to avoid false high vesselness response regions at the border of the lungs.

For the extraction of the vessel seed points, the lung fields were eroded again by three voxels. All local maxima in vesselness response on the inner lung border were selected as initial seed points. A point is considered to be in the inner lung border if it is at the border and that a point taken three voxel from it in the direction away from the centroid of the lungs is within the lung fields. Paths were searched in the outward direction by setting the initial branch orientation $\vec{d}_0$ for each seed point $\vec{x}_0$ to $(\vec{x}_0 - \vec{x}_c) / \|\vec{x}_0 - \vec{x}_c\|_2$, where $\vec{x}_c$ is the centroid of the lung fields.

8.4.2 Parameters

The parameters used for the vesselness filter (8.1) were $\alpha = 0.5$, $\beta = 0.5$, $c = 50$, and $I_{min} = -850$ HU. A total of 10 scales ranging from 1 to 5.5 mm, exponentially distributed, were used. Tuning was performed on one image from the testing dataset.

For the tracking of locally optimal paths, two search radii r_s were used, which were 15 and 7.5 mm. Different length ratios γ were used for the different search radii, which were to 1.2 for $r_s = 15$ mm and 1.05 for $r_s = 7.5$ mm. The maximum number of selected paths for each seed point was $N_{max} = 2$. At most N = 30 percent of points on the path may have a vesselness below $\rho_p = 0.05$, and all trailing points with vesselness below $\rho_t = 0.035$ were removed. The settings for the locally optimal paths were based on prior knowledge on the geometric characteristics of the pulmonary vessels and were fine tuned using a few cropped sections of the image that was used previously to tune the parameters of the vesselness filter.

8.4.3 Results

The threshold for the thresholding method was set to ρ_p, which was 0.05. Segmentation results from both methods were visually inspected. Only minor false positives from airway walls and nodules were observed for both methods. Surface renderings of the extracted vessels from a random case are shown in Figure 8.1.

The total vessel tree length and the length of non overlapping vessel branch segments, which signifies the length of vessel branches discovered by one method but not by the other, were used to compare both results quantitatively. The length were estimated by multiplying the number of voxels from the centerlines with the average voxel size, which is 0.71 mm. The centerlines for the results from thresholding were extracted using the thinning algorithm presented in [114]. Vessel segments were considered overlapping if their centerline voxels were less than 2 voxels apart. In order to remove possible spurious structures due to noise, individual centerlines of less than 10 voxels (ca. 7 mm) in length, were removed and not included in the evaluation. The average vessel tree length extracted was 55.61 m for the proposed method and 52.17 m for thresholding. Based on the average length of non overlapping vessel branch segments, a total of 4.45 m vessel branch segments were missed by the proposed method and 8.93 m were missed by thresholding.

Connected component analysis performed on the unfiltered results from both method gives an average of 5004 disconnected components for thresholding and 191 for the proposed method. For the filtered results, the number of disconnected components for both thresholding and the proposed method are 430 and 160 respectively.

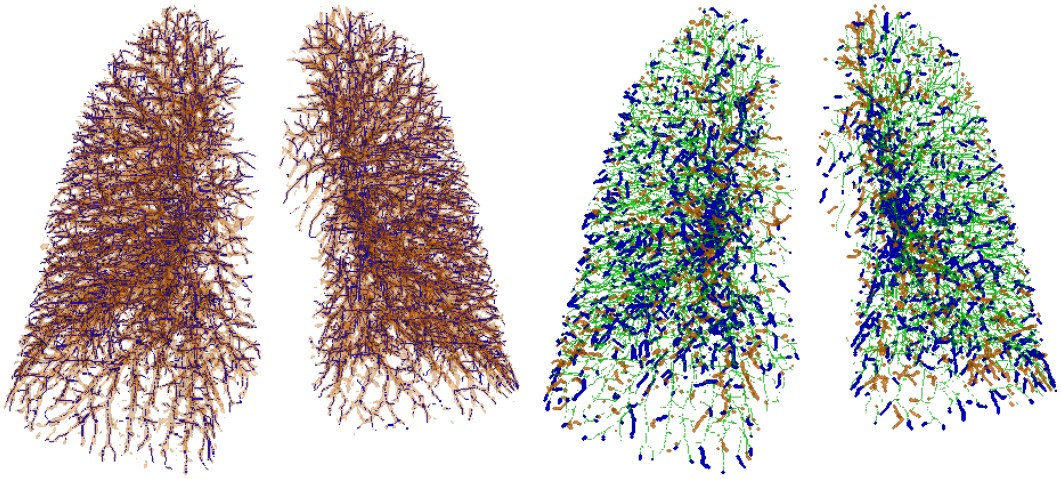

(a) (b)

Figure 8.1: (a) Surface rendering of the extracted vessels from the proposed method in blue and those from thresholding in orange. (b) Surface rendering (after removal of small structures) showing the overlapping centerlines in green, non overlapping centerlines of the proposed method in blue and the thresholding in orange, with the non overlapping centerlines dilated slightly for clarity.

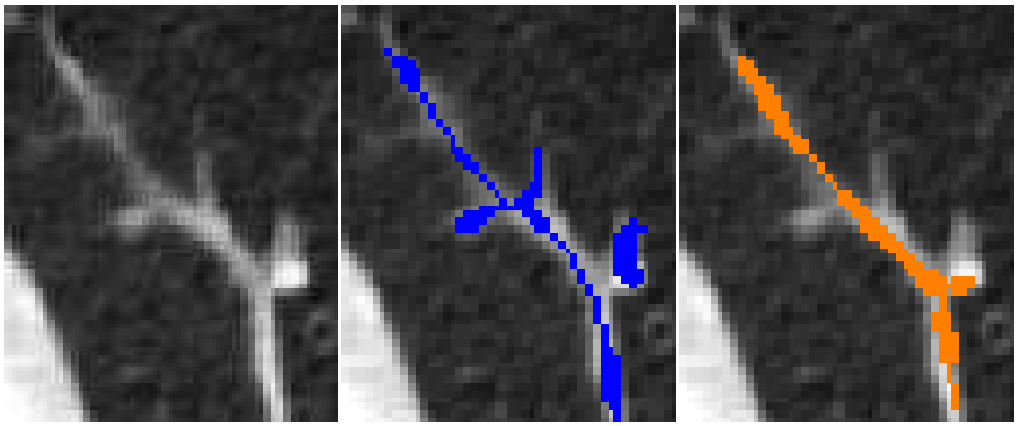

(a) (b) (c)

Figure 8.2: An example showing the ability of the proposed method to reach into thin, peripheral vessels. (a) Original image. (b) Dilated paths extracted from proposed method in blue. (c) Dilated centerlines from thresholding in orange.

8.5 Discussion and conclusion

As observed from the surface rendering in Figure 8.1, the proposed method is capable of tracking the thin, peripheral vessels, while thresholding can only extract them partially in small and disconnected sections. This is further verified by the number of disconnected components, vessel tree length and the total length of non overlapping centerlines, which show that the vessel trees extracted by the proposed method are both better connected and more complete. Figure 8.2 shows a slice where the proposed method was able to track into regions that centerlines from thresholding missed.

Even though the proposed method allows small regions lower than the vesselness threshold to be included in the segmentation, it contained in general fewer false positives than the results from the thresholding approach. This can be explained by the connectivity requirements and the inclusion of geometrical constraints in the path search approach. A few false positives remained present in the results of the proposed method, mainly in the airway walls near the hylar region. If necessary, these false positive branches could easily be removed by discarding paths that run too close to a segmented airway tree, such as those from [62].

A limitation of our current implementation is that we do not have optimal seed points for initialization, but yet we assume that each seed point is the root of a vessel. This causes vessels grown from different seed points to compete with each other, leading to connected vessels being split and some vessels being missed. This is shown in Figure 8.1(b), where it can be observed that some vessels around the inner part of the lungs are not detected correctly.

Our future work will focus on extracting suitable seed points in the main pulmonary arteries and veins using atlas based methods, which we expect to solve the problem mentioned above, resulting in better connectivity and even fewer missed vessel branches. Another possibility is the extraction of arteries, for applications such as emboli detection, which can be achieved by simply providing the proposed method with only seed points of the main arteries, therefore removing the need for artery vein separation.

In conclusion, we have proposed a vessel extraction algorithm that extends locally optimal paths in an iterative manner. Due to the local nature of these optimal paths, geometrical constraints such as bifurcation angle, straightness, and proximity to other vessel branches can be incorporated naturally. Compared to vessel segmentation based on a threshold on the vesselness filter response, the local path search is better able to detect the thin, peripheral vessels.

Chapter 9

Summary and General Conclusion

9.1 Summary

Chapter 1 presented a brief introduction on the background of the medical context that motivates this thesis, which includes a brief explanation of Chronic Obstructive Pulmonary Disease (COPD), and the reason for using scans from the Danish Lung Cancer Screening Trial (DLCST) study to investigate COPD. An outline of the thesis and a list of contributions were also given in the end of this chapter.

A region growing based lung segmentation algorithm targeted for low dose screening computed tomography (CT) scans was presented in **Chapter 2**. The algorithm starts by detecting part of the trachea automatically and segmenting a coarse airway tree. Subsequently, the trachea, and the left and right main bronchi are extracted from the coarse airway tree, and both left and right main bronchi are used to initiate two coupled region growing algorithms to segment the left and right lungs respectively. Wrongly added regions belonging to the esophagus are detected using an algorithm that looks for cylindrical object in the segmented lung fields, which are removed from segmented lung fields to form the final lung segmentation. An optional smoothing and hole filling process is also included into the lung segmentation algorithm. The lung segmentation algorithm was evaluated manually on 200 CT scans, where only minor errors were identified in nine scans, and has been applied successfully to over 6000 CT scans from the DLCST study. The algorithm has also been applied to clinical CT scans with pathologies, where acceptable results were obtained. This lung segmentation algorithm also serves as a preprocessing step for the rest of the chapters in this thesis.

Chapter 3 applies the lung segmentation algorithm presented in the previous chapter to study the effects of changes in smoking behavior on CT based emphysema quantification. The study consisted of baseline and one year follow up scans from a total of 548 subjects from the DLCST study with known smoking history. A volume adjusted 15th percentile density (PD15) [91] was used to quantify emphysema in the CT scans. Effects of smoking on the adjusted PD15 were studied using a cross-sectional model, where the adjusted PD15 of a group of former smokers were compared against a group of current smokers. The change in the adjusted PD15 between the base line and one year follow up scans were studied in a longitudinal model, where the subjects were categorized into continuous smokers, recent quitters, continuous ex-smokers and re-starters based on the changes in their smoking behavior. The analysis of both models were performed based on the assumption of a linear model, which also takes into account sex, age, pack years and body mass index, as well as time between scans for the longitudinal model. From the cross-sectional model, it was observed that adjusted PD15 of the current smokers were higher than the ex-smokers, with a difference of 10.6 g/L ($p < 0.001$). The longitudinal model showed that the changes in adjusted PD15 were only significantly different from continuous smokers in the first (-6.2 g/L, $p < 0.001$) and second (-3.6 g/L, $p < 0.001$) year of smoking cessation. In conclusion, the study has showed that changes in smoking behavior have an effect on lung density in CT, indicating the importance of taking smoking status into account when using CT lung density to assess the severity of emphysema.

Chapter 4 described a method for constructing a voxel classification based airway appearance model and a way of using it in combination with a segmented vessel tree to segment airway tree in CT.

The novelty of the appearance model lies in the usage of easily obtained low quality segmentations for training purpose and applying for the task of airway tree segmentation. For each training image, two separate segmentations of the airway tree were obtained using an interactive intensity based region growing algorithm: a manual segmentation, which is error free, and a leaked segmentation, which contains more branches but at the cost of having a certain amount of errors. The manual segmentation defines the regions where airway class were to be extracted, while the leaked segmentation is meant to reduce possible false negatives of airways when extracting the non-airway class. Additionally, extraction of training samples for airway class was made such that approximately the same number of samples were extracted at the different depths of the airway tree to prevent the large airways from dominating the training samples. Finally, the extracted samples were used to construct a k nearest neighbors (KNN) classifier that uses an optimal set of features selected using sequential floating forward feature selection. By making use of the fact that airways are accompanied by arteries, resulting in both structures having the same orientation, a vessel orientation similarity measure was used along with the appearance model. The objective of the vessel orientation similarity measure is to overcome regions within the airway tree where using appearance model alone will result in low probability because of either noise or artifacts. Experiments were conducted on 250 low dose CT scans from the DLCST study, where 32 scans were use for training purpose. The results were validated qualitatively via visual inspection and quantitatively using an automated leakage detection algorithm based on [90]. Experiment results showed that the appearance based region growing approach resulted in more complete airway tree being segmented (20% longer trees) and was less proned to leakage (50% lower false positive rate) as compared to intensity based region growing. Combining the appearance model with vessel orientation similarity resulted in even more significant ($p < 0.01$) improvements than only using the appearance model alone, with on average 7% increase in the total length of branches extracted correctly.

The robustness of the appearance model presented in the previous chapter is demonstrated in **Chapter 5**. In this chapter, the 3D region growing algorithm that uses both the KNN based airway appearance model and the vessel orientation similarity measure was trained and applied on a diverse set of CT scans from the "Extraction of airways from CT" (EXACT'09) dataset, which consists of 20 training images and 20 test images. Except for two minor modifications in the initialization and in the parameter tuning step to cope with the variations in the quality of the scans, the whole framework remains the same as the previous chapter. Quantitative evaluation of the results was performed by EXACT'09, which was based on a manually constructed reference. In comparison to 15 other methods that participated in EXACT'09, our method is able to extract a fair amount of airway branches, while still maintains a very low false positive rate. Our method has an average percentage of tree length detected of 54% and a false positive rate of 0.11%, while the most conservative and most explorative methods in EXACT'09 have an average tree length detected and false positive rate of 28.1% and 0.11%, and 73.3% and 15.56% respectively.

Chapter 6 presented the EXACT'09 study, which is the first study to compare the performance of several different algorithms quantitatively using a standard dataset. An alternative method for constructing a reference for the airway trees using segmentations from existing algorithms was used in this study in order to circumvent the need to manually segment airway trees, which is a task both extremely laborious and impractical. Airway tree segmentations from the algorithms to be evaluated were subdivided into their individual branches, whereupon these individual branches were visually inspected and evaluated. Individual branches that were determined to be correct by human observers were then combined to form the airway tree reference. The study consists of a dataset of 40 CT scans of various quality from different scanners, with 20 for training or tuning purposes and another 20 for testing. Reference segmentations were constructed for the 20 test set, in which the performance measures of the participating teams were computed and evaluated. A total of 15 algorithms developed by different research groups were evaluated. In addition, results from a simple voxel voting based fusion scheme that uses results from all algorithms were also included in the evaluation. Three performance measures were computed for each method, which includes two sensitivity measures and a specificity measure. The two sensitivity measures are branch detected, which is the fraction of branches in the reference that are correctly detected, and tree length detected, which is the total length of correctly detected branches over the total length of the branches in the reference. False positive rate is used as the specificity measure, which gives the fraction of voxels that are incorrectly marked as airways

according to the reference. Interestingly, results from the evaluation shows that no one method was capable of extracting (nearly) all the branches in the reference correctly, with the most explorative method achieving only around 76% in terms of branch and tree length detected. Results from the fusion scheme showed that the branches detected by the different algorithms were quite different, and that better results can easily be achieved by fusing results from different methods. It has been shown that a simple fusion scheme that assumes a voxel belongs to the airways if it is marked by more than one method gives results better than those from the participating teams, with an average tree length detected of 78.8% and average false positive rate of 1.22%.

The problem of airway tree segmentation was revisited again in **Chapter 7**. Instead of the common voxel based growing approach, a path based growing approach that continually extends a tree with locally optimal paths is presented. The locally optimal paths were defined within a fixed radius search sphere, and obtained by applying the Dijkstra algorithm to a cost function that is based on the appearance model described in Chapter 4, and on Hessian eigen analysis based shape and orientation information. The most probable paths were then selected through a series of rules that take into account various geometric characteristics of an airway branch segment. Possible branching points and the end points of the selected paths were extracted and added to a list of candidate points, which were used to generate subsequent optimal paths. The whole iterative process stopped once all candidate points are processed. Because decisions are made based on a path, the presented algorithm can overcome local regions of low airway probability from the appearance model in actual airways, which would otherwise block voxel based algorithms, resulting in a whole subtree being missed. Experiments were conducted on 10 CT scans from the DLCST study and compared to airway trees extracted using the algorithm presented in Chapter 4. Resulting segmentations were evaluated manually using the evaluation software used in Chapter 6. We observed significant improvements from the locally optimal paths approach, with up to 36% longer trees compared to the previous region growing approach at the price of a slight increase in false positive rate.

Chapter 8 presented an extension of the locally optimal paths approach to the problem of pulmonary vessel segmentation. The cost function was adapted to use a multiscale vessel enhancement filter along with a Hessian eigenvector based directional affinity. Two improvements were introduced to the locally optimal paths approach. The first improvement was the use of multiple radii search spheres, which enables the extraction of short vessels using small radius search sphere without losing the robustness of having a search sphere with large radius. The second improvement was that the rules for the selection of optimal paths were modified to take previously selected paths into account, which improves the monitoring of furcation number and the overall appearance of the extracted centerlines. Experiments were conducted on 10 CT scans from the ANODE09 [107] dataset and results were compared against those obtained by applying a threshold on the vessel enhancement filter. Results from the experiments showed that that the locally optimal paths approach was able to extract a better connected vessel tree with more of the small peripheral vessels in comparison to applying a threshold on the output of the vessel enhancement filter.

9.2 General discussion and conclusions

Several methods for segmenting different lung structures, namely the lung parenchyma, airway tree and vessel tree, were presented in this thesis. The different techniques employed in this thesis for the various segmentation tasks mainly consisted of a combination of machine learning based, rule based and model based segmentation techniques.

The lung segmentation algorithm presented in Chapter 2 is a typical rule based method, where a series of rules were applied in stages. The basic assumption is that lungs in CT are of lower intensities than surrounding structures. Experiment results have shown that the presented lung segmentation algorithm performs well on both low dose CT scans from the DLCST study and also on various CT scans from other studies. In a more general note, compared to other region growing based method that uses the same intensity based assumption, we expect our lung segmentation algorithm to have similar or slightly better performance, because of the extra esophagus detection and removal process. To compare with the more advanced model based methods that include more prior knowledge of the lungs, such as shape model [54] or templates [93,110], we should use the lung segmentation algorithm

with the optional smoothing and hole filling process described in Section 2.3.4. In this case, there are two situations where the presented algorithm will perform worse:

1. Certain regions in the diaphragm that separates the lungs and the bowels have low intensity, especially in thick slice CT scans, causing the segmentation from proposed method to leak into the bowels.

2. The lungs have large dense pathologies touching the pleura, which will either appear as "dents" on the surface of the segmented lung fields, or "block" the region growing process from marking certain lung regions.

However, the above two situations rarely occurs in thin slice CT scans of relatively healthy subjects used in the DLCST study, which explains the good performance of the proposed algorithm. It should be noted that the model based methods are also not without disadvantages. One of the more obvious problems with the model based methods is their tendency to slightly over or under segment the lungs, due to certain shape or smoothness related constraints. For CT scans of subjects with dense pathologies, this is generally not a problem as the improvements in results outweigh the errors, when compared to results from region growing based methods. However, for cases without dense pathologies, which region growing based algorithms excel in, results from such algorithms may be more preferable than the model based methods.

A large portion of this thesis is devoted to solving the problem of airway tree extraction. A supervised machine learning based approach for airway tree segmentation is presented, where a voxel classification based airway appearance model is used. Despite using low quality airway tree segmentations that are incomplete for training, we have shown that good results can be obtained as long as proper measures are taken to reduce possible false negatives and to account for the different branch size. Since we can only be certain of what is airways and what is not airways within the region surrounding of the training segmentations, the appearance model trained as such is therefore only valid within the vicinity of the airway tree. This constraint makes region growing based techniques ideal to be used for obtaining segmentation from the appearance model.

As responses from the airway appearance model can be quite noisy, simple region growing strategy is insufficient to fully utilize the potential of the airway appearance model. As pointed out in Chapter 4, it was often observed that a whole subtree was missed due to a small number of false positives from the appearance model at the beginning of the subtree, even though the rest of the subtree was detected correctly by the appearance model. In order to better utilize the airway appearance model, two different approaches were proposed: the vessel guided approach (see Chapter 4) and the locally optimal paths approach (see Chapter 7).

Between the two proposed approaches, the vessel guided approach has the advantage of being computationally cheaper, as it is only applying region growing on an objective function that combines response from the appearance model and the vessel orientation similarity measure. Another advantage of the vessel guided approach is the use of additional priors other than the appearance for decision making, as appearance alone is often insufficient for differentiating airways and surrounding lung tissues (see Section 1.1 and Figure 1.3). For this reason, although results from the locally optimal paths approach are generally better than those from the vessel guided approach in terms of total length of branches extracted, there are quite a number of branches that are extracted by the latter but not by the former approach, as shown in Chapter 7.

The locally optimal paths approach is capable of making use of geometrical priors and overcoming local obstructions due to noise, which are the main advantages of this approach over general voxel based growing approaches, such as the vessel guided approach in Chapter 4. Another advantage is the flexibility of its framework, as new priors (e.g. vessel orientation similarity measure) can be introduced either into the cost function or as part of the path selection rules. However, the main downside of this approach is that it is computationally expensive, as it involves performing the relatively expensive Dijkstra algorithm on a large number of small regions.

Measurement of airway dimension remains one of the main application of airway tree segmentation algorithm. Common approaches to obtaining airway dimension measurements, e.g. radius of airway lumen and airway wall thickness, usually involve segmentation of the airway tree, followed by an extraction of centerlines and finally the re-segmentation of the airway lumen and airway walls, where

the airway dimension measurements are computed [81,100,117]. It is in general difficult to merge both extraction of the tree, and the segmentation of lumen and walls together in a single framework, as the former operates at the voxel level, while the latter operates on the centerlines. Since the locally optimal paths approach operates directly at the centerline level, it offers a possibility to combine these two segmentation processes into a single framework. An advantage of such a combined framework is that priors in relation to the airway lumen and airway walls can now be directly used in the tree extraction process, which may prove to be useful for detecting and avoiding leakages.

A hand crafted appearance model of the vessels, which is based on the multiscale vessel enhancement filter [26], is used along with the locally optimal paths approach to extract pulmonary vessel trees in Chapter 8. Because of the relatively simple appearance of vessels in CT, which resemble solid bright tubes, the vessels can be described easily using Hessian eigen analysis. Although the model is known to be unable to handle bifurcations, this is overcome by the use of a low threshold value and the locally optimal paths approach. Therefore, there is no need for a voxel classification based appearance model, which is relatively harder to implement due to the need of training data. However, because of the simplistic assumption of the appearance of vessels in CT, this appearance model is only valid for CT scans from relatively healthy subjects. When CT scans from pathological subjects is of concern, especially those with dense pathologies in the lungs, the appearance model usually has a tendency to also give high responses on pathological regions, resulting in a high false positive rate. For such CT scans, it will probably be more appropriate to use a voxel classification based appearance model, as such model will be able to learn how to differentiate between actual vessels and dense pathological regions, provided that appropriate training data is available.

Another reason for using a voxel classification based vessel appearance model instead of a hand crafted appearance model will be that it now becomes possible to represent both airways and vessels using a single classification based appearance model. This offers the possibility to extract both structures using a single locally optimal paths framework, which makes it possible to introduce additional rules into the framework that take into account the relationship between airways and vessels, such as similarity in orientation, as shown in Chapter 4, and proximity between both structures, as in [97]. An advantage of this co-segmentation framework is that a more complete airway tree and a vessel tree with less false positives (mainly due to airway walls) can now be extracted. In addition, both arteries and veins may also be extracted individually by incorporating information from the airways [13], which is needed for analysis of certain diseases, such as hypertension and pulmonary embolism.

Chapter 6 presents the EXACT'09 evaluation framework for evaluating airway extraction algorithms. In order to ensure the consistencies of the labels assigned, the scoring of branches in the EXACT'09 evaluation framework is made such that it can only be performed by properly trained human observers that were involved in the study. A limitation of this closed scoring process is that it is difficult to extend EXACT'09 to be a standard for evaluating different algorithms, such as the nodule detection competition ANODE09[1] [107] and the Rotterdam coronary artery algorithm evaluation framework[2], where researchers from all over the world are free to submit results from their algorithms any time they like. Although evaluation of new methods can be made using current established reference, it has the drawback that new branches found by newly submitted methods will be treated as false positives and thus limiting the reliability of the evaluation, as mentioned in Chapter 6.

A possible way to implement an open scoring process for EXACT'09 would be to present human observers with a scored branch of known label along with a new branch, where the label assigned to the former will serve as an indication of confidence for the label assigned to the latter. This idea is similar to the reCAPTCHA project[3], which is used to assist the digitization of text in books. In addition, web based training sessions can also be conducted online by assigning observers with scored branches of known labels, where the true label is presented whenever a wrong label is given. Provided that a large enough pool of observers participate in the open scoring process, it will be possible to update the reference with newly submitted methods as frequent as possible, and thus improving the reliability of the resulting evaluation. Reference for the training set can also be updated in such a manner and be made publicly available, making state of the art airway tree training reference available for research groups all over the world. A downside of this open scoring based evaluation framework,

[1] See http://anode09.isi.uu.nl/details.php
[2] See http://coronary.bigr.nl/
[3] See http://recaptcha.net/

however, is that it opens up the possibility to train on the testing set by continually optimizing based on the provided evaluation measurements. This is made even worse by the fact that it is not easy to add new images into the dataset, due to the extra work involved.

Bibliography

[1] G. Agam, S. G. Armato III, and C. Wu. Vessel tree reconstruction in thoracic CT scans with application to nodule detection. *IEEE Transactions on Medical Imaging*, 24(4):486–499, April 2005.

[2] S. Arya, D. M. Mount, N. S. Netanyahu, R. Silverman, and A. Y. Wu. An optimal algorithm for approximate nearest neighbor searching fixed dimensions. *Journal of the ACM*, 45(6):891–923, 1998.

[3] H. Ashraf, P. Tønnesen, J. H. Pedersen, A. Dirksen, H. Thorsen, and M. Døssing. Effect of CT screening on smoking habits at 1-year follow-up in the Danish lung cancer screening trial (DLCST). *Thorax*, 64(5):388–392, May 2009.

[4] D. Aykac, E. Hoffman, G. McLennan, and J. Reinhardt. Segmentation and analysis of the human airway tree from three-dimensional X-ray CT images. *IEEE Transactions on Medical Imaging*, 22(8):940–950, 2003.

[5] S. R. Aylward and E. Bullitt. Initialization, noise, singularities, and scale in height ridge traversal for tubular object centerline extraction. *IEEE Transactions on Medical Imaging*, 21(2):61–75, Feb. 2002.

[6] C. Bauer, H. Bischof, and R. Beichel. Segmentation of airways based on gradient vector flow. In *Proc. of Second International Workshop on Pulmonary Image Analysis*, pages 191–201, 2009.

[7] C. Bauer, T. Pock, H. Bischof, and R. Beichel. Airway tree reconstruction based on tube detection. In *Proc. of Second International Workshop on Pulmonary Image Analysis*, pages 203–213, 2009.

[8] F. Benmansour and L. Cohen. Fast object segmentation by growing minimal paths from a single point on 2D or 3D images. *Journal of Mathematical Imaging and Vision*, 33(2):209–221, 2009.

[9] P. Berger, V. Perot, P. Desbarats, J. M. T. de Lara, R. Marthan, and F. Laurent. Airway wall thickness in cigarette smokers: quantitative thin-section CT assessment. *Radiology*, 235(3):1055–1064, Jun 2005.

[10] C. Bergin, N. Mller, D. M. Nichols, G. Lillington, J. C. Hogg, B. Mullen, M. R. Grymaloski, S. Osborne, and P. D. Par. The diagnosis of emphysema. A computed tomographic-pathologic correlation. *American Review of Respiratory Disease*, 133(4):541–546, Apr 1986.

[11] S. Born, D. Iwamaru, M. Pfeifle, and D. Bartz. Three-step segmentation of the lower airways with advanced leakage-control. In *Proc. of Second International Workshop on Pulmonary Image Analysis*, pages 239–250, 2009.

[12] T. Bülow, C. Lorenz, and S. Renisch. A general framework for tree segmentation and reconstruction from medical volume data. In *Medical Image Computing and Computer-Assisted Intervention*, volume 3216 of *Lecture Notes in Computer Science*, pages 533–540, 2004.

[13] T. Bülow, R. Wiemker, T. Blaffert, C. Lorenz, and S. Renisch. Automatic extraction of the pulmonary artery tree from multi-slice CT data. In A. A. Amini and A. Manduca, editors, *Medical Imaging 2005: Physiology, Function, and Structure from Medical Images*, volume 5746, pages 730–740. SPIE, 2005.

[14] P. Burney, S. Suissa, J. B. Soriano, W. M. Vollmer, G. Viegi, S. D. Sullivan, L. M. Fabbri, D. D. Sin, P. Ernst, D. Coultas, J. Bourbeau, D. W. Mapel, K. Weiss, T. McLaughlin, D. Price, M. C. J. M. Sturkenboom, R. Taylor, and G. W. Hagan. The pharmacoepidemiology of COPD: Recent advances and methodological discussion. *European Respiratory Journal Supplement*, 43:1s–44s, Sep 2003.

[15] R. Castillo, E. Castillo, R. Guerra, V. E. Johnson, T. McPhail, A. K. Garg, and T. Guerrero. A framework for evaluation of deformable image registration spatial accuracy using large landmark point sets. *Physics in Medicine and Biology*, 54(7):1849–1870, Apr 2009.

[16] T. Cover and P. Hart. Nearest neighbor pattern classification. *IEEE Transactions on Information Theory*, 13(1):21–27, 1967.

[17] H. O. Coxson. Chairman's summary. In *Proceedings of the American Thoracic Society*, volume 5, pages 874 – 877, 2008.

[18] H. O. Coxson and R. M. Rogers. Quantitative computed tomography of chronic obstructive pulmonary disease. *Academic Radiology*, 12(11):1457–1463, Nov 2005.

[19] A. Dirksen, E. Piitulainen, D. G. Parr, C. Deng, M. Wencker, S. B. Shaker, and R. A. Stockley. Exploring the role of CT densitometry: A randomised study of augmentation therapy in Alpha1-antitrypsin deficiency. *European Respiratory Journal*, 33(6):1345–1353, Jun 2009.

[20] R. O. Duda, P. E. Hart, and D. G. Stork. *Pattern Classification*, chapter 4.4, pages 174 – 177. Wiley-Interscience, 2 edition, 2001.

[21] A. Fabijanska. Results of applying two-pass region growing algorithm for airway tree segmentation to MDCT chest scans from EXACT database. In *Proc. of Second International Workshop on Pulmonary Image Analysis*, pages 251–260, 2009.

[22] C. Fetita, M. Ortner, P.-Y. Brillet, F. Prêteux, and P. Grenier. A morphological-aggregative approach for 3D segmentation of pulmonary airways from generic MSCT acquisitions. In *Proc. of Second International Workshop on Pulmonary Image Analysis*, pages 215–226, 2009.

[23] C. Fetita, F. Preteux, C. Beigelman-Aubry, and P. Grenier. Pulmonary airways: 3-D reconstruction from multislice CT and clinical investigation. *IEEE Transactions on Medical Imaging*, 23(11):1353–1364, 2004.

[24] M. Feuerstein, T. Kitasaka, and K. Mori. Adaptive branch tracing and image sharpening for airway tree extraction in 3-D chest CT. In *Proc. of Second International Workshop on Pulmonary Image Analysis*, pages 273–284, 2009.

[25] C. Fletcher and R. Peto. The natural history of chronic airflow obstruction. *British Medical Journal*, 1:1645 – 1648, June 1977.

[26] A. Frangi, W. Niessen, K. Vincken, and M. Viergever. Multiscale vessel enhancement filtering. In *Medical Image Computing and Computer-Assisted Interventation*, volume 1496 of *Lecture Notes in Computer Science*, pages 130–137, 1998.

[27] E. Gamble, D. C. Grootendorst, K. Hattotuwa, T. O'Shaughnessy, F. S. F. Ram, Y. Qiu, J. Zhu, A. M. Vignola, C. Kroegel, F. Morell, I. D. Pavord, K. F. Rabe, P. K. Jeffery, and N. C. Barnes. Airway mucosal inflammation in COPD is similar in smokers and ex-smokers: A pooled analysis. *European Respiratory Journal*, 30(3):467–471, Sep 2007.

[28] B. Ghaye, D. Szapiro, J. M. Fanchamps, and R. F. Dondelinger. Congenital bronchial abnormalities revisited. *Radiographics*, 21(1):105–119, 2001.

[29] V. Gorbunova, P. Lo, H. Ashraf, A. Dirksen, M. Nielsen, and M. D. Bruijne. Weight preserving image registration for monitoring disease progression in lung CT. In *Medical Image Computing and Computer-Assisted Intervention*, volume 5242 of *Lecture Notes in Computer Science*, pages 863–870, 2008.

[30] M. W. Graham, J. D. Gibbs, and W. E. Higgins. Robust system for human airway-tree segmentation. In *Medical Imaging 2008: Image Processing*, volume 6914, page 69141J. SPIE, 2008.

[31] T. B. Grydeland, A. Dirksen, H. O. Coxson, S. G. Pillai, S. Sharma, G. E. Eide, A. Gulsvik, and P. S. Bakke. Quantitative computed tomography: Emphysema and airway wall thickness by sex, age and smoking. *European Respiratory Journal*, 34(4):858–865, Oct 2009.

[32] M. A. Gülsün and H. Tek. Robust vessel tree modeling. In *Medical Image Computing and Computer-Assisted Intervention*, volume 5241 of *Lecture Notes in Computer Science*, pages 602–611, 2008.

[33] J. W. Gurney, K. K. Jones, R. A. Robbins, G. L. Gossman, K. J. Nelson, D. Daughton, J. R. Spurzem, and S. I. Rennard. Regional distribution of emphysema: Correlation of high-resolution CT with pulmonary function tests in unselected smokers. *Radiology*, 183(2):457–463, May 1992.

[34] A. Hilsmann, T. Vik, M. Kaus, K. Franks, J.-P. Bissonette, T. Purdie, A. Bejzak, and T. Aach. Deformable 4DCT lung registration with vessel bifurcations. In *Proc. 21st International Congress on Computer Assisted Radiology and Surgery (CARS)*, pages 44–60, Berlin, June 27–30 2007. Elsevier.

[35] J. C. Hogg, F. Chu, S. Utokaparch, R. Woods, W. M. Elliott, L. Buzatu, R. M. Cherniack, R. M. Rogers, F. C. Sciurba, H. O. Coxson, and P. D. Par. The nature of small-airway obstruction in chronic obstructive pulmonary disease. *The New England Journal of Medicine*, 350(26):2645–2653, Jun 2004.

[36] M. Hou, Y. Morishita, T. Iijima, K. Mase, Y. Dai, S. Sekine, and M. Noguchi. The implication of anthracosis in the development of pulmonary adenocarcinoma. *Cancer Science*, 89(12):1251–1256, 1998.

[37] S. Hu, E. Hoffman, and J. Reinhardt. Automatic lung segmentation for accurate quantitation of volumetric X-ray CT images. *IEEE Transactions on Medical Imaging*, 20(6):490–498, June 2001.

[38] B. Irving, P. Taylor, and A. Todd-Pokropek. 3D segmentation of the airway tree using a morphology based method. In *Proc. of Second International Workshop on Pulmonary Image Analysis*, pages 297–307, 2009.

[39] M. Jackowski, X. Papademetris, L. W. Dobrucki, A. J. Sinusas, and L. H. Staib. Characterizing vascular connectivity from microCT images. In *Medical Image Computing and Computer-Assisted Intervention*, volume 3750 of *Lecture Notes in Computer Science*, pages 701–708, 2005.

[40] S. Jbabdi, P. Bellec, R. Toro, J. Daunizeau, M. Pélégrini-Issac, and H. Benali. Accurate anisotropic fast marching for diffusion-based geodesic tractography. *Journal of Biomedical Imaging*, 2008(1):1–12, 2008.

[41] P. W. Jones, F. H. Quirk, and C. M. Baveystock. The St George's Respiratory Questionnaire. *Respiratory Medicine*, 85 Suppl B:25–31; discussion 33–7, Sep 1991.

[42] P. Jones, S. Lareau, and D. A. Mahler. Measuring the effects of COPD on the patient. *Respiratory Medicine*, 99 Suppl B:S11–S18, Dec 2005.

[43] R. E. Kanner, J. E. Connett, D. E. Williams, and A. S. Buist. Effects of randomized assignment to a smoking cessation intervention and changes in smoking habits on respiratory symptoms in smokers with early chronic obstructive pulmonary disease: The Lung Health Study. *American Journal of Medicine*, 106(4):410–416, Apr 1999.

[44] A. P. Kiraly, W. E. Higgins, E. A. Hoffman, G. McLennan, and J. M. Reinhardt. 3D human airway segmentation for virtual bronchoscopy. In *SPIE Medical Imaging 2002: Physiology and Function from Multidimensional Images*, volume 4683, pages 16–29, 2002.

[45] A. Kiraly, B. Odry, D. Naidich, and C. Novak. Boundary-specific cost functions for quantitative airway analysis. In *Medical Image Computing and Computer-Assisted Intervention*, volume 4791 of *Lecture Notes in Computer Science*, pages 784–791, 2007.

[46] A. P. Kiraly, W. E. Higgins, G. McLennan, E. A. Hoffman, and J. M. Reinhardt. Three-dimensional human airway segmentation methods for clinical virtual bronchoscopy. *Academic Radiology*, 9(10):1153–1168, 2002.

[47] T. Kitasaka, K. Mori, Y. Suenaga, J. Hasegawa, and J. Toriwaki. A method for segmenting bronchial trees from 3D chest X-ray CT images. In *Medical Image Computing and Computer-Assisted Intervention*, volume 2879 of *Lecture Notes in Computer Science*, pages 603–610, 2003.

[48] J. Kittler and F. M. Alkoot. Moderating k-NN classifiers. *Pattern Analysis & Applications*, 5(3):326–332, 2002.

[49] J. M. Kuhnigk, H. Hahn, M. Hindennach, V. Dicken, S. Krass, and H. O. Peitgen. Lung lobe segmentation by anatomy-guided 3D watershed transform. In M. Sonka and J. M. Fitzpatrick, editors, *Medical Imaging 2003: Image Processing*, volume 5032, pages 1482–1490. SPIE, 2003.

[50] W. G. Kuschner, A. D'Alessandro, H. Wong, and P. D. Blanc. Dose-dependent cigarette smoking-related inflammatory responses in healthy adults. *European Respiratory Journal*, 9(10):1989–1994, Oct 1996.

[51] X. Q. Lao, C. Q. Jiang, W. S. Zhang, P. Adab, T. H. Lam, K. K. Cheng, and G. N. Thomas. Smoking, smoking cessation and inflammatory markers in older Chinese men: The Guangzhou Biobank Cohort Study. *Atherosclerosis*, 203(1):304–310, 2009.

[52] J. Lee and A. P. Reeves. Segmentation of the airway tree from chest CT using local volume of interest. In *Proc. of Second International Workshop on Pulmonary Image Analysis*, pages 333–340, 2009.

[53] Y. K. Lee, Y.-M. Oh, J.-H. Lee, E. K. Kim, J. H. Lee, N. Kim, J. B. Seo, S. D. Lee, and K. O. L. D. S. Group. Quantitative assessment of emphysema, air trapping, and airway thickening on computed tomography. *Lung*, 186(3):157–165, 2008.

[54] B. Li and J. Reinhardt. Automatic generation of object shape models and their application to tomographic image segmentation. In M. Sonka and K. Hanson, editors, *Medical Imaging 2001: Image Processing*, volume 4322, pages 311–322. SPIE, 2001.

[55] B. Li, G. E. Christensen, E. A. Hoffman, G. McLennan, and J. M. Reinhardt. Pulmonary CT image registration and warping for tracking tissue deformation during the respiratory cycle through 3D consistent image registration. *Medical Physics*, 35(12):5575–5583, 2008.

[56] H. Li, A. Yezzi, and L. Cohen. 3D multi-branch tubular surface and centerline extraction with 4D iterative key points. In *Medical Image Computing and Computer-Assisted Intervention*, volume 5762 of *Lecture Notes in Computer Science*, pages 1042–1050.

[57] T. Lindeberg. Feature detection with automatic scale selection. *International Journal of Computer Vision*, 30(2):79–116, 1998.

[58] P. Lo, J. Sporring, H. Ashraf, J. Pedersen, and M. de Bruijne. Vessel-guided airway segmentation based on voxel classification. In M. Brown, M. de Bruijne, B. van Ginneken, A. Kiraly, J. Kuhnigk, C. Lorenz, K. Mori, and J. Reinhardt, editors, *Proc. of First International Workshop on Pulmonary Image Analysis*, pages 113–121, 2008.

[59] P. Lo, B. van Ginneken, J. Reinhardt, and M. de Bruijne. Extraction of airways from CT (EXACT'09). In *Second International Workshop on Pulmonary Image Analysis*, pages 175–189, 2009.

[60] P. Lo and M. de Bruijne. Voxel classification based airway tree segmentation. In *Medical Imaging 2008: Image Processing*, volume 6914, page 69141K. SPIE, 2008.

[61] P. Lo, J. Sporring, and M. de Bruijne. Multiscale vessel-guided airway tree segmentation. In *Proc. of Second International Workshop on Pulmonary Image Analysis*, pages 323–332, 2009.

[62] P. Lo, J. Sporring, J. J. H. Pedersen, and M. de Bruijne. Airway tree extraction with locally optimal paths. In *Medical Image Computing and Computer-Assisted Intervention*, volume 5762 of *Lecture Notes in Computer Science*, pages 51–58, 2009.

[63] R. Malladi and J. Sethian. Level set and fast marching methods in image processing and computer vision. In *Proc. International Conference on Image Processing*, volume 1, pages 489–492 vol.1, 1996.

[64] R. Manniesing, B. Velthuis, M. van Leeuwen, I. van der Schaaf, P. van Laar, and W. Niessen. Level set based cerebral vasculature segmentation and diameter quantification in CT angiography. *Medical Image Analysis*, 10(2):200–214, 2006.

[65] A. Marin, E. Mons, M. Garcia, J. Sauleda, A. Noguera, J. Pons, A. Agust, and J. Morera. Variability and effects of bronchial colonisation in patients with moderate COPD. *European Respiratory Journal*, 35(2):295–302, Jul 2009.

[66] C. D. Mathers and D. Loncar. Projections of global mortality and burden of disease from 2002 to 2030. *PLoS Medicine*, 3(11):e442, Nov 2006.

[67] D. Mayer, D. Bartz, J. Fischer, S. Ley, A. del Río, S. Thust, H.-U. Kauczor, and C. P. Heussel. Hybrid segmentation and virtual bronchoscopy based on CT images. *Academic Radiology*, 11(5):551–565, 2004.

[68] C. S. Mendoza, B. Acha, and C. Serrano. Maximal contrast adaptive region growing for CT airway tree segmentation. In *Proc. of Second International Workshop on Pulmonary Image Analysis*, pages 285–295, 2009.

[69] A. Morabia, M. S. Bernstein, F. Curtin, and M. Berode. Validation of self-reported smoking status by simultaneous measurement of carbon monoxide and salivary thiocyanate. *Preventive Medicine*, 32(1):82–88, Jan 2001.

[70] K. Mori, J. Hasegawa, Y. Suenaga, and J. Toriwaki. Automated anatomical labeling of the bronchial branch and its application to the virtual bronchoscopy system. *IEEE Transactions on Medical Imaging*, 19(2):103–114, Feb. 2000.

[71] K. Mori, J. Hasegawa, J. Toriwaki, H. Anno, and K. Katada. Recognition of bronchus in three-dimensional X-ray CT images with applications to virtualized bronchoscopy system. In *Proc. 13th International Conference on Pattern Recognition*, volume 3, pages 528–532 vol.3, 1996.

[72] K. Mori, Y. Nakada, T. Kitasaka, Y. Suenaga, H. Takabatake, M. Mori, and H. Natori. Lung lobe and segmental lobe extraction from 3D chest CT datasets based on figure decomposition and Voronoi division. In J. M. Reinhardt and J. P. W. Pluim, editors, *Medical Imaging 2008: Image Processing*, volume 6914, page 69144K. SPIE, 2008.

[73] C. J. Murray and A. D. Lopez. Evidence-based health policy–lessons from the global burden of disease study. *Science*, 274(5288):740–743, Nov 1996.

[74] C. J. Murray and A. D. Lopez. Mortality by cause for eight regions of the world: Global burden of disease study. *Lancet*, 349(9061):1269–1276, May 1997.

[75] Y. Nakano, S. Muro, H. Sakai, T. Hirai, K. Chin, M. Tsukino, K. Nishimura, H. Itoh, P. D. Paré, J. C. Hogg, and M. Mishima. Computed tomographic measurements of airway dimensions and emphysema in smokers. Correlation with lung function. *American Journal of Respiratory and Critical Care Medicine*, 162(3 Pt 1):1102–1108, Sep 2000.

[76] J. D. Newell, J. C. Hogg, and G. L. Snider. Report of a workshop: Quantitative computed tomography scanning in longitudinal studies of emphysema. *European Respiratory Journal*, 23(5):769–775, May 2004.

[77] R. A. Ochs, J. G. Goldin, F. Abtin, H. J. Kim, K. Brown, P. Batra, D. Roback, M. F. McNitt-Gray, and M. S. Brown. Automated classification of lung bronchovascular anatomy in CT using AdaBoost. *Medical Image Analysis*, 11(3):315–324, 2007.

[78] D. G. Parr, B. C. Stoel, J. Stolk, and R. A. Stockley. Validation of computed tomographic lung densitometry for monitoring emphysema in Alpha1-antitrypsin deficiency. *Thorax*, 61(6):485–490, Jun 2006.

[79] D. G. Parr, M. Sevenoaks, C. Deng, B. C. Stoel, and R. A. Stockley. Detection of emphysema progression in Alpha1-antitrypsin deficiency using CT densitometry; methodological advances. *Respiratory Research*, 9:21, 2008.

[80] J. Pedersen, H. Ashraf, A. Dirksen, K. Bach, H. Hansen, P. Toennesen, H. Thorsen, J. Brodersen, B. Skov, M. Døssing, J. Mortensen, K. Richter, P. Clementsen, and N. Seersholm. The Danish randomized lung cancer CT screening trial - Overall design and results of the prevalence round. *Journal of Thoracic Oncology*, April 2009.

[81] J. Petersen, P. Lo, M. Nielsen, G. Edula, H. Ashraf, A. Dirksen, and M. de Bruijne. Quantitative analysis of airway abnormalities in CT. In *Medical Imaging 2010: Image Processing (to appear)*. SPIE, 2010.

[82] R. Pinho, S. Luyckx, and J. Sijbers. Robust region growing based intrathoracic airway tree segmentation. In *Proc. of Second International Workshop on Pulmonary Image Analysis*, pages 261–271, 2009.

[83] C. Pisupati, L. Wolff, and E. Zerhouni. Segmentation of 3D pulmonary trees using mathematical morphology. In *Proc. Mathematical Morphology and its Applications to Image and Signal Processing, Atlanta*, pages 409–416, 1996.

[84] E. Prescott, M. Osler, H. O. Hein, K. Borch-Johnsen, P. Schnohr, and J. Vestbo. Life expectancy in Danish women and men related to smoking habits: Smoking may affect women more. *Journal of Epidemiology & Community Health*, 52(2):131–132, Feb 1998.

[85] N. B. Pride. Smoking cessation: Effects on symptoms, spirometry and future trends in COPD. *Thorax*, 56 Suppl 2:ii7–i10, Sep 2001.

[86] P. Pudil, J. Novovičová, and J. Kittler. Floating search methods in feature selection. *Pattern Recognition Letters*, 15(11):1119–1125, 1994.

[87] K. F. Rabe, S. Hurd, A. Anzueto, P. J. Barnes, S. A. Buist, P. Calverley, Y. Fukuchi, C. Jenkins, R. Rodriguez-Roisin, C. van Weel, J. Zielinski, and Global Initiative for Chronic Obstructive Lung Disease. Global strategy for the diagnosis, management, and prevention of chronic obstructive pulmonary disease: Gold executive summary. *American Journal of Respiratory and Critical Care Medicine*, 176(6):532–555, Sep 2007.

[88] M. Saetta. Airway inflammation in chronic obstructive pulmonary disease. *American Journal of Respiratory and Critical Care Medicine*, 160(5 Pt 2):S17–S20, Nov 1999.

[89] P. D. Scanlon, J. E. Connett, L. A. Waller, M. D. Altose, W. C. Bailey, and A. S. Buist. Smoking cessation and lung function in mild-to-moderate chronic obstructive pulmonary disease. The Lung Health Study. *American Journal of Respiratory and Critical Care Medicine*, 161(2 Pt 1):381–390, Feb 2000.

[90] T. Schlathölter, C. Lorenz, I. C. Carlsen, S. Renisch, and T. Deschamps. Simultaneous segmentation and tree reconstruction of the airways for virtual bronchoscopy. In M. Sonka and J. M. Fitzpatrick, editors, *Medical Imaging 2002: Image Processing*, volume 4684, pages 103–113. SPIE, 2002.

[91] S. B. Shaker, A. Dirksen, C. S. Ulrik, M. Hestad, T. Stavngaard, L. C. Laursen, N. Maltbaek, P. Clementsen, N. Skjaerbaek, L. Nielsen, B. Stoel, L. T. Skovgaard, and P. Tonnesen. The effect of inhaled corticosteroids on the development of emphysema in smokers assessed by annual computed tomography. *COPD: Journal of Chronic Obstructive Pulmonary Disease*, 6(2):104–111, 2009.

[92] H. Singh, M. Crawford, J. P. Curtin, and R. Zwiggelaar. Automated 3D segmentation of the lung airway tree using gain-based region growing approach. In *Medical Image Computing and Computer-Assisted Intervention*, volume 3217 of *Lecture Notes in Computer Science*, pages 975–982, 2004.

[93] I. Sluimer, M. Prokop, and B. van Ginneken. Toward automated segmentation of the pathological lung in CT. *IEEE Transactions on Medical Imaging*, 24(8):1025–1038, Aug. 2005.

[94] I. Sluimer, A. Schilham, M. Prokop, and B. van Ginneken. Computer analysis of computed tomography scans of the lung: A survey. *IEEE Transactions on Medical Imaging*, 25(4):385–405, April 2006.

[95] G. L. Snider, L. J. Kleinerman, W. M. Thurlbeck, and Z. H. Bengali. The definition of emphysema. Report of a National Heart, Lung, and Blood Institute, Division of Lung Diseases workshop. *American Review of Respiratory Disease*, 132(1):182–185, Jul 1985.

[96] K. Soejima, K. Yamaguchi, E. Kohda, K. Takeshita, Y. Ito, H. Mastubara, T. Oguma, T. Inoue, Y. Okubo, K. Amakawa, H. Tateno, and T. Shiomi. Longitudinal follow-up study of smoking-induced lung density changes by high-resolution computed tomography. *American Journal of Respiratory and Critical Care Medicine*, 161(4 Pt 1):1264–1273, Apr 2000.

[97] M. Sonka, W. Park, and E. Hoffman. Rule-based detection of intrathoracic airway trees. *IEEE Transactions on Medical Imaging*, 15(3):314–326, 1996.

[98] J. Stolk, M. I. M. Versteegh, L. J. Montenij, M. E. Bakker, E. Grebski, M. Tutic, S. Wildermuth, W. Weder, M. el Bardiji, J. H. C. Reiber, K. F. Rabe, E. W. Russi, and B. C. Stoel. Densitometry for assessment of effect of lung volume reduction surgery for emphysema. *European Respiratory Journal*, 29(6):1138–1143, Jun 2007.

[99] X. Sun, H. Zhang, and H. Duan. 3D computerized segmentation of lung volume with computed tomography. *Academic Radiology*, 13(6):670–677, 2006.

[100] J. Tschirren, E. Hoffman, G. McLennan, and M. Sonka. Intrathoracic airway trees: segmentation and airway morphology analysis from low-dose CT scans. *IEEE Transactions on Medical Imaging*, 24(12):1529–1539, Dec. 2005.

[101] J. Tschirren, T. Yavarna, and J. Reinhardt. Airway segmentation framework for clinical environments. In *Proc. of Second International Workshop on Pulmonary Image Analysis*, pages 227–238, 2009.

[102] J. N. Tsitsiklis. Efficient algorithms for globally optimal trajectories. *IEEE Transactions on Automatic Control*, 40(9):1528–1538, 1995.

[103] G. Turato, A. D. Stefano, P. Maestrelli, C. E. Mapp, M. P. Ruggieri, A. Roggeri, L. M. Fabbri, and M. Saetta. Effect of smoking cessation on airway inflammation in chronic bronchitis. *American Journal of Respiratory and Critical Care Medicine*, 152(4 Pt 1):1262–1267, Oct 1995.

[104] S. Ukil, M. Sonka, and J. M. Reinhardt. Automatic segmentation of pulmonary fissures in X-ray CT images using anatomic guidance. In J. M. Reinhardt and J. P. W. Pluim, editors, *Medical Imaging 2006: Image Processing*, volume 6144, page 61440N. SPIE, 2006.

[105] H. van der Vaart, D. S. Postma, W. Timens, and N. H. T. ten Hacken. Acute effects of cigarette smoke on inflammation and oxidative stress: A review. *Thorax*, 59(8):713–721, Aug 2004.

[106] B. van Ginneken, W. Baggerman, and E. van Rikxoort. Robust segmentation and anatomical labeling of the airway tree from thoracic CT scans. In *Medical Image Computing and Computer-Assisted Intervention*, volume 5241 of *Lecture Notes in Computer Science*, pages 219–226, 2008.

[107] B. van Ginneken, S. G. A. III, B. de Hoop, S. van de Vorst, T. Duindam, M. Niemeijer, K. Murphy, A. M. R. Schilham, A. Retico, M. E. Fantacci, N. Camarlinghi, F. Bagagli, I. Gori, T. Hara, H. Fujita, G. Gargano, R. Belloti, F. D. Carlo, R. Megna, S. Tangaro, L. Bolanos, P. Cerello, S. C. Cheran, E. L. Torres, and M. Prokop. Comparing and combining algorithms for computer-aided detection of pulmonary nodules in computed tomography scans: The ANODE09 study. Technical report, Image Sciences Institute, Utrecht University, 2009.

[108] C. A. van Iersel, H. J. de Koning, G. Draisma, W. P. Mali, E. T. Scholten, K. Nackaerts, M. Prokop, J. D. F. Habbema, M. Oudkerk, and R. J. van Klaveren. Risk-based selection from the general population in a screening trial: Selection criteria, recruitment and power for the Dutch-Belgian randomised lung cancer multi-slice CT screening trial (NELSON). *International Journal of Cancer*, 120(4):868–874, 2007.

[109] E. M. van Rikxoort and B. van Ginneken. A pattern recognition approach to enhancing structures in 3D CT data. In J. P. W. P. Joseph M. Reinhardt, editor, *Medical Imaging 2006: Image Processing*, volume 6144, pages 569–576. SPIE, 2006.

[110] E. van Rikxoort, B. de Hoop, M. Viergever, M. Prokop, and B. van Ginneken. Automatic lung segmentation from thoracic computed tomography scans using a hybrid approach with error detection. *Medical Physics*, 36(7):2934–2947, 2009.

[111] E. M. van Rikxoort, W. Baggerman, and B. van Ginneken. Automatic segmentation of the airway tree from thoracic CT scans using a multi-threshold approach. In *Proc. of Second International Workshop on Pulmonary Image Analysis*, pages 341–349, 2009.

[112] J. Vestbo, T. Srensen, P. Lange, A. Brix, P. Torre, and K. Viskum. Long-term effect of inhaled budesonide in mild and moderate chronic obstructive pulmonary disease: A randomised controlled trial. *Lancet*, 353(9167):1819–1823, May 1999.

[113] J. Vestbo. Systemic inflammation and progression of COPD. *Thorax*, 62(6):469–470, Jun 2007.

[114] T. Wang and A. Basu. A note on 'A fully parallel 3D thinning algorithm and its applications'. *Pattern Recognition Letters*, 28(4):501–506, 2007.

[115] J. Weickert. Coherence-enhancing diffusion filtering. *International Journal of Computer Vision*, 31(2-3):111–127, April 1999.

[116] J. Weickert, S. Ishikawa, and A. Imiya. On the history of Gaussian scale-space axiomatics. In J. Sporring, M. Nielsen, L. Florack, and P. Johansen, editors, *Gaussian Scale-Space Theory*, chapter 4, pages 45–59. Kluwer Academic Publishers, Dordrecht, The Netherlands, 1997.

[117] O. Weinheimer, T. Achenbach, C. Bletz, C. Duber, H. U. Kauczor, and C. P. Heussel. About objective 3-D analysis of airway geometry in computerized tomography. *IEEE Transactions on Medical Imaging*, 27(1):64–74, Jan 2008.

[118] O. Weinheimer, T. Achenbach, C. Buschsiewke, C. P. Heussel, T. Uthmann, and H.-U. Kauczor. Quantification and characterization of pulmonary emphysema in multislice-CT. In *ISMDA*, pages 75–82, 2003.

[119] O. Weinheimer, T. Achenbach, and C. Düber. Fully automated extraction of airways from CT scans based on self-adapting region growing. In *Proc. of Second International Workshop on Pulmonary Image Analysis*, pages 315–321, 2009.

[120] R. Wiemker, T. Buelow, and C. Lorenz. A simple centricity-based region growing algorithm for the extraction of airways. In *Proc. of Second International Workshop on Pulmonary Image Analysis*, pages 309–314, 2009.

[121] Z. Wu, E. Rietzel, V. Boldea, D. Sarrut, and G. C. Sharp. Evaluation of deformable registration of patient lung 4DCT with subanatomical region segmentations. *Medical Physics*, 35(2):775–781, Feb 2008.

[122] X. Zhou, T. Hayashi, T. Hara, H. Fujita, R. Yokoyama, T. Kiryu, and H. Hoshi. Automatic segmentation and recognition of anatomical lung structures from high-resolution chest CT images. *Computerized Medical Imaging and Graphics*, 30(5):299–313, 2006.

[123] J. Zielinski, W. MacNee, J. Wedzicha, N. Ambrosino, A. Braghiroli, J. Dolensky, P. Howard, K. Gorzelak, A. Lahdensuo, K. Strom, M. Tobiasz, and E. Weitzenblum. Causes of death in patients with COPD and chronic respiratory failure. *Monaldi Archives of Chest Disease*, 52(1):43–47, Feb 1997.

[124] R. L. ZuWallack, M. C. Haggerty, and P. Jones. Clinically meaningful outcomes in patients with chronic obstructive pulmonary disease. *American Journal of Medicine*, 117 Suppl 12A:49S–59S, Dec 2004.

Publications

Papers in international journals

- P. Lo, J. Sporring, H. Ashraf, J. J. H. Pedersen and M. de Bruijne. Vessel-guided airway tree segmentation: A voxel classification approach. In *Medical Image Analysis*, volume 14(4), pages 527-538, 2010.

- H. Ashraf, P. Lo, S. B. Shaker, M. de Bruijne, A. Dirksen, P. Tønnesen, M. Dahlbäck, J. J. H. Pedersen. Short term effect of changes in smoking behaviour on lung density by computed tomography. Submitted, 2010.

Papers in conference proceedings

- L. Sørensen, M. Loog, P. Lo, H. Ashraf, A. Dirksen, R. P. W. Duin, and M. de Bruijne. Image dissimilarity-based quantification of lung disease from CT. In *Medical Image Computing and Computer-Assisted Intervention* (to appear). 2010.

- V. Gorbunova, S. S. A. M. Jacobs, P. Lo, A. Dirksen, M. Nielsen, A. Bab-Hadiashar, and M. de Bruijne. Early detection of emphysema progression. In *Medical Image Computing and Computer-Assisted Intervention* (to appear). 2010.

- P. Lo, B. van Ginneken and M. de Bruijne. Vessel tree extraction using locally optimal paths. In *IEEE International Symposium on Biomedical Imaging*, pages 680-683, 2010.

- J. Petersen, P. Lo, M. Nielsen, G. Edula, H. Ashraf, A. Dirksen, and M. de Bruijne. Quantitative analysis of airway abnormalities in CT. In *Medical Imaging 2010: Image Processing*, volume 7624, page 76241S. SPIE, 2010.

- C. Chen, K. Chernoff, G. Karemore, P. Lo, M. Nielsen, and F. Lauze. Classification in medical images using adaptive metric k-NN. In *Medical Imaging 2010: Image Processing*, volume 7623, page 76230S. SPIE, 2010.

- P. Lo, J. Sporring, J. J. H. Pedersen, and M. de Bruijne. Airway tree extraction with locally optimal paths. In *Medical Image Computing and Computer-Assisted Intervention*, volume 5762 of *Lecture Notes in Computer Science*, pages 51-58, 2009.

- L. Sørensen, P. Lo, H. Ashraf, J. Sporring, M. Nielsen and M. de Bruijne. Learning COPD sensitive filters in pulmonary CT. In *Medical Image Computing and Computer-Assisted Intervention*, volume 5762 of *Lecture Notes in Computer Science*, pages 699-706, 2009.

- P. Lo, B. van Ginneken, J. Reinhardt, and M. de Bruijne. Extraction of airways from CT (EXACT'09). In *Second International Workshop on Pulmonary Image Analysis*, pages 175-189, 2009.

- P. Lo, J. Sporring and M. de Bruijne. Multiscale Vessel-guided Airway Tree Segmentation. In *Second International Workshop on Pulmonary Image Analysis*, pp. 323-332, 2009.

- V. Gorbunova, S. Durrleman, P. Lo, X. Pennec, and M. de Bruijne. Curve- and surface-based registration of lung CT images via currents. In *Second International Workshop on Pulmonary Image Analysis*, pages 15-25, 2009.
- K. Murphy, B. van Ginneken, E. M. van Rikxoort, B. J. de Hoop, M. Prokop, P. Lo, M. de Bruijne, and J. P. W. Pluim. Obstructive pulmonary function: Patient classification using 3D registration of inspiration and expiration CT images. In *Second International Workshop on Pulmonary Image Analysis*, pages 37-47, 2009.
- V. Gorbunova, P. Lo, M. Loeve, H. Tiddens, J. Sporring, M. Nielsen, and M. de Bruijne. Mass preserving registration for lung CT. In *Medical Imaging 2009: Image Processing*, volume 7259, page 72592R. SPIE, 2009.
- V. Gorbunova, P. Lo, H. Ashraf, A. Dirksen, M. Nielsen, and M. D. Bruijne. Weight preserving image registration for monitoring disease progression in lung CT. In *Medical Image Computing and Computer-Assisted Intervention*, volume 5242 of *Lecture Notes in Computer Science*, pages 863-870, 2008.
- P. Lo, J. Sporring, H. Ashraf, J. Pedersen, and M. de Bruijne. Vessel-guided airway segmentation based on voxel classification. In *First International Workshop on Pulmonary Image Analysis*, pages 113-121, 2008.
- P. Lo and M. de Bruijne. Voxel classification based airway tree segmentation. In *Medical Imaging 2008: Image Processing*, volume 6914, page 69141K. SPIE, 2008.

Published abstracts

- H. Ashraf, P. Lo, S. B. Shaker, M. de Bruijne, A. Dirksen, P. Tønnesen, M. Dahlbäck, and J. H. Pedersen. Change in smoking habits affects lung density by CT. In *American Thoracic Society International Conference*, 2009
- G. Edula, H. Ashraf, P. Lo, M. de Bruijne, M. Dahlbäck, and J. H. Pedersen. Natural progression of lung density changes in COPD measured by MSCT: Correlation to lung function. In *American Thoracic Society International Conference*, 2009
- P. Lo, J. Sporring, H. Ashraf, J. Pedersen, and M. de Bruijne. Voxel classification based vessel-guided airway segmentation. In *Proceedings of the Danish Conference on Pattern Recognition and Image Analysis*, pages 08-10, 2008.

Acknowledgments

Now that I finally finished my PhD and have a chance to look back, I am happy to note that my three years PhD journey in the Department of Computer Science (DIKU) in the University of Copenhagen had been a very wonderful and fulfilling one indeed. Although there are some frustrating and annoying times, which I am fortunate to only have few of them, I think it is these "bitter sweet" experiences that make everything just that more memorable and cherishable. It is also through these difficult times, that I was able to really appreciate the importance of the people around me. It is thanks to their help and support that I am able to reach the end goal of my PhD journey, which is this thesis. I hope the end of my PhD journey will not be the ending where everyone goes on their separate ways, but will mark the new beginning where we embark on another even more wonderful journey.

First of all, I would like to thank my supervisor, Marleen de Bruijne, for giving me the chance to start on this journey in the first place. Throughout my journey, Marleen has always been my main source of support, guidance, encouragement and inspiration both within and outside the scope the PhD studies. I would also like to thank her for her patience and willingness to listen to my frequently unstructured, seemingly random and often long winded "report". Although it can be a bit "traumatic" at times, Marleen's ability in asking very sharp questions that are critical to the problem at hand never ceases to amaze me and have taught me a lot in terms of how to do research properly. Thank you Marleen for holding the rein of this wild horse till it reaches its destination throughout all these years.

Besides having a great supervisor, I was also fortunate enough to have two good and helpful co-supervisors, Jon Sporring and Mads Nielsen. Jon has been very supportive throughout my studies and is the main contributor of some of the concepts behind my work. His tendency of playing the role of the devil's advocate not only struck fear into me at times, but more importantly forces me to look at things more thoroughly and be more mature in my thinking. Although Mads and I seldom met, partly due to Mads heavily packed time schedule and that I am already in the safe hands of both Marleen and Jon, Mads' vision on "how things should be done" that he conveyed to me through those few occasions where we met has been very inspiring and has given me a brief view of the future of medical image analysis.

It has been fun working alongside with both Lauge Sørensen and Vladlena Gorbunova on the "COPD project", which is the center of this thesis. It has been a real luxury to not only have one, but two persons who know my work intimately to discuss my problems with. Although, I have to admit that I often abused this luxury and used it for bragging and procrastinate purpose instead. Lauge, thank you for being a great and responsive audience throughout the years, and also for those enlightening after office hour discussions. Thank you Vladlena for making the effort to invite me to barbecue and dinner parties from time to time, thus keeping me from growing mold in my apartment. Also, thanks for the the wonderful, though slightly tiring, tour of Russia.

The COPD project would not have progress as smoothly as it had if not for the collaborations of our partners in Gentofte Hospital and Astra Zeneca. From Gentofte, I would like to thank Asger Dirksen for his invaluable insights on the physiology of the human lungs, Haseem Ashraf for the countless free rides between Gentofte and DIKU, and the various helps from Jesper Pedersen, Saher Shaker and Zaigham Saghir. From Astra Zeneca, I would like to thank Magnus Dahlbäck, Thomas Fehniger, Goutham Edula and Lars Wigström for their support and interests. Asger, Haseem and Goutham are also the main contributor behind the evaluation of the lung segmentation algorithm, which plays a critical role in one of the chapter in this thesis.

The EXACT'09 challenge would not have been possible if not for the help of Bram van Ginneken and Joseph Reinhardt. I would like to especially thank Bram for his effort in assembling the

team of medical students who are instrumental to the challenge, namely Michiel Boekhout, Karina Grooteman, Raya Brandenburg, Anouk van Burgel, Viviana Cuellar, Maartje Mulder, Kejal-Ramona Charaghvandi, Laura Vos, Laila Lamchachti, Chani Marie and Welling Oei. My thanks also to the 15 participating teams of the EXACT'09 challenge for their bravery, and to the contributors of the CT scans used from various institutions in the USA, Germany, the Netherlands, Denmark and Japan, which are critical to the success of the challenge.

The administrative staffs of DIKU have helped me a lot in maneuvering through the maze of forms and various application process. Thank you Marianne Henriksen and Dina Riis Johannessen for your help in dealing the travel applications, taxes, formal letters and what not during my studies. Thank you Camilla Jørgensen for keeping the Image Group running smoothly and for your often contagious cheerful giggle that never failed to bring a smile to my face. Thank you Ruth Schlüter for your hospitality.

Another reason for my great time in DIKU is thanks to the people in the Image Group. I would like to thank the "adults" in the groups, Marco Loog for the enjoyable Friday beer session (when he was still in Copenhagen), Francois Lauze for the various pranks and a meatless summer party, Kenny Erleben for the discussions on science, often after a few bottle of beers, Kim Steenstrup Pedersen for his library of books, and Peter Johansen, Søren Olsen and Knud Henriksen for the interesting conversations and helps on various occasions. To the residents of the "evil office", Chen Chen, Aasa Feragen, Stefan Sommer, Søren Hauberg, Morten Nørgaard Larsen and Konstantin Chernoff, thank you for the various wonderful times, especially to Søren for the somewhat strange experience at Hven and also the equally strange party after that. My thanks to Sune Darkner, the only non-COPD person in the "good office", for the interesting discussions. Thank you Jens Petersen for letting me be part of your journey to your masters thesis. My thanks to the "Nordic bunch", Melanie Ganz, Kersten Petersen, Lene Lillemark Larsen, Gopal Karemore, Alexandro Crimi and Joselene Marques for the various wonderful occasions as well. There is also a list of ex-DIKU research staff whom I owe my thanks to, namely Eugenio Iglesias, who took the trouble forcing me to explore Copenhagen during my early days, Sune Keller, Rabia Granlund, Eva van Rikxoort, Michael Lund, Anne Cuzol, Jakob Raundahl, Lars Schjøth, Aditya Tatu, Ketut Fundana, Ali Reza Bab-Hadiashar, Eric Creusen, Jerome Lapuyade, Pauline Julian and Katja Gamby.

I would like to thank Bram again for his hospitality during my visits and my three months residence in the Image Science Institute (ISI) at Utrecht. I also owe my enjoyable time there to the secretaries at ISI for finding a nice apartment for me during my stay in Utrecht. My thanks would not be complete without thanking the research staffs in the CAD group at ISI for my wonderful time there, namely Evelien van Dongen for her invaluable help in getting me started on the topic of pulmonary vessels segmentation, Thomas Duindam, Ewoud Smit, Geert Litjens, Sasha Muenzing, Adriënne Mendrik, Ivana Isgum, Christian Mol, Thessa Kockelkorn and Clarisa Sánchez. I hope I manage to cover everyone in the CAD group here, for those whose names I forgot to mentioned, my sincere apologies and my thanks for the great time I had in ISI.

Thank you Christian Mailand for your hospitality during my early days in Copenhagen. To John Wrisberg, Janus Lundager and Rune Andresen from the IT support in DIKU, thank you guys for the help with my notebook and the servers. My thanks to my Malaysian friends, Viktor Goh, Renbin Yang, Mathias Foo and Timothy Yap for "listening" to my frequent ramblings via messenger. Also, special thanks to Michel Bister, my supervisor back in the days when I was a masters student in Multimedia University, for introducing me to the fun and challenging field of medical image analysis.

I would also like to thank the Danish Council for Strategic Research (NABIIT) for funding the project and my research. I probably should also thank Google for landing me the job in the first place, and Yahoo messenger, MSN messenger, Skype and VoipStunt for making it possible for me to keep in contact with my friends and families who are mostly at the other side of the world.

Last but not least, I would like to thank my parents, my sisters and brother back in Malaysia for their support. Specifically, my mom for allowing me to be so far away from home to pursue my studies, my dad for knocking the sense into me, both figuratively and literally speaking, during my rebellious years, and finally my sisters and brother for taking care of my parents in my absence. Finally, to my parents (in Chinese):

因为有你们，才有今天的我

(Because of both of you, there is a me today)